



# **Simulation of process-induced deformations of fusion bonded hybrid components and potential analysis in a car model**

## **Master Thesis**

Name:	Suba Siva Chandran Kalimuthu
Matriculation Number:	4868941
Course:	Computational Sciences in Engineering
Examiner:	Univ.-Prof. Dr.-Ing. Prof.h.c. Klaus Dilger
Supervisor:	Niklas Günther M.Sc., Institut für Füge und Schweißtechnik
In cooperation with:	GNS mbH
Company supervisor:	Crash simulation - Research and Methods Dipl.-Ing. Erdeniz Ince 
Date of Submission:	23.08.2021

# **Declaration**

I hereby declare on oath that I have independently written the present Master thesis work "Simulation of process-induced deformations of fusion bonded hybrid components and potential analysis in a car model" and I have fully stated all sources and tools used. The work has not been submitted as an examination paper before.

Braunschweig, 23.08.2021

Signature

# Abstract

Reducing fuel consumption and to meet the increasingly stringent requirements for CO<sub>2</sub> fleet consumption are the major challenges faced by the automotive industry when developing and manufacturing lightweight structural components. Therefore, combining classic materials such as high-strength steel and aluminium with fiber-reinforced plastics which exhibits greater lightweight potential is a crucial tool for overcoming this challenge. For this reason, traditional construction materials are reinforced or patched with lightweight materials in a wide variety of application areas.

There are numerous well-established joining techniques of metallic structures with FRP's (Fiber-reinforced polymer). In this work, the process of heat-assisted press joining technique is examined experimentally and numerically. The aim of this investigation is to produce a hybrid plate made of Steel and glass fiber reinforced with thermoplastic matrix along with a high temperature, modified epoxy film adhesive Redux®677 using this technique and the joining process is to be simulated in FEM (Finite Element method) software ABAQUS™. After the process simulation and a comparison with the experimental results are finalized, a purely simulative potential analysis is carried out on a complete vehicle model (Toyota Camry) already available from GNS mbH with variation of the component thicknesses. The accomplished process simulation method is then transferred to a component in car model and the process related deformations are evaluated on that component as an example.

---

# Acknowledgement

I would like to express my gratitude to my supervisor Mr. Niklas Günther M.Sc., for his constant support and encouragement throughout my academics. His knowledge sharing regarding the bonding techniques theoretically and applying it numerically in the FE software helped me a lot to learn the key and advanced concepts.

At GNS mbH I also had a lot of help by constructive and elaborate discussions with Mr. Dipl.-Ing. Erdeniz Ince and I would like to thank him for this.

I would also like to thank Mr. Michael Griese M.Sc., for helping to define a workflow for the experimental procedures and with the structural tests at the lab.

Finally I would like to thank my friends and family for their constant and wholesome support during my studies at TU Braunschweig.

# Contents

<b>List of Abbreviations</b>	<b>V</b>
<b>List of Figures</b>	<b>VI</b>
<b>List of Tables</b>	<b>XI</b>
<b>List of Variables</b>	<b>XII</b>
<b>1 Introduction</b>	<b>1</b>
1.1 Background . . . . .	1
1.2 Motivation . . . . .	1
1.3 Goal . . . . .	2
<b>2 State of the art</b>	<b>3</b>
2.1 Hybrid construction of BIW structure . . . . .	3
2.1.1 Metal-FRP connections . . . . .	5
2.2 Experimental techniques . . . . .	11
2.2.1 Fusion bonding - An introduction . . . . .	12
2.2.2 Process . . . . .	13
2.2.3 Mechanical tests . . . . .	18
2.3 Simulation techniques . . . . .	21
2.3.1 Process . . . . .	21
2.3.2 Mechanical tests . . . . .	23
2.4 Review of process parameters . . . . .	26
<b>3 Objective and methodical approach</b>	<b>30</b>
3.1 Questions in focus and research objectives . . . . .	30
3.2 Definition of research workflow . . . . .	31
3.3 Methodology . . . . .	33
3.3.1 Components in experimental process . . . . .	34
3.3.2 Cooling process implementation in ABAQUS™ . . . . .	34
3.3.3 Simulation outline . . . . .	35
<b>4 Experimental proceeding</b>	<b>38</b>
4.1 Equipment and materials . . . . .	38
4.1.1 Equipment used for the process and its validation . . . . .	38
4.1.2 Equipment used for the mechanical test . . . . .	39
4.1.3 Materials applied . . . . .	40
4.2 Process . . . . .	40
4.2.1 Pre-tests . . . . .	40

---

4.2.2	Cooling experiment for components of hybrid plate . . . . .	43
4.2.3	Process of producing hybrid plate . . . . .	47
4.2.4	Validation of production procedure . . . . .	49
4.3	3-point-bending experiments . . . . .	52
4.3.1	Flexural tests for Steel . . . . .	52
4.3.2	Flexural tests for GFRP . . . . .	53
4.3.3	Flexural tests for Hybrid Steel/GFRP-PA6 specimen . . . . .	54
<b>5</b>	<b>FEM simulation</b>	<b>57</b>
5.1	Process . . . . .	57
5.1.1	Simulation strategy . . . . .	57
5.1.2	Material model buildup . . . . .	58
5.1.3	Cooling process simulation FE model . . . . .	66
5.1.4	Process validation simulation . . . . .	70
5.2	Structural . . . . .	72
5.2.1	Simulation strategy . . . . .	72
5.2.2	Material model buildup . . . . .	73
5.2.3	Hybrid specimen validation simulation . . . . .	79
<b>6</b>	<b>Potential of hybrid components in Toyota Camry</b>	<b>81</b>
6.1	Analysis of different components in Camry . . . . .	81
6.1.1	V064 - Floorpanxmemberfrnt . . . . .	82
6.1.2	V065 - Floorpanxmember . . . . .	84
6.1.3	V068 - Midrailouter . . . . .	86
6.2	Hybrid component implementation analysis in Camry . . . . .	90
6.2.1	V095 - Floorpanxmember - 5 mm patch . . . . .	90
6.2.2	V097 - Floorpanxmember - 3 mm patch . . . . .	92
6.2.3	Preferred hybrid component variant . . . . .	94
6.2.4	Process simulation transfer to hybrid part . . . . .	96
<b>7</b>	<b>Results</b>	<b>98</b>
7.0.1	Cooling process simulation results . . . . .	98
7.0.2	Process validation simulation results . . . . .	105
7.0.3	Process simulation results of hybrid part from Camry . . . . .	109
<b>8</b>	<b>Summary</b>	<b>112</b>
<b>9</b>	<b>Bibliography</b>	<b>XIII</b>

# List of Abbreviations

Abbreviation	Description
FRP	Fiber-reinforced polymer
FEM	Finite element method
GHG	Green house gas
BIW	Body in white
CFRP	Carbon fiber reinforced polymer
GFRP	Glass fiber reinforced polymer
CDC	Cataphoretic dip coating
OEM	Original equipment manufacturer
TWB	Tailor welded blank
SLC	Super Light Car
TPMC	Thermoplastic matrix composite
TSMC	Thermoset matrix composite
GMT	Glass mat reinforced thermoplastic
SBS	Short beam strength
ILSS	Inter laminar shear strength
ODB	Offset deformable barrier
CEL	Coupled Eulerian-Lagrangian
FML	Fiber metal laminate
ASTM	American society for testing and materials
DIN EN	Deutsches Institut für Normung Europäische Norm
AFRP	Aramid fiber reinforced polymer
GLARE	Glass fiber reinforced aluminium laminates
CARALL	Carbon fiber reinforced aluminium laminates
CZM	Cohesive zone model
OHLF	Open hybrid lab factory
UTM	Universal testing machine
DCB	Double cantilever beam
CDP	Cataphoretic dip painting
IIHS	Insurance institute for highway safety

# List of Figures

Figure 2.1	Porsche 911 BIW [1] . . . . .	4
Figure 2.2	Comparison of CFRP and GFRP properties [2] . . . . .	4
Figure 2.3	Material properties which determines the use [3] . . . . .	5
Figure 2.4	Hybrid automotive components . . . . .	6
Figure 2.5	Audi R8 Space Frame [3] . . . . .	7
Figure 2.6	Comparison of weight of steel TWB and CR420/CFRP composite [4] . . . . .	8
Figure 2.7	Illustration of CFRP reinforcement in experimental BIW of BMW M6 [5] . . . . .	8
Figure 2.8	Hybrid B-pillar assembly made of Steel and CFRP in BMW M7 [6]	9
Figure 2.9	Aluminium and CFRP integrated parts in Carbon core in BMW M7	9
Figure 2.10	Multi-material BIW of the SLC [7] . . . . .	10
Figure 2.11	Weight savings of the multi-material BMW M6 [5] . . . . .	10
Figure 2.12	Lightweight seat structure [7] . . . . .	11
Figure 2.13	Illustration of fusion bonding process [8] . . . . .	12
Figure 2.14	Illustration of fusion bonding process [9] . . . . .	13
Figure 2.15	Setup for manufacturing hybrid plates [10] . . . . .	13
Figure 2.16	Manufacturing setup [11] . . . . .	14
Figure 2.17	Optimised joining apparatus and pressure profile [8] . . . . .	15
Figure 2.18	Process equipment [12] . . . . .	15
Figure 2.19	Overview of punching tool and induction heater . . . . .	16
Figure 2.20	Manufacturing setup for lap-shear samples [13] . . . . .	16
Figure 2.21	Joining setup [14] . . . . .	17
Figure 2.22	Test setup [15] . . . . .	18
Figure 2.23	Bending collapse behavior of thin-walled structures [16] . . . . .	19
Figure 2.24	Hybrid hat profile with spot-welded closing plate [10, 17] . . . . .	20
Figure 2.25	Crash test facility and Sample geometries [18] . . . . .	20
Figure 2.26	Boundary conditions on the process simulation FE model [11] . . . . .	22
Figure 2.27	Material behavior, simulation and experimental results comparison [11] . . . . .	23
Figure 2.28	3-point-bending FE model [19] . . . . .	23
Figure 2.29	Experimental and simulation setup of 3-point-bending model [20] .	24
Figure 2.30	Tensile and 3-point-bend FE model [21] . . . . .	24
Figure 2.31	Geometry (dimensions in mm), simulation results of the hybrid tubes under quasi-static bending [22] . . . . .	25
Figure 2.32	Experimental and numerical simulation setup of hybrid component [23] . . . . .	26
Figure 2.33	Failure modes . . . . .	29

---

Figure 3.1	Research workflow . . . . .	32
Figure 3.2	Importance of simulating cooling phase [1, 24] . . . . .	33
Figure 3.3	Key elements of the experimental process . . . . .	34
Figure 3.4	Illustration of film condition implementation in ABAQUS™ . . . . .	35
Figure 3.5	Outline of the simulation strategy for Process . . . . .	36
Figure 3.6	Outline of the simulation strategy for mechanical tests . . . . .	37
Figure 4.1	Press equipment used for the process . . . . .	38
Figure 4.2	Oven used for heating GFRP and laser based linear extensometer	39
Figure 4.3	Mechanical test using Instron 30 UTM . . . . .	39
Figure 4.4	Hybrid specimen manufactured using the adapted methodical process . . . . .	41
Figure 4.5	Fracture pattern from lap shear tests . . . . .	42
Figure 4.6	Comparison of different lap shear strengths . . . . .	42
Figure 4.7	Cooling setup of DP980 Steel plate . . . . .	43
Figure 4.8	Experimental cooling trials of the DP980 Steel plate . . . . .	44
Figure 4.9	Cooling setup of the Support plate with and without Kapton tape . . . . .	45
Figure 4.10	Experimental cooling trials of the support plate . . . . .	45
Figure 4.11	Cooling setup of the GFRP laminate . . . . .	46
Figure 4.12	Experimental cooling trials of the GFRP . . . . .	47
Figure 4.13	Production of DCB hybrid plate . . . . .	48
Figure 4.14	Cooling curves of the measured points . . . . .	48
Figure 4.15	Validation setup of the experimental process . . . . .	49
Figure 4.16	Cooling curves of the measured points . . . . .	50
Figure 4.17	Trials made for validation experiment . . . . .	50
Figure 4.18	Deflections measured before and after experimental process . . . . .	51
Figure 4.19	Misalignment of the steel joining partner on the GFRP . . . . .	51
Figure 4.20	Force-Displacement curves of 3PB of DP980 Steel . . . . .	52
Figure 4.21	Force-Displacement curves of 3PB of GFRP-PA6 . . . . .	53
Figure 4.22	Force-Displacement curves of 3PB of Hybrid specimens . . . . .	54
Figure 4.23	Failure mode and defects of the hybrid specimens . . . . .	56
Figure 5.1	Steel plate FE model . . . . .	58
Figure 5.2	Experimental vs Simulation results comparison for Steel plate . . . . .	59
Figure 5.3	Support plate FE model . . . . .	60
Figure 5.4	Experimental vs Simulation results comparison for Support plate . . . . .	61
Figure 5.5	GFRP cooling FE model . . . . .	62
Figure 5.6	Experimental vs Simulation results comparison for GFRP . . . . .	63
Figure 5.7	Scaled temperature dependent elastic properties of GFRP . . . . .	64
Figure 5.8	Scaled temperature dependent elastic properties of Redux® 677 . . . . .	65
Figure 5.9	Thermal expansion coefficient of GFRP . . . . .	66
Figure 5.10	Process simulation thermal analysis FE model . . . . .	67

---

Figure 5.11 Cooling curves of the process simulation . . . . .	67
Figure 5.12 Process simulation mechanical analysis FE model . . . . .	69
Figure 5.13 Tensile, shear and energy release rates used for the bonding agent [24] . . . . .	69
Figure 5.14 Process simulation validation thermal analysis FE model . . . . .	71
Figure 5.15 Cooling curves of the process validation simulation . . . . .	71
Figure 5.16 Process simulation validation mechanical analysis FE model . . . . .	72
Figure 5.17 Plasticity data legitimized by Swift-voce relation Vs Tensile tests of DP980 . . . . .	73
Figure 5.18 Steel specimen bending simulation FE model . . . . .	74
Figure 5.19 Force-Displacement curves of 3PB simulation of Steel . . . . .	74
Figure 5.20 GFRP specimen bending simulation FE model . . . . .	75
Figure 5.21 Sensitivity analysis of parameters thickness and friction coefficient	77
Figure 5.22 Sensitivity analysis of parameters elastic modulus and element size	78
Figure 5.23 Force-Displacement curves of 3PB simulation of GFRP . . . . .	78
Figure 5.24 Hybrid specimen bending simulation FE model . . . . .	79
Figure 5.25 Force-Displacement curves of 3PB simulation of Hybrid specimen	80
Figure 6.1 Components analyzed in Toyota Camry . . . . .	81
Figure 6.2 Front seat cross members in Toyota Camry . . . . .	82
Figure 6.3 Plasticity comparison between basis and V064 . . . . .	83
Figure 6.4 Intrusion comparison between basis and V064 . . . . .	83
Figure 6.5 Spot weld failure comparison between basis and V064 . . . . .	83
Figure 6.6 Adhesive failure comparison between basis and V064 . . . . .	83
Figure 6.7 Material failure comparison between basis and V064 . . . . .	84
Figure 6.8 Rear seat cross members in Toyota Camry . . . . .	84
Figure 6.9 Plasticity comparison between basis and V065 . . . . .	85
Figure 6.10 Intrusion comparison between basis and V065 . . . . .	85
Figure 6.11 Spot weld failure comparison between basis and V065 . . . . .	85
Figure 6.12 Adhesive failure comparison between basis and V065 . . . . .	85
Figure 6.13 Material failure comparison between basis and V065 . . . . .	86
Figure 6.14 Mid rail outer component in Toyota Camry . . . . .	86
Figure 6.15 Plasticity comparison between basis and V068 . . . . .	87
Figure 6.16 Intrusion comparison between basis and V068 . . . . .	87
Figure 6.17 Spot weld failure comparison between basis and V068 . . . . .	87
Figure 6.18 Adhesive failure comparison between basis and V068 . . . . .	88
Figure 6.19 Material failure comparison between basis and V068 . . . . .	88
Figure 6.20 Rear seat cross member reinforced with patch thickness 5 mm . . . . .	90
Figure 6.21 Plasticity comparison between basis and V095 . . . . .	91
Figure 6.22 Intrusion comparison between basis and V095 . . . . .	91
Figure 6.23 Spot weld failure comparison between basis and V095 . . . . .	91
Figure 6.24 Adhesive failure comparison between basis and V095 . . . . .	91

---

---

Figure 6.25 Material failure comparison between basis and V095 . . . . .	92
Figure 6.26 Rear seat cross member reinforced with patch thickness 3 mm . . . . .	93
Figure 6.27 Plasticity comparison between basis and V097 . . . . .	93
Figure 6.28 Intrusion comparison between basis and V097 . . . . .	93
Figure 6.29 Spot weld failure comparison between basis and V097 . . . . .	94
Figure 6.30 Adhesive failure comparison between basis and V097 . . . . .	94
Figure 6.31 Material failure comparison between basis and V097 . . . . .	94
Figure 6.32 Intrusion comparison between basis, V095 & V097 . . . . .	95
Figure 6.33 Hybrid part process simulation thermal analysis FE model . . . . .	96
Figure 6.34 Hybrid part process simulation thermal analysis FE model . . . . .	97
Figure 7.1 Temperature distribution of hybrid plate components . . . . .	98
Figure 7.2 Temperature distribution on upper and lower surface of GFRP . . . . .	99
Figure 7.3 Magnitude of displacement of the hybrid plate components based on isotropic CTE of GFRP . . . . .	100
Figure 7.4 Scalar stiffness degradation and damage initiation criterion results of the bonding agent based on isotropic CTE of GFRP . . . . .	101
Figure 7.5 Magnitude of displacement of the hybrid plate components based on orthotropic CTE of GFRP . . . . .	102
Figure 7.6 Scalar stiffness degradation and damage initiation criterion results of the bonding agent based on orthotropic CTE of GFRP . . . . .	102
Figure 7.7 Comparison of displacements for the GFRP adherend based on isotropic and orthotropic thermal expansion coefficients . . . . .	103
Figure 7.8 Comparison of displacements for the GFRP lower surface not fixed based on isotropic thermal expansion coefficient . . . . .	104
Figure 7.9 Scalar stiffness degradation and damage initiation criterion results of the bonding agent . . . . .	104
Figure 7.10 Temperature distribution of hybrid plate components of process validation simulation . . . . .	105
Figure 7.11 Displacement of the steel part based upon the different boundary conditions . . . . .	106
Figure 7.12 Steel part simulation displacements Vs experimentally measured deflections before and after experiments . . . . .	106
Figure 7.13 Steel part simulation displacements based on increase and decrease of CTE of GFRP . . . . .	107
Figure 7.14 Steel part displacement scaled view . . . . .	108
Figure 7.15 Steel part simulation displacements Vs experimentally measured deflections before and after experiments . . . . .	108
Figure 7.16 Thermal analysis results of the hybrid part . . . . .	109
Figure 7.17 Displacement results of the hybrid part . . . . .	110
Figure 7.18 Overall displacement results of the hybrid part . . . . .	110

---

Figure 7.19 QUADSCRT and SDEG values of bonding agent in the hybrid component . . . . .	110
---	-----

# List of Tables

Table 4.1	DP980 Steel 3PB specimen measurements . . . . .	53
Table 4.2	GFRP 3PB specimen measurements . . . . .	54
Table 4.3	Weight measurements before and after drying . . . . .	55
Table 4.4	Hybrid 3PB specimen measurements . . . . .	55
Table 5.1	Thermal properties used for Steel FE model [25] . . . . .	58
Table 5.2	Temperature-dependent film coefficients finalized for Steel plate . . . . .	59
Table 5.3	Thermal properties used for Support plate FE model [26] . . . . .	60
Table 5.4	Temperature-dependent film coefficients finalized for Support plate . . . . .	62
Table 5.5	Thermal properties used for GFRP FE model [27] . . . . .	62
Table 5.6	Thermal conductivity of GFRP in unit convention $\text{mW mm}^{-1}\text{K}^{-1}$ [27]	63
Table 5.7	Temperature-dependent film coefficients finalized for GFRP . . . . .	64
Table 5.8	Thermal properties used for Bonding agent [28] . . . . .	68
Table 5.9	Mechanical properties of components of hybrid plate [29, 30, 31] . . . . .	69
Table 5.10	Thermal expansion coefficients used for Redux® 677 [28] . . . . .	70
Table 5.11	Elastic properties of GFRP [32] . . . . .	76
Table 5.12	GFRP properties used in simulation[32] . . . . .	76
Table 5.13	Material parameters used for Redux® 677 [33] . . . . .	79
Table 6.1	Component characteristics comparison between basis and V064 . . . . .	82
Table 6.2	Component characteristics comparison between basis and V065 . . . . .	84
Table 6.3	Component characteristics comparison between basis and V068 . . . . .	87
Table 6.4	Critical components prioritized based on potential analysis . . . . .	89
Table 6.5	Component characteristics comparison between basis and V095 . . . . .	90
Table 6.6	Component characteristics comparison between basis and V097 . . . . .	92
Table 6.7	Failure time comparison between basis, V095 & V097 . . . . .	95
Table 7.1	Isotropic temperature dependent thermal expansion coefficients of GFRP . . . . .	100
Table 7.2	Orthotropic temperature dependent thermal expansion coefficients of GFRP [34] . . . . .	101
Table 7.3	Displacements of the steel part based on different rates of CTE of GFRP . . . . .	107

# List of Variables

Symbol	Property	Unit
$\rho$	Density	ton mm <sup>-3</sup>
$k$	Thermal conductivity	mW mm <sup>-1</sup> K <sup>-1</sup>
$E_{11}$	Young's modulus in the principal direction 1	MPa
$E_{22}$	Young's modulus in the principal direction 2	MPa
$E_{33}$	Young's modulus in the principal direction 3	MPa
$\nu_{12}$	Poisson's ratio in the principal direction 1	-
$\nu_{13}$	Poisson's ratio in the principal direction 2	-
$\nu_{23}$	Poisson's ratio in the principal direction 3	-
$G_{12}$	Shear modulus in the principal direction 1	MPa
$G_{13}$	Shear modulus in the principal direction 2	MPa
$G_{23}$	Shear modulus in the principal direction 3	MPa

# 1 Introduction

## 1.1 Background

Rigorous regulations and amendments are revised for energy conservation and also to protect the climate change every year. As part of the automotive industry, the objective of the EU commission is reduction of an 80% to 95% of the GHG (Green house gas) emissions by 2050 compared to 1990 [35]. However, the expectations are such that, the emissions in future can no longer be controlled only through improvements in engine alone. Another possibility of cutting down the fuel consumption is by reducing the vehicle weight [36]. For this purpose, a constructional ideology or philosophy called “Lightweighting” has gained importance over the recent years [37]. Weight reduction of 100kg in the vehicle saves approx. 0.3 - 0.4 litres of fuel per 100 km, provided that the drive train and chassis are also adapted to the reduced weight [38].

One such aspect of the lightweight construction technique is that, modern lightweight materials such as FRP's can be used as a pure substitute instead of the metallic joining partners. Before the year 2006, the fiber-reinforced materials were used only in high-end applications such as aviation, aerospace and Formula1 racing segment. But in the recent years the trend of high-strength composites play a major role due to their potential in lightweight construction [2]. A precedent of its potential is the use of composite laminates in Boeing 787 Dreamliner and Airbus A350 which exceeds 50% of the vehicle weight [39]. Also in the automotive series production, the BIW (Body in white) of BMW i and BMW 7 series constituted numerous components made out of CFRP (Carbon fiber reinforced polymer) which came out in 2013 and 2015 respectively [36]. Because of the high material cost of the composites, using them as a authentic substitute will not be feasible in the near future. A prospect of reducing those high costs is manufacturing the car segments by integrating the Metal-FRP component as one called as Hybridization [40].

## 1.2 Motivation

The multi-component system plays a crucial role as it performs exceptionally well during crash. The higher load carrying abilities along with larger energy absorption makes it a superior choice over a individual traditional metal sheet [41]. The method of joining the components influences the structural efficiency since the joints are the weakest part of the structure. There are two joining approaches. Mechanical and Ad-

hesively bonded joints [42]. Adhesive joints are preferred over mechanical fastening in some non-critical areas such as non-flight critical aircraft components in smaller aircraft because they appertain to eliminate stress concentrations [43] and also gets rid complex preparation of the components for the mechanical connections. Apart from the two joining processes there are also some thermal joining processes which can be used to produce Metal-FRP parts [44]. Those methods include Bulk heating, Frictional heating, Electromagnetic heating and two-stage techniques [9]. In this work, one among such heating methods is used where a glass fiber reinforced thermoplastic is heated, pressed and cured onto the metallic part. The process is called co-curing [10] and an additional epoxy film is also co-cured to increase the bonding strength of the hybrid part. As per current state of the art, very few researches combining the co-curing and adhesive bonding are investigated. Even then the investigations were purely experimental. So, this process should be validated against the experiments to establish a systematic method and also to identify the relative displacements of the multi-material BIW structures.

### 1.3 Goal

Therefore, the combination of the post-molding technique and adhesive bonding is examined both experimentally and using FEM technique. The content of this work is to manufacture hybrid plates made out of Steel, GFRP (Glass fiber reinforced polymer) and epoxy glue film Redux®677. The primary focus is to evaluate and validate the process by comparing the temperatures and deformations of a hybrid plate by devising a process simulation method using FEM software ABAQUS™. The next step is to validate the material model of each of these materials and evaluate the strength on 3-point bending hybrid specimens both experimentally and numerically. Finally, a potential analysis to identify the critical components of the Toyota Camry model available at GNS mbH which could affect the crash performance should be accomplished. Then the formulated process simulation method is transferred to the decisive variant and analysis of the stresses and deformations is to be carried out.

Prior to Chapter 2, a preface to Metal-FRP connections used in BIW construction, the simulation and experimental methods of process as well as structural validations is extensively carried out. In order to gain profound knowledge about this process, a comprehensive description about the process parameters influencing the process is also provided in the following chapter.

## 2 State of the art

This unit covers the basic concepts such as the use of metal and FRP's in BIW construction, the experimental methods which had been carried out for the process and the mechanical tests followed by the simulation approaches performed previously about this topic. Finally some prospects which needs to be considered with producing the multi-material connections using this process is elaborated.

### 2.1 Hybrid construction of BIW structure

The prime motive of multi-material connections in BIW is to reduce the weight of the structure which can further reduce the emissions and to improve the stiffnesses compared to the reference system. Therefore, it is important to know about the diverse methods of the weight reduction.

The different strategies of the lightweight design are:

- **Material lightweight design**
- Structure lightweight design
- System lightweight design

Of these three strategies, material lightweight design employs the use of the property of single material or combine two different materials to form a hybrid. This strategy is a subgroup of the structure lightweight design which changes the shape and design to reduce the weight while keeping the stiffness on an increase or maintaining it as constant. In the subsequent section, the material lightweight design is concentrated as this is fundamentally associated with this topic [37].

In the manufacturing of multi-material components, Aluminium had been used as a substitute for Steel over the recent years. An illustration of this is a Porsche 911 which is made up of a mix of Steel, Aluminium and 2% Magnesium. In this, 44% of the body is made up of Aluminium, where the aluminium sheets are connected to the steel components. This is illustrated in Figure 2.1. Another example of this is the BMW 5 series where the doors, the front flap and the front side panel are made up of Aluminium. In the BMW 7 series the roof is also made up of Aluminium whereas the entire body is made up of Steel. Even though Aluminium is used at increasing rate, FRP's have gained attention over the past decade because of its excellent mechanical properties. Still due to the high material, production cost and long processing time, the FRP's has failed on a large-scale production case [1].

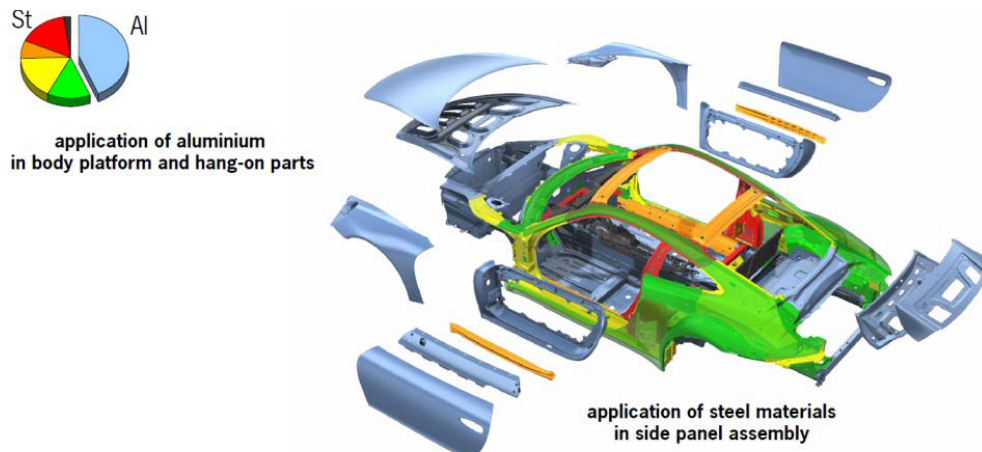


Figure 2.1: Porsche 911 BIW [1]

In volume or high performance applications only the continuous GFRP and CFRP are used. Based on the polymer category and two different fibers, the combination sets are shown in 2.2 and compared [2].

Application examples	CARBON-FIBER-REINFORCED PLASTICS (CFRP)		GLASS-FIBER-REINFORCED PLASTICS (GFRP)	
	Carbon fiber	Thermo-set	Glass fiber	Thermo-set
Source: Lamborghini	Source: ENG3D Austria	Source: Lawless		
Stiffness	⬆️	➡️	➡️	➡️
Strength	⬆️	➡️	➡️	➡️
Weight	⬇️	➡️	➡️	➡️
Cost	⬆️	➡️	➡️	⬇️
"Best mechanical properties but highest cost"		"High impact resistance and short cycle time"		"Reduced mech. properties but cost advantage"
"Short cycle times and attractive cost profile"				
⬆️ High (compared to each other)	⬇️ Low (compared to each other)			

Figure 2.2: Comparison of CFRP and GFRP properties [2]

The FRP material has superior characteristics over the conventional steel such as high strength-to-weight ratio, excellent corrosion resistance and high tensile strength, ease to transport and install. Another notable feature of FRP is its capacity to follow curved and irregular surfaces of a structure, which is tough to accomplish using steel plates. The material properties of FRP in multiple directions can be modified for a specific application, which is another advantage [45]. Inspite of the exceptional characteristics of FRP over metals, there are also some drawbacks such as low

ductility and poor impact resistance. Another disadvantage is that if the matrix layer is based on thermoset polymer then it takes long processing cycle to cure the matrix which further increases the production time [46]. In order to overcome this, the FRP's based on thermoplastic matrix is recommended as it have significant gain over the thermoset based FRP's such as excellent energy-absorption properties [47] and environmental favors like recyclability, post forming and rapid processing which reduces production time and associated manufacturing costs [48].

However it would be meaningful only if the right material is used at the right place in right quantity. In this strategy for weight reduction, the share of lightweight materials is 70%, the concept of construction shares 20% and the new joining techniques shares 10%. The properties of the materials which determines its use is represented in figure 2.3.

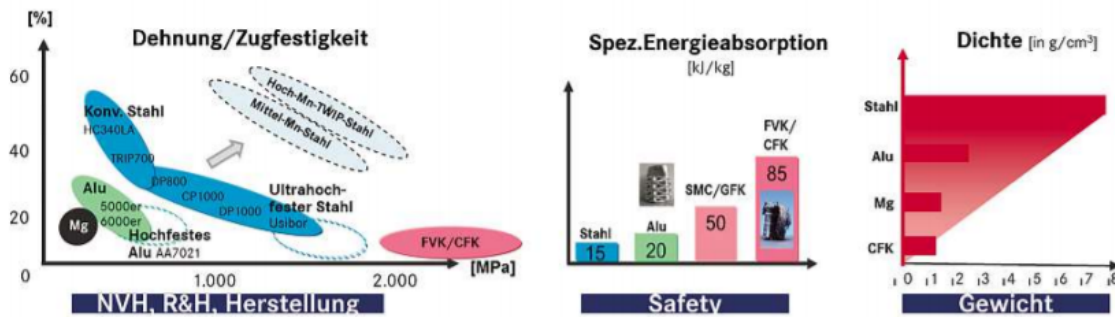


Figure 2.3: Material properties which determines the use [3]

This can be clarified such that due to its high tensile strength and excellent NVH properties Steel remains predestined for certain applications. Aluminium has weight advantages but sometimes need more insulation material. FRP cannot be used in body shell parts as it tends to be involved in the dryer at about 180° C after the CDC (Cataphoretic dip coating) process. Currently, the OEM (Original equipment manufacturer) such as Daimler uses plastics on the outer skin assembly parts so that it does not have to go through the dryer [3].

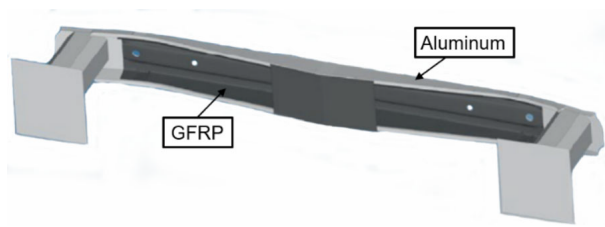
### 2.1.1 Metal-FRP connections

Using the advantages of metal materials such as good toughness and impact resistance along with the FRP's benefits will help to overcome [49] those drawbacks discussed in section 2.1. Hence, the hybridization of the metal and FRP components is the technique that the industries are adapting. A depiction of this in figure 2.4a is a hybrid design A-pillar which is made up of high strength steel and short glass fibers reinforced within polyamide 6 resin bonded by friction with the L-5235 structural foam. Without compromising the strength and rigidity provided by the previous structure made of high-strength steel tubes, the weight of this hybrid part is reduced by 5 kg and also improved vehicle dynamics by lowering the car's center of gravity

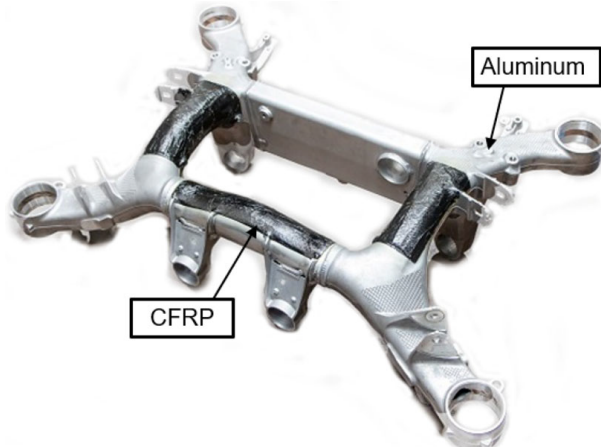
[50]. In the figure 2.4b, is shown a fiber reinforced plastic patch in the front bumper made up of Aluminium. This joining concept is made with two different adhesives namely 1-component epoxy adhesive film and 2-component polyurethane adhesive film. This hybrid component weighs 45% less than Steel-Aluminium reference. Also this crash management system was validated using three-point bending test and found that the maximum force absorbed can be increased by 11% compared to the reference system [51].



(a) Hybrid A-pillar [50]



(b) Hybrid front bumper [51]



(c) Hybrid subframe [41]

Figure 2.4: Hybrid automotive components

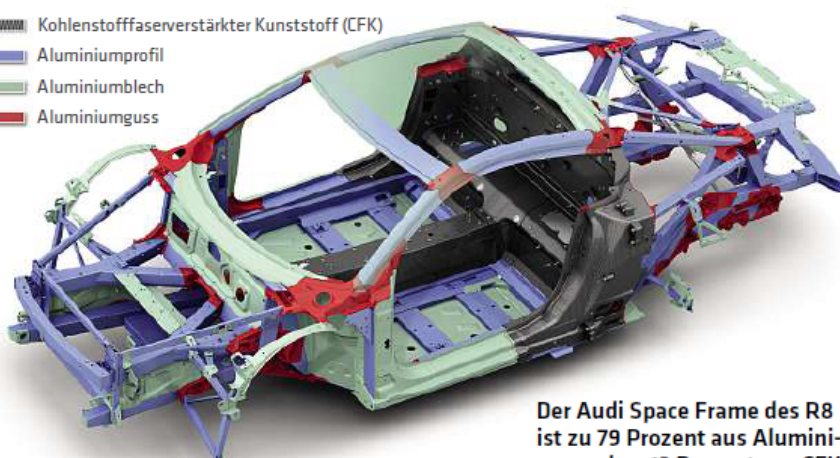
A 500g fast curing CFRP prepreg reinforced on an aluminium subframe shown in figure 2.4c has a beneficial impact on the overall NVH performance and also reducing the load of the structure to a certain extent when compared with all metal components [41]. This shows that even by reinforcing a bare amount of FRP can have consequential effect on the structure.

The Audi group has with then the Audi R8 in figure 2.5 where the space frame weighs about 200 kg and is 10 kg less than before. But the reinforced structure is extremely stiff and crash-proof. Space frame is composed of 79% Aluminium and 13% CFRP. The CFRP is used in the areas such as the rear wall, central tunnel where it achieves even better results than Aluminium. The fabric layers of the cross members of the rear wall is unidirectional and the finished component has very high tensile strength of about 2000 MPa. To decide the final concept where this material could be placed the simulation models with different crash and stiffness load cases were played through. If there are certain components which cannot be calculated through the simulation, then they were not installed or included in the final concept [3].

### → AUDI R8 COUPÉ

Audi Space Frame in Multimaterialbauweise

- Kohlenstofffaserverstärkter Kunststoff (CFK)
- Aluminiumprofil
- Aluminiumblech
- Aluminiumguss



Der Audi Space Frame des R8 ist zu 79 Prozent aus Aluminium und zu 13 Prozent aus CFK.

Figure 2.5: Audi R8 Space Frame [3]

In another study, the center-pillar reinforcements made from steel tailor welded blanks (TWB) and CR420 steel/carbon-fiber-reinforced plastic (CR420/CFRP) hybrid composite materials were compared by collision tests to assess the fracture toughness of the hybrid composite material. The figure 2.6 shows the TWB of cold rolled steel sheets of thicknesses 2 and 3mm. The bottom part of the figure shows the CFRP of  $0.22\text{ mm} \times 8\text{ ply} = 1.76\text{ mm}$  (thickness after curing) was stacked over the CR420 of thickness 1.4mm. This hybrid component is formed by using a press to compress it at 0.5 MPa while the CFRP was heated at 140°C and cured for 30 minutes. The resulted component is subjected to collision test and compared to the experimental collision test result from TWB's of CR420. It was found that weight of the center-pillar reinforcement made from TWB was 1487g and the hybrid component weighed about 830g which is 44% less than the TWB's of CR420. Further to this, crashworthiness was also improved by 10%. This is because of the low elongation rate of the CFRP which is on the upper side of the hybrid component [4].

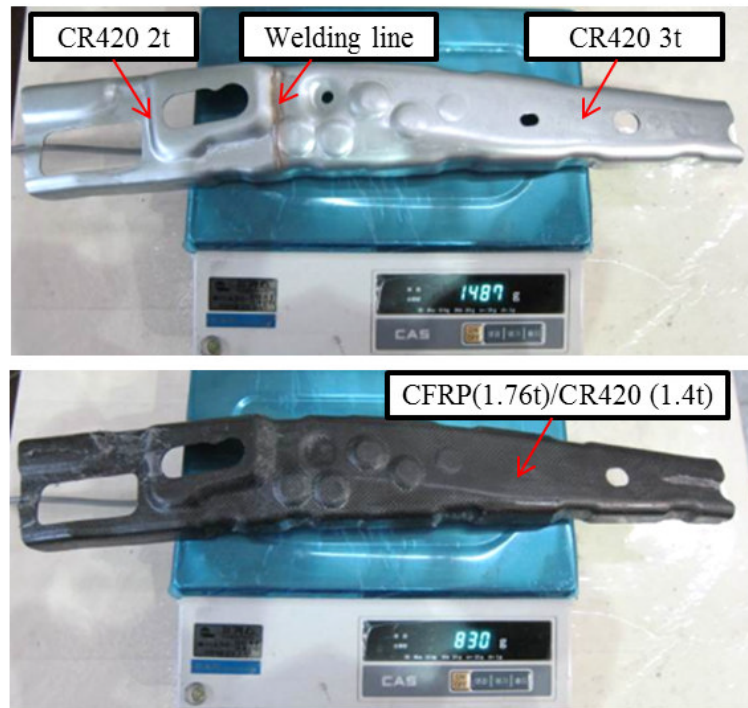


Figure 2.6: Comparison of weight of steel TWB and CR420/CFRP composite [4]

There are some researches related to the concept basis in the metal-FRP connections in BIW. One instance of that is the side frame inner reinforcements of the BMW M6 Sports car depicted in figure 2.7 must be totally modified to deliver a resulting mass of 40 kg when developed in steel to fulfill higher functional standards in terms of collision. By replacing steel with carbon fiber composites, reinforcements with a mass of just 25 kg will be produced, resulting in a mass reduction of at least 37.5%. This is one such illustration of the application of fiber reinforced plastics in the experimental BIW [5].

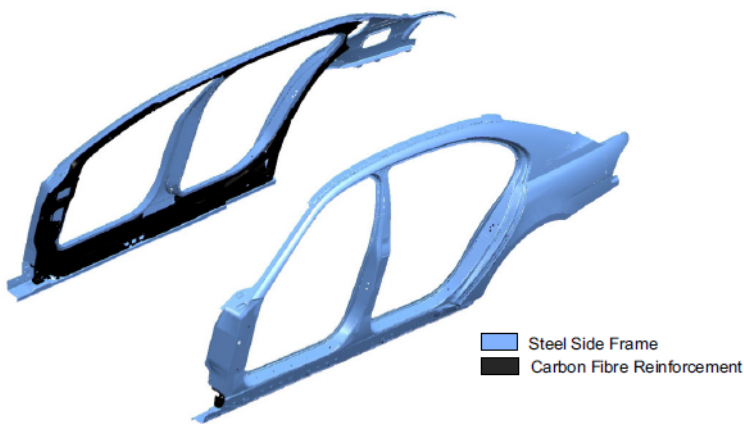


Figure 2.7: Illustration of CFRP reinforcement in experimental BIW of BMW M6 [5]

In the year 2013, the BMW Group has demonstrated that the techniques for manufacturing FRP are adequate for large-scale production with the CFRP electric vehicles

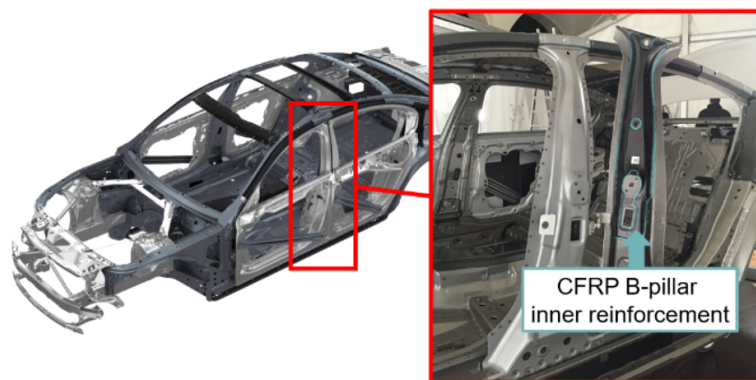


Figure 2.8: Hybrid B-pillar assembly made of Steel and CFRP in BMW M7 [6]

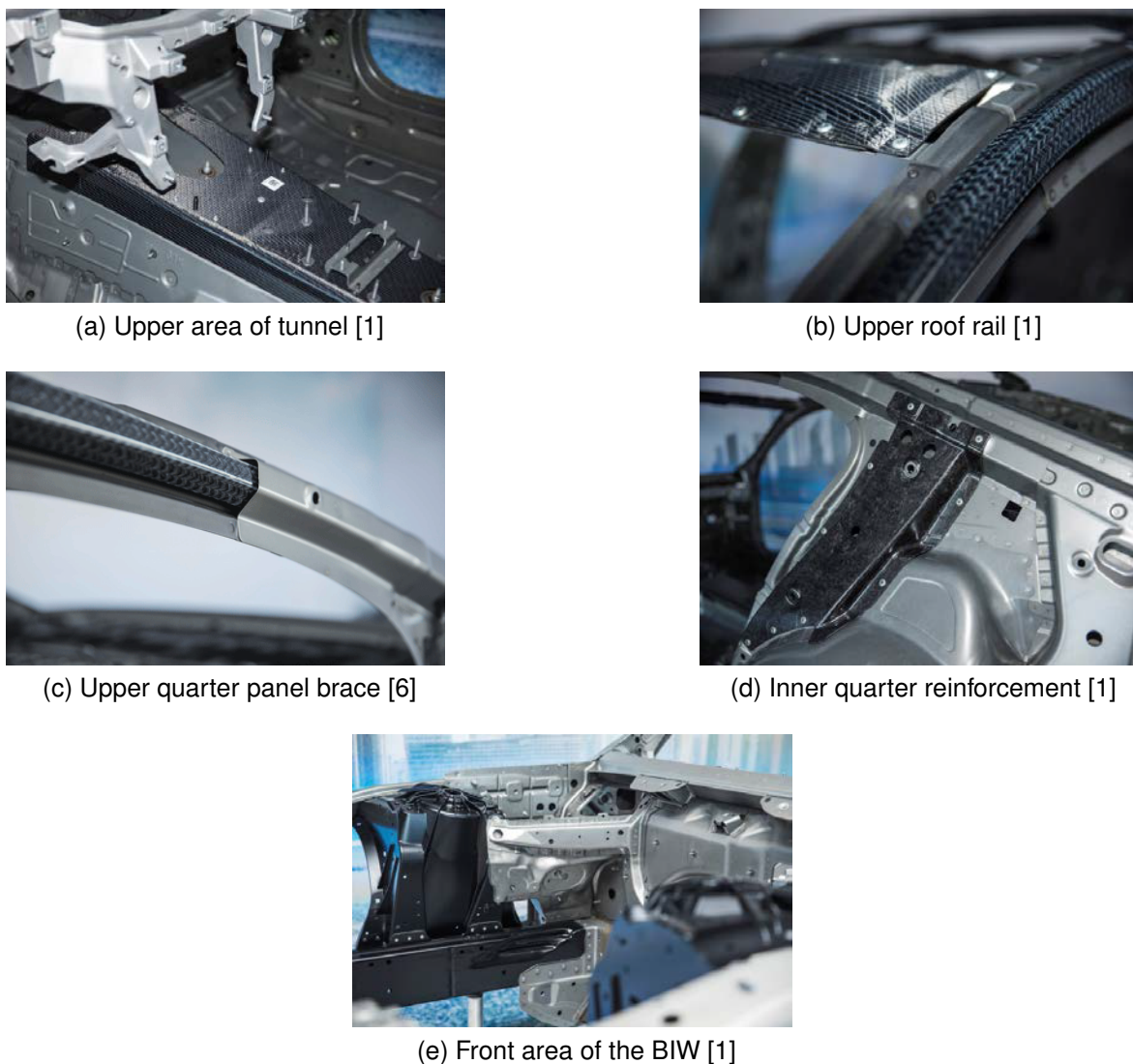


Figure 2.9: Aluminium and CFRP integrated parts in Carbon core in BMW M7

BMW i3 and i8. With the BMW 7 series in 2016, a feature called as the carbon core blends the carbon fiber, aluminium and high-strength steel components together.

The B-pillar is reinforced with CFRP shown in figure 2.8 by rivet bonding which reduces the weight of the BIW structure [6]. Also, there were some other regions such as the upper side of the tunnel area in figure 2.9a , C-pillar, roof bows, rocker panel reinforcement, upper roof rail reinforcement in figure 2.9b, upper quarter panel brace in figure 2.9c, inner quarter reinforcement shown in figure 2.9d and also the front area of the struthousing in figure 2.9e. This enables the body weight to be reduced by 40 kg and the overall vehicle weight to be reduced up to 130 kg compared to the predecessor model [1].

Not only the FRP, there are many other materials such as magnesium and other types of casting and plastic materials which plays an important role in the lightweight construction. Those examples are discussed briefly in this part. SLC (SuperLight-Car) depicted in figure 2.10 is an example of that kind of multi-material construction where it employs Steel, Aluminium, Magnesium and fiber reinforced plastics which can significantly reduce the weight of the mid-range passenger cars by 35% [7].

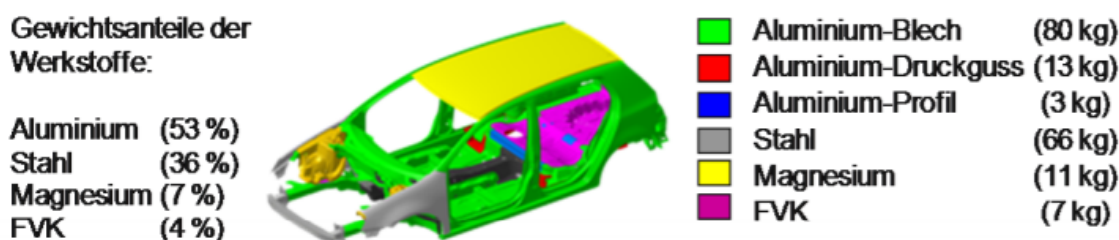


Figure 2.10: Multi-material BIW of the SLC [7]

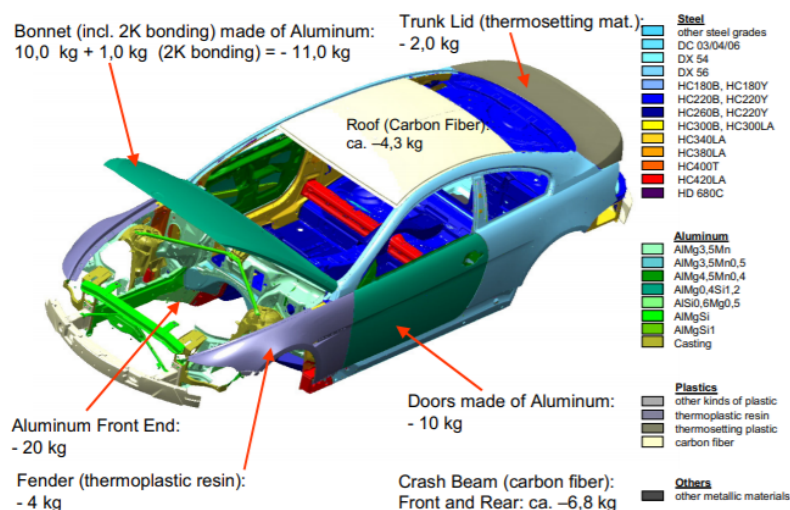


Figure 2.11: Weight savings of the multi-material BMW M6 [5]

According to the value proposition philosophy, weight reduction is done in the BMW M6 sports car shown in figure 2.11 with different materials such as front structure

with aluminium hood, aluminium front end and thermoplastic side panel. To achieve equal load distribution between the front and rear axle, advanced high strength and multiphase steel components were made in the middle. The fender and trunk lid is made up of different types of plastics so as to save the cost. Also the roof is made of carbon fiber to lower the center of gravity [5].

Another demonstration of this type of construction is the seat structure presented in figure 2.12 where the seat rails, portions of the seat shell, and the rear seat back inserts are made of high-strength steel grades. It is predicted that the usage of hybrid construction in seat structures forecasts a lightweight potential construction of 15 to 20%. The usage of different materials such as Aluminium, Steel and plastics in seat structures will lead to a weight saving of 4 kg when compared to the steel solution [7].

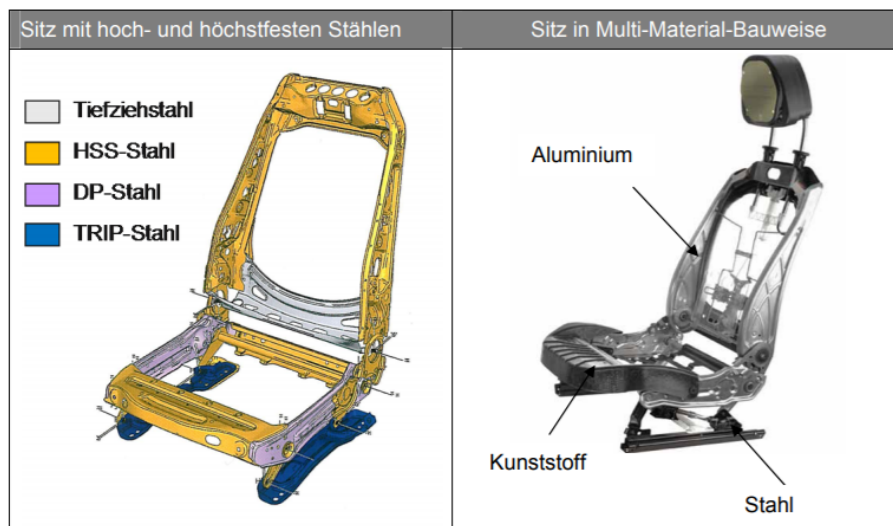


Figure 2.12: Lightweight seat structure [7]

Even though this construction technique has many advantages over the existing philosophy, there arises certain problem such as the joining technology due to the different electrochemical potentials and thermal expansion coefficient [7]. Also the adhesive technology and the CTE-mismatch problems have to be thoroughly investigated [1].

## 2.2 Experimental techniques

In this section, the established different fusion bonding techniques which has been adapted in the Metal-FRP connections are elaborated for the process as well as the mechanical tests which are used to evaluate the bond strength.

## 2.2.1 Fusion bonding - An introduction

In this section, an outset to the fusion bonding process is briefly discussed. There are three basic joining technologies which is used to join the metals and polymeric materials. They are as follows:

- Mechanical fastening
- Adhesive bonding
- **Fusion bonding**

Comparing the two former techniques, adhesive bonding was considered in many places than the mechanical fastening as discussed in the section 1.2. But it has a disadvantage that, the structural adhesives used in the BIW construction attains its final strength in the drying oven after the CDC process [52]. In order to overcome this drawback, the latter of the above mentioned two processes namely the fusion bonding comes into picture. In this approach shown in figure 2.13, the metal joining partner is heated above the melting temperature of fiber-reinforced TPMC (Thermoplastic matrix composite) or TSMC (Thermoset matrix composite) and once the joining temperature is reached the fiber-reinforced composite is pressed under a defined force to the heated metal partner. The matrix resin then melts (here referred to as hot melt adhesive) and wets the metal surface and the bond is obtained after a holding and cooling under pressure phase. Thus a consolidation is obtained at the interface of the two different substrates [8]. This technique reduces stress concentrations unlike adhesive bonding technique and also reduces the processing time, surface preparation requirements and enhances durability [9].

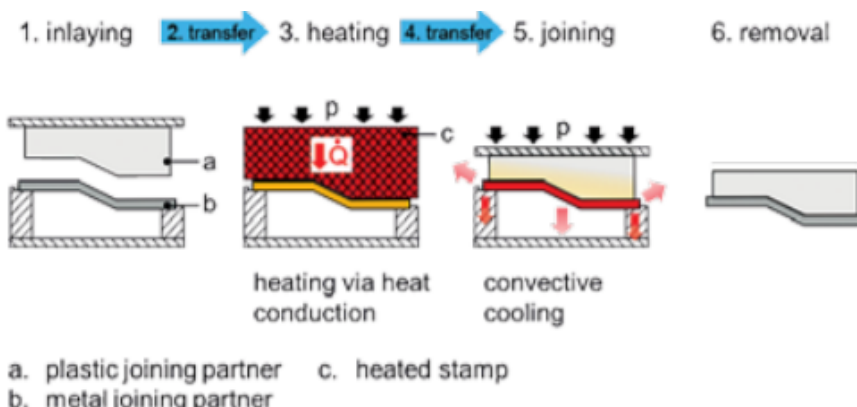


Figure 2.13: Illustration of fusion bonding process [8]

Based on the source used for introducing heat, fusion bonding techniques are classified as displayed in figure 2.14. Of the different techniques which are available, the bulk heating procedures are of the main focus here since it is being used in the automotive industries. From the process point of view, the approaches other than bulk

heating involves heating up only small areas in the vicinity of bonding and minimises the impact effects on the rest of the structure. But from the joint performance point of view, the bulk heating methods are advantageous since no surface preparation is required and the bond strength is equal to that of the parent materials [9].

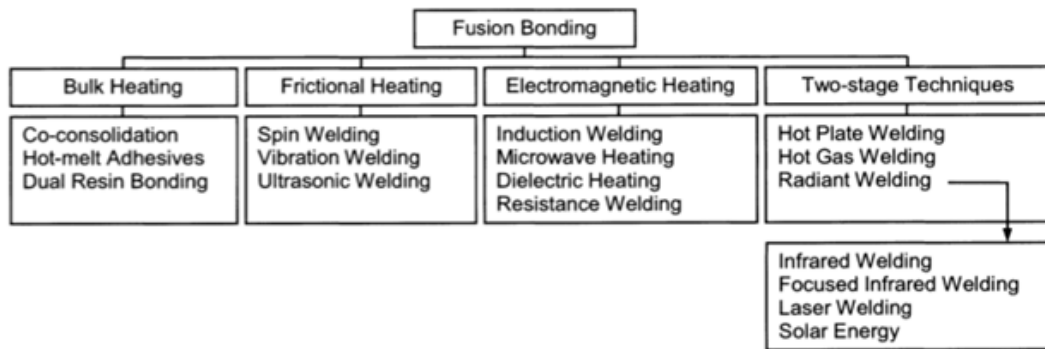


Figure 2.14: Illustration of fusion bonding process [9]

## 2.2.2 Process

One such technique which is done in [10] forms the base of this work which uses the *Hot-melt adhesive* technique where it also employs an additional glue film apart from the resin present in the composite material. In this study, hybrid plates were manufactured from high-strength dual-phase steel (HC660XD) and a pre-impregnated continuous unidirectional glass-fibre reinforced epoxy material (prepreg) with fast-curing abilities. An additional modified epoxy adhesive film Redux®677 is co-cured with the GFRP onto the Steel plate. The manufacturing of hybrid plates is done with a setup shown in figure 2.15.

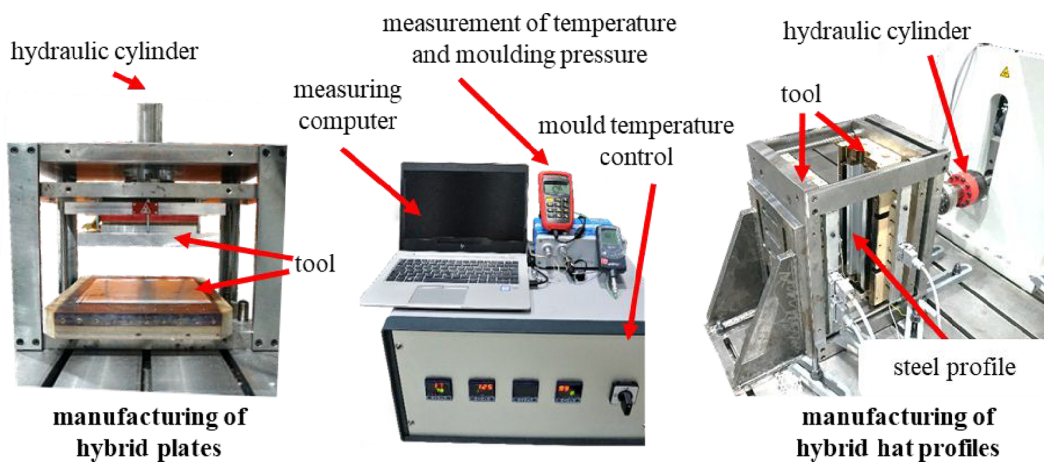


Figure 2.15: Setup for manufacturing hybrid plates [10]

The temperature and pressure settings such as moulding tools heated upto 180 °C and a moulding pressure of 0.18 MPa was used. The moulding time was about 30

seconds for hybrid plate without additional glue film and about 60 seconds with additional glue film. Also the hybrid plates were heated at 180 °C for about 30 minutes after the manufacturing process to simulate the e-coat drying process. But there are only few researches [17, 53, 54, 55] which adapt this method of producing the hybrid constructions and also rarely explains the process approaches. Although this is the base of this research there are also some investigations which are related to the conventional fusion bonding and explains the process. This could be of interest to adapt those approaches to the underlying base technique of this research. Hence they are discussed elaborately in the subsequent reading.

In [11], quadratic steel (25 x 25 x 0.6 mm) and plastic (polyamide 6) plates (25 x 25 x 2 mm) were used to demonstrate the process. A mechanical device was modelled for homogenous heat transfer from joining device to metal plate with the help of heating elements as displayed in Figure 2.16.

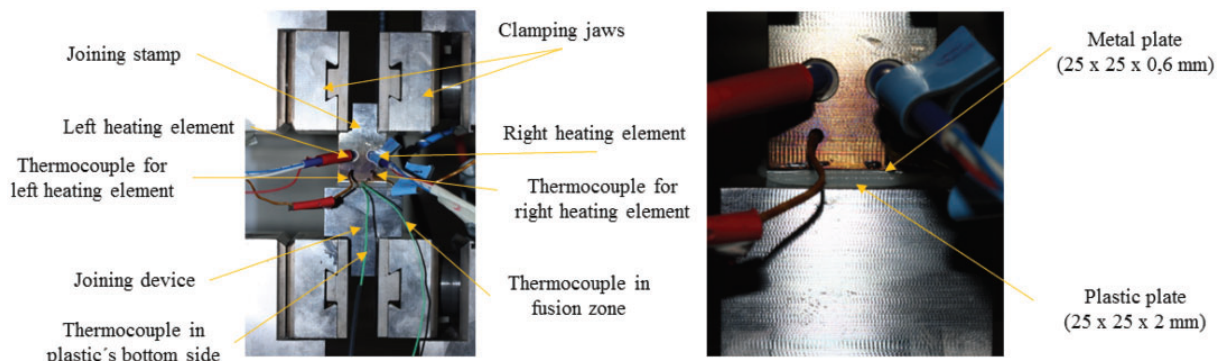


Figure 2.16: Manufacturing setup [11]

As the concept of conventional process lies in heating the metal part alone and conducting the heat from the metal to plastic, the heating rate was maintained at 50K/min to attain the desired temperature of 230 °C at the joining zone of metal and plastic which is above the melting point of polyamide 6. Once the plastic starts to melt different joining forces of 75N, 150N, 300N was applied constantly and maintained for about 10 seconds. This holding time is responsible for the plastic to wet the metal surface properly. Then the joining force is released. The focus of this investigation is to measure the maximum outflow or maximum displacement of the melted plastic. A joining device developed in the Cluster of Excellence “Integrative Production Technology for High-Wage Countries“ is examined in [8]. The investigated materials were stainless steel 1.4301 and an aluminium alloy 3.3547 joined in combinations with three different plastic partners such as Polyamide 6, PA6GF30 - Polyamide 6 with 30% weight of short glass fiber reinforcement and PA6GF47 - Polyamide 6 glass fiber content of 47% weight of glass fibers with a 0°/90° twill weave. The principle of joining is the same but with a small variation in the pressure which is being employed to join. The joining equipment and the pressure variation are depicted in the figures

2.17a and 2.17b respectively. The pressure at the initial stage of the process should be high which ensures good heat conduction and wetting of the metal with the thermoplastic. After a certain time  $t_1$ , it must be reduced again to prevent pressing out all the thermoplastic. Again after time  $t_2$ , pressure must be raised again to counteract the thermal contact of the fiber and plastic and also to minimise the residual stress. The overlap shear-strength obtained with this approach is considerably high when compared to the constant joining pressure.

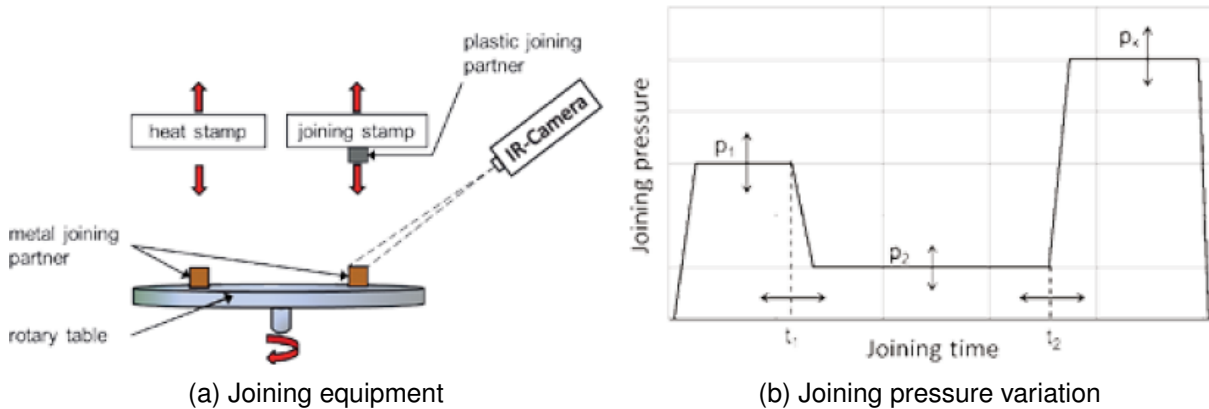


Figure 2.17: Optimised joining apparatus and pressure profile [8]

Another study investigates the effect of different surface treatments and adhesion models used to join Aluminium (AlMg3) of thickness 1.0 mm and CF/PA66 (Carbon fiber reinforced polyamide 66) with a fiber volume fraction of 48% of thickness 2.0 mm [12]. The technique used to join the adherends are based upon one of the electromagnetic heating methods known as the Induction heating. The complete setup is shown in the Figure 2.18.

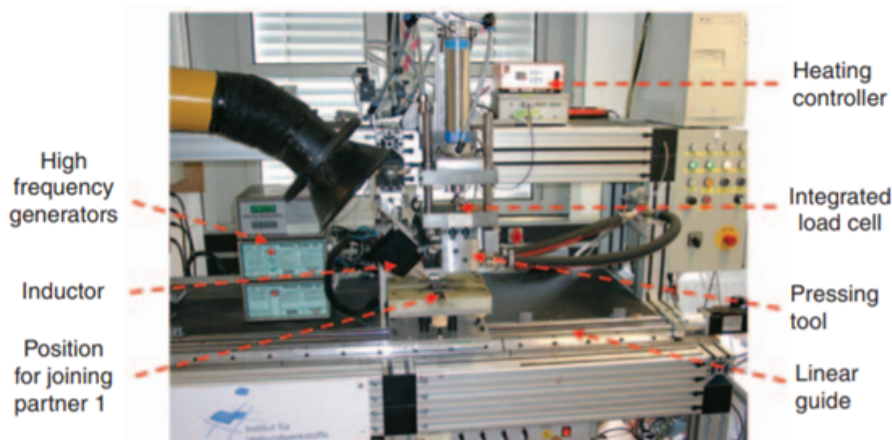


Figure 2.18: Process equipment [12]

This inspection also involves the same principle of heating the metal above the melt-

ing point of the FRP and conducting the heat through to the CF/PA66 depicted in Figure 2.19b to allow it to melt and joined by means of punching tool displayed in Figure 2.19a. The adherends are heated using high frequency generators and after the heating process, it is traversed using the linear guide to the pressing tool and joined by applying pressure as shown in figure 2.18.

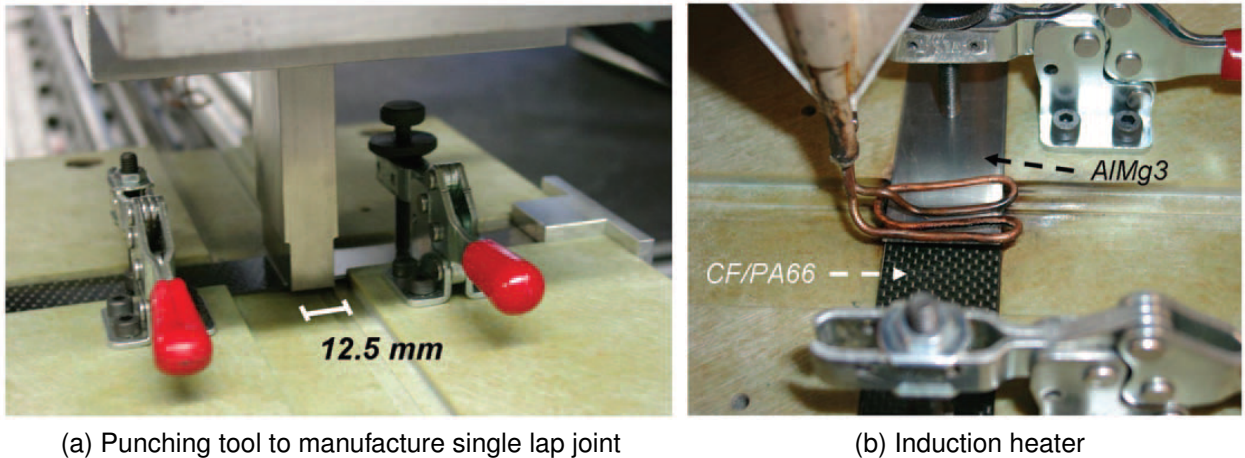


Figure 2.19: Overview of punching tool and induction heater

The target of this analysis is to develop a hybrid joint, determining the influence of different surface treatments of the joining partners and also analyzing the significant process parameters which are involved in the manufacturing process later explained in section 2.4. In [13], fusion bonded hybrid joints made of press hardened steel (22MnB5) coated with AlSi and glass fiber reinforced polyamide 6 matrix are reviewed. The induction heating was used for heating the metal and the infrared emitter represented in Figure 2.20 was used to heat the FRP to bring above its melting temperature. The glass mat reinforced thermoplastic (GMT) is heated for about 2.5 minutes placed on a linear rail while the press hardened steel is heated with inductor.

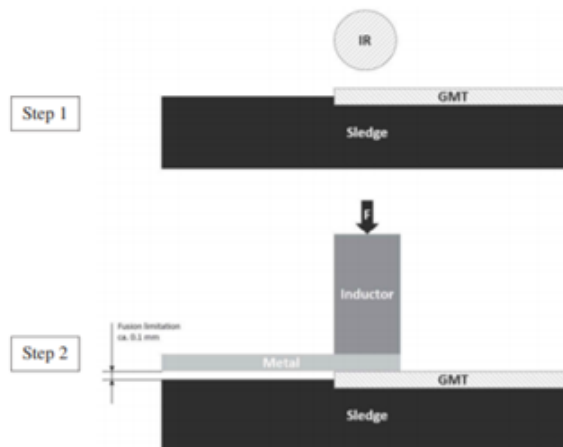


Figure 2.20: Manufacturing setup for lap-shear samples [13]

The metal temperature is varied from 170 °C till 280 °C. The temperature of the GMT starts at 220 °C and increased in steps of 20 °C upto 280 °C. Pyrometer was used to control the temperature of the GMT. Once the desired temperature of the GMT is reached it is moved on the linear rail towards the metal joining partner and the steel adherend is pushed onto the melted GMT. The joining pressure applied was about 0.1 MPa and a cooling time period of about 10 seconds using compressed air. The aim of this investigation is to understand the formation of joining zone of the hybrid joints and to optimize the process parameters. Similar to this investigation, in [14] the pre-treatment of the metal surface using different laser intensities before joining was studied. Also the sensitivity of joining parameters such as joining temperatures, holding time and joining pressure were also examined. The joining partners used were DC01 Steel and thermoplastic glass fiber reinforced polyamide 6 with fiber content of around 60%. The lap shear samples according to the standard DIN EN (Deutsches Institut für Normung Europäische Norm) 1465 were prepared by using inductive heating method of metal and melting the thermoplastic material above its melting point via heat conduction. A constant pressure of about 150 N was applied using two setups specifically using a pressure cylinder and another using universal testing machine displayed in Figure 2.21. At the end of the joining process, both pressure mechanisms used an air pressured cooling system to cool the samples at least for 10 seconds to bring it below the melting temperature of matrix material of the FRP. The pre-treatment of the metal surface using lower and higher laser intensities benefited in achieving higher lap-shear strength. Also the influence of different dwelling times and joining temperature and pressure are discussed elaborately in section 2.4.

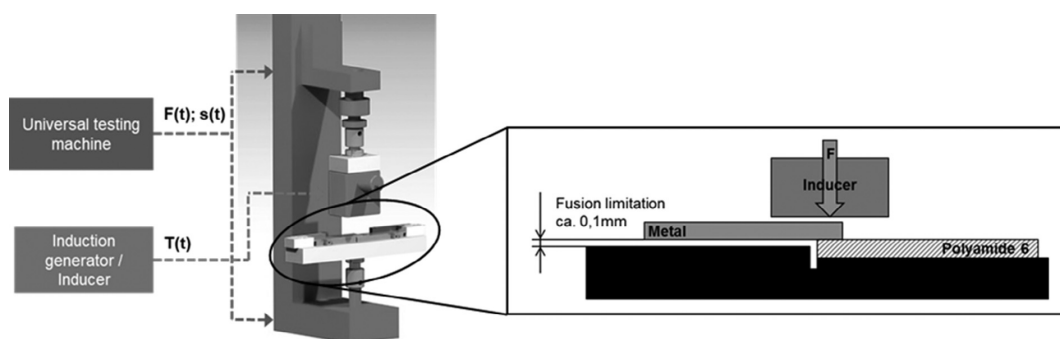


Figure 2.21: Joining setup [14]

All of these investigations belong to the category of discontinuous joining of hybrid materials which requires a significant amount of process steps. In order to minimize those process steps, the investigations related to continuous manufacturing of Steel-FRP structures is pointed out concisely in the following clause. In [15, 55, 56, 57, 58] the aforementioned technique is used for joining the metal adherend DC01 Steel and carbon fiber reinforced thermoplastic tape made of Polyamide 6 resin. The setup is shown in Figure 2.22 where the Steel adherend (200 mm × 25 mm × 1 mm)

is heated by an inductor and the CFR-TP (Carbon fiber reinforced thermoplastic) tape ( $250 \text{ mm} \times 25 \text{ mm} \times 0.19 \text{ mm}$ ) is heated up by hot air gas. The processing speed is controlled by an electric motor and an even speed of about  $11.7 \text{ mm/s}$  is achieved throughout the process. A joining pressure of about  $5.76 \text{ N/mm}^2$  presses the CFR-TP onto the steel sample. The roll which pushes the CFR-TP was coated with polytetrafluoroethylene tape to prevent an adhesion between the tape and itself.

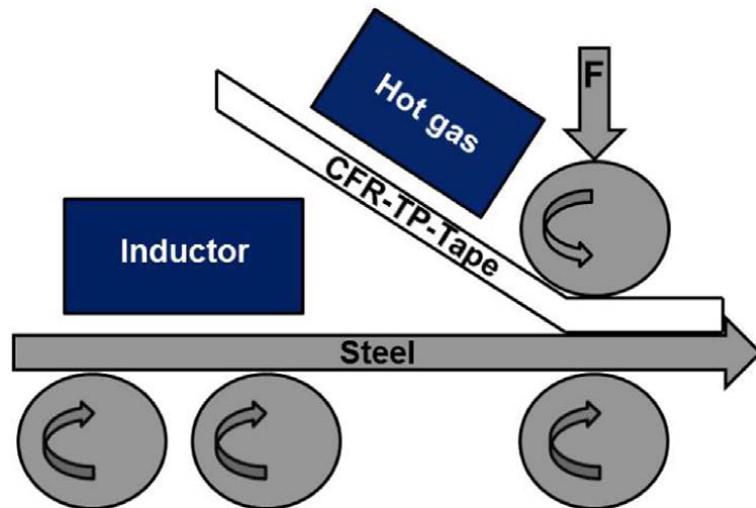


Figure 2.22: Test setup [15]

Thus, a complete understanding of the fusion bonding process is achieved through this section and the experimental mechanical tests for characterizing the material properties and deformation behavior of the hybrid structures is intricately in the next section.

### 2.2.3 Mechanical tests

The mechanical characteristics during the preparation of a hybrid composite were tested by different mechanical tests such as bending, tensile and lap shear [59]. But mainly the fusion bonded hybrid joints were tested by lap shear tests [12, 13, 14, 58, 60, 61]. Specifically in [14], the lap shear tests characterized the lap-shear strength of the specimens tested at different operating temperatures from  $-40^\circ \text{ C}$  to  $200^\circ \text{ C}$ . The Short beam strength (SBS) test was performed in [62] to assess the interlaminar shear strength of the fusion bonded carbon fabric reinforced polyphenylene sulphide. Also in [63], comparison was made to evaluate the shear strength between the results of ILSS (Interlaminar shear strength) test and edge shear test. However the authors showed that the ILSS test might not be appropriate since it overestimated the measured shear strength which was also due to the interference of other failure modes which were not caused by shear loads. In [8], along with overlap shear specimen tests, box geometry was used to investigate the joining of complex geometries

and to test the impermeability. For the continuously fusion bonded hybrid structures there were some appropriate testing methods employed. Some of them are climbing drum peel test [55, 56], floating roller peel test [15, 57].

Apart from the above-mentioned tests the most pertinent test method would be bending test because bending is a common mode of deformation in the car safety structures during collisions such as front bumper in the ODB (Offset deformable barrier) or the other frontal crash tests and A/B-pillar assemblies during side crash. Further the Steel-FRP composites behave differently from bending to compression to tensile loads [41]. In [16], the bending and collapse behavior of thin walled structures is illustrated and shown in the Figure 2.23. This bending action is composed of two deformation modes such as the flexural deformation of the top and bottom sheets and the other is the compressive deformation of the side walls of the structure. Hence, it is of entirely important to understand the deformation behavior so as to strengthen the hybrid steel-FRP composites. There were few exemplary instances from the previous researches. Some of them are explained in detail in the following clause. One of that is where the hybrid specimens made out of Steel and CFRP was characterized by four-point- bending test and FE simulation is also performed for the same in [64].

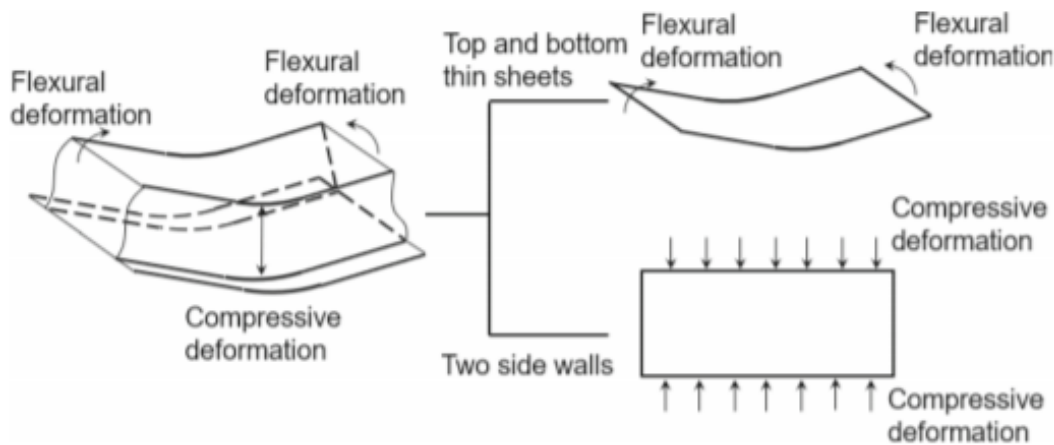


Figure 2.23: Bending collapse behavior of thin-walled structures [16]

Another illustrative example in [10, 17] emphasizes a complex hybrid hat profile under 3-point-bending load exhibited in Figure 2.24. The hybrid hat profile reinforced with composite layup of  $[0, \pm 45, \pm 45]$  along with additional glue film was resistant spot welded onto a metallic closing plate in order to increase the stiffness. The energy absorption of the structures was calculated until a displacement of 30 mm. Further, in [10] the hybrid hat profile was tested at different operating temperatures such as  $-40^\circ\text{C}$ ,  $23^\circ\text{C}$ ,  $80^\circ\text{C}$  since the operating temperature of a car is defined between  $-40^\circ\text{C}$  and  $80^\circ\text{C}$ . It was found that the performance of additionally glued profiles drops down to the level of profiles manufactured without additional glue film at elevated test

temperature of 80° C. Also the influence of testing speed on the hybrid hat profiles with additional glue film by use of a drop tower test was performed. The impactor scaled 58 kg and the drop height was 2 m and the impactor velocity achieved was 6.3 m/s. The deformation and intrusion were measured and compared with quasi-static tests and the dissipated energies were calculated until a displacement of 30 mm. In [17], the reinforced hat profiles were tested using 3-point-bending so as to study the influence of moulding pressure and pressing time of reinforcement.

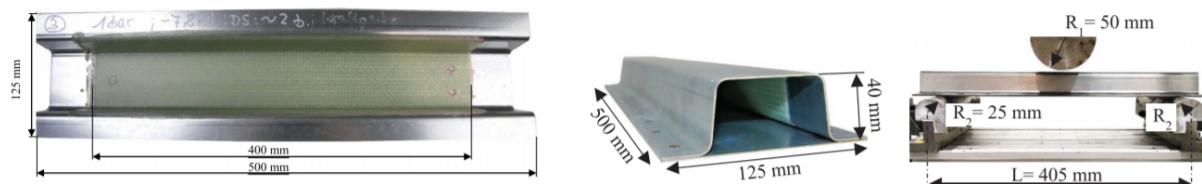


Figure 2.24: Hybrid hat profile with spot-welded closing plate [10, 17]

Lauter et al. [18] used two different sample geometries for testing the performance. The tests were performed on a carriage crash test facility displayed in Figure 2.25.

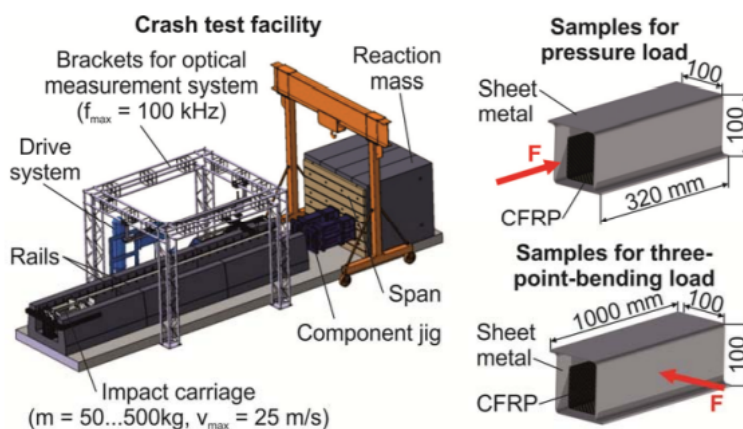


Figure 2.25: Crash test facility and Sample geometries [18]

Different component jigs were used to represent contrasting load cases such as bending or pressure loads. The carriage was accelerated by hydraulic drive system on guided rails. The pressure load case was performed with 320 mm and three-point-bending load case with 1000 mm long double-Z-profile. The metal adherend was DD11 with thickness of 1.5 and 2 mm and the FRP adherend was carbon fibers embedded in epoxy resin (Type E201) from SGL. The reinforcement CFRP of length 300 mm was pressed onto the sheet metal by prepreg-pressing process. The consolidation pressure used for the pressing process exceeded 0.3 MPa. The metal adherends were bonded together in the flange region with the help of BETAMATE 1620 adhesive of thickness 0.3 mm. The deformations and the intrusions were measured with the help of optical measurement system. Also the tests were performed

with different wall thicknesses for the metal and the reinforcement and the medial specific forces for each configuration was compared. It was found that the reinforcement for lower wall thicknesses shows noticeable improvements within the hybrid structures because of the relative share of CFRP. Lee et al. [65] fabricated the hybrid composites made of cold rolled steel (CR340) of thickness 0.9 mm and CFRP with thermosetting epoxy resin from Toray of thickness 1.1 mm. Further the three point bending tests were carried out and the FE simulation to compare the results. Similar to this, in [66] only the experimental three-point-bending test was carried out to analyze the performance of the hybrid material namely carbon fiber-reinforced plastic infiltrated with epoxy resin from MITSUBISHI and X5CrNi18-9 stainless steel manufactured by hot-press molding. The flexural strength of the metal-frp structure was studied by varying molding pressure, temperature and holding time. Also in [41], the three-point-bending tests were carried out experimentally and an analytical model was developed to investigate the flexural behavior of composites such as DP980 Steel and CFRP and also DP980 and AFRP (Aramid fiber reinforced polymer) and the results were compared to the analytical model and found a good correlation.

The different mechanical tests executed for characterizing and testing the performance of the hybrid composites was discussed in this section and in the subsequent sections the simulation techniques which were used for the fusion bonding process and the mechanical test simulations in the previous investigations will be deliberated.

## 2.3 Simulation techniques

The simulation methods adapted to illustrate the fusion bonding process in the literature study is very much limited. But the structural simulations performed to evaluate the strength of the hybrid components is notably high when compared to the process simulations. Hence, an eminent simulation method which describes this particular process is expressed in the following section.

### 2.3.1 Process

In Levent et al. [11], the simulation is carried out in FEM software ABAQUS<sup>TM</sup> using the fully coupled thermal-stress analysis with explicit time integration. The aim of the investigation was to simulate the maximum outflow or displacement of the plastic which melted due to heat conduction from the metal upon applying the joining force. The experimental procedure was demonstrated in section 2.2.2. This particular research did not include any kind of bonding agent in the joining area of the metal and plastic components. ABAQUS<sup>TM</sup> provides a method called as the coupled Eulerian-Lagrangian (CEL) [67]. The metal does not undergo large deformations and hence

it was meshed with Lagrangian elements. But when the plastic meshed with Lagrangian elements reaches its melting point, it begins to flow and when it is pressed by the metallic joining partner the elements will undergo large distortions and the simulation may become unstable. Therefore, to avoid the discrepancy the plastic is meshed with Eulerian elements since in Eulerian analysis, the mesh is fixed in space and the material can flow through the mesh which can avoid the element distortions. ABAQUS™ provides the possibility of combining the Eulerian with the Lagrangian analysis. The technique is applicable in areas which involves fluid-structure interactions. The joining process including heating and holding takes place for around 290 seconds in the experiment and this entire time cannot be solved using the explicit time integration technique. Hence, two different approaches such as the mass scaling and time scaling were applied to reduce the simulation time. The boundary and loading conditions prescribed on the FE model is illustrated in the Figure 2.26.

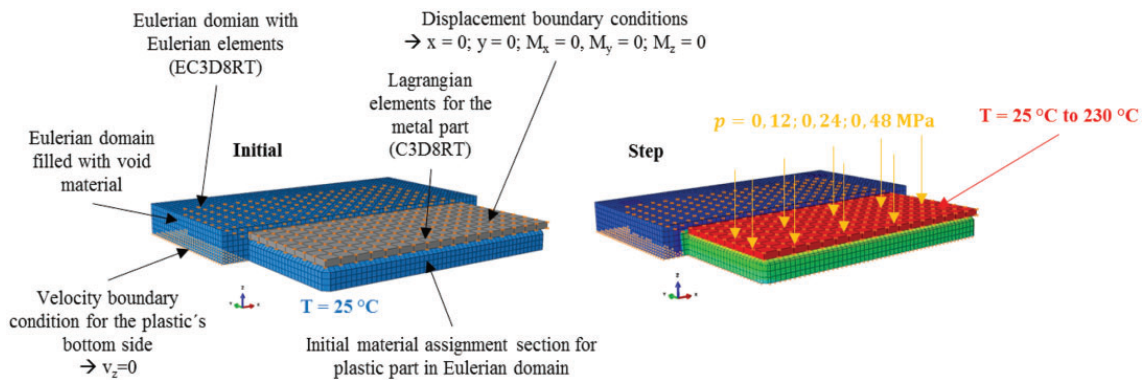


Figure 2.26: Boundary conditions on the process simulation FE model [11]

An initial condition of about 25 °C is applied to the nodes of the metal and plastic part. The Lagrangian elements C3D8RT is used for the metal partner and Eulerian elements EC3D8RT for the plastic joining partner. The temperature boundary condition applied to the metal obtained from the validation experiment. Also the different joining forces applied on the Steel is applied as a constant pressure with magnitude of (0.12, 0.24, 0.48 MPa). To obtain the heat transfer coefficients dependent upon the pressure, a separate simulation method of fully coupled thermal-stress analysis with implicit time integration in ABAQUS™/Standard is carried out to use it for the process simulation. The material parameters such as Density, thermal conductivity, viscosity of the plastic part, specific heat capacity, heat transfer coefficients obtained from the validated simulation and the dilatational wave speed through the element were scaled according to the scaling approaches and all the properties are temperature-dependent. The temperatures measured at the fusion zone and the bottom side of the plastic from the experiment correlated with the temperatures obtained from the simulation. The resulting outflow or displacement of the plastic as a result of the joining pressure applied on the metal was also compared with the experiment and found a close affiliation to the experimental values exhibited in Figure 2.27. The left hand

side on the picture shows the material behavior when applying the same amount of pressure with two different temperature boundary conditions. Since the melting temperature of the polyamide 6 is 220 °C, applying a temperature boundary condition of 25 to 230 °C results in the squeezing effect of plastic which is not observed in the other case. Also the energies of the bodies were analysed in the simulation to ensure the meaningfulness of the method.

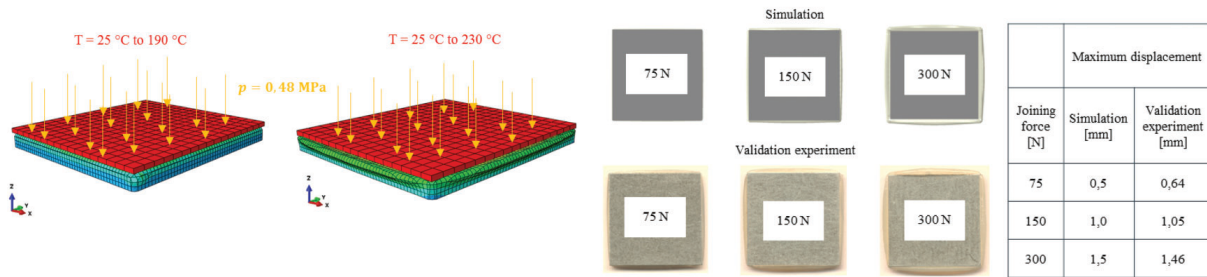


Figure 2.27: Material behavior, simulation and experimental results comparison [11]

In the next section, the structural test simulations performed to characterize the material behavior and performance using finite element method is discussed in detail.

### 2.3.2 Mechanical tests

Dhaliwal et al. [19, 20] investigated the flexural strength according to ASTM (American society for testing and materials) D790 standard of FML's (Fiber metal laminates) which constituted Aluminium alloy 5052-H32 sheets of 0.5 mm thickness and carbon fiber epoxy prepgs of thickness 0.22 mm. The specimens were manufactured by hand layup method followed by autoclave process to cure. The three-point-bending simulation is done in the FE software LS-DYNA™ using explicit time integration scheme. The model setup is depicted in Figure 2.28.

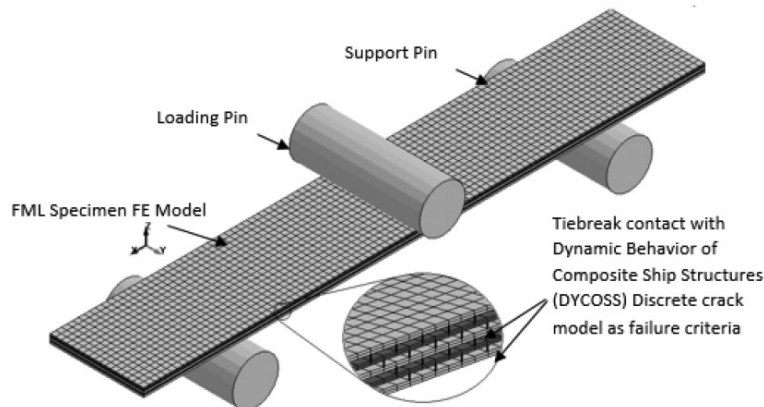


Figure 2.28: 3-point-bending FE model [19]

The aluminium and CFRP layers were modelled with 3D hexahedral elements and

avoided 2D elements which produces inaccurate results. Tiebreak interface contacts was used to model the boundary layer where the Aluminium and CFRP is in contact. This was used to simulate the interlaminar delamination between the adjacent layers. The contact between the support rods and specimen, loading pin and specimen was surface-to-surface contact and the coefficient of friction used was 1.0 . Similar to this in [20], an aluminium-CFRP hybrid hat profile was used to test experimentally and the relevant FE simulation was done in LS-DYNA software. The model setup is shown in Figure 2.29.

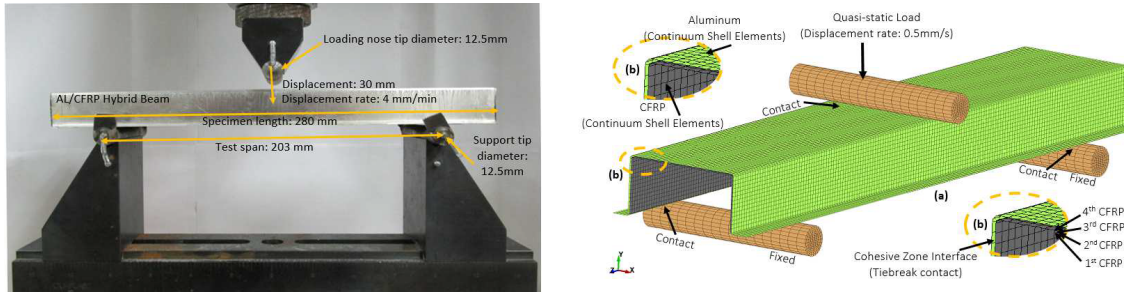


Figure 2.29: Experimental and simulation setup of 3-point-bending model [20]

Kai et al. [21] developed a 3D constitutive model for the FML's which constitutes glass fiber reinforced aluminium laminates (GLARE). The fiber delamination, ductile damage of the metal adherend and interlaminar debonding was analysed by employing a user subroutine VUMAT in ABAQUS<sup>TM</sup>/Explicit 6.12. Cohesive element functionality was employed to capture the debonding behavior between metal and FRP. Tensile test according to (ASTM D3039) and three-point-bending tests according to (ASTM D7264) were carried out experimentally and also evaluated numerically. The FE model developed is represented in Figure 2.30.

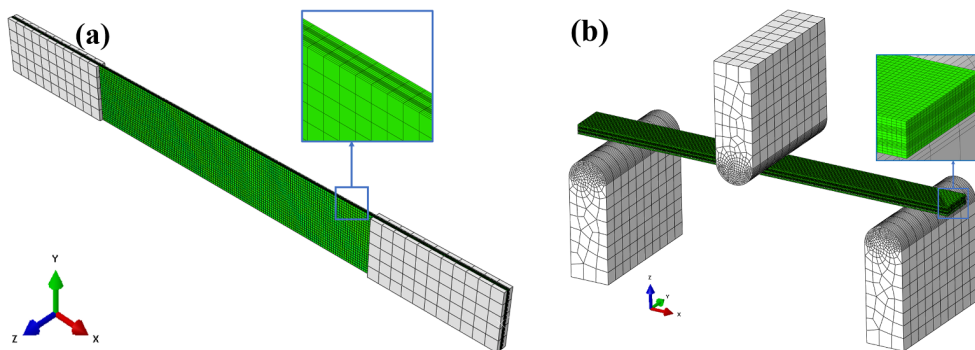


Figure 2.30: Tensile and 3-point-bend FE model [21]

Similar to this, Ruohang Xu et al. [68] developed a user-defined FORTRAN subroutine in ABAQUS<sup>TM</sup> to represent the damage criterion of CFRP. The bending behavior of carbon fiber reinforced aluminium laminates (CARALL) was investigated experimentally and numerically using three-point-bending tests and a cohesive zone model

(CZM) was used to simulate the interlaminar failure of the hybrid composite. The specimens were manufactured by heat pressure composite process. Based upon the results from the bending tests, it was found that the aluminium yields in the mid-span region and delamination occurred between the aluminium and CFRP layers. The deformation of the multi-cell Al/CFRP (Aluminium carbon fiber reinforced plastic) hybrid tubes was investigated by quasi-static bending and impact tests by the drop hammer test machine in [22]. The bending resistance and the energy absorption performances were investigated in ABAQUS<sup>TM</sup>/Explicit. The aluminium and CFRP layers are modelled as shell elements (S4R) and the cohesive elements (COH3D8) was used for the demolding film or adhesive which was used for joining metal and CFRP. The deformed shape and the Von Mises stress distribution was analysed and parametric studies were carried out to evaluate the wall thickness, no.of CFRP plies, impact velocity. It was also found that the hybrid multi-cell tubes outperforms the single cell Aluminium or CFRP counterparts in the crash performance by showing an increase in the specific energy absorption. The multi-cell hybrid tubes and the simulation result (tensile damage status) of the CA4 (4-celled hybrid tube) in the quasi-static bending test in Figure 2.31.

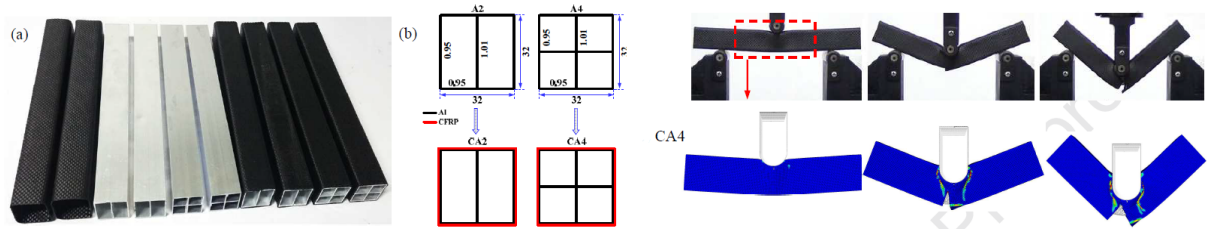


Figure 2.31: Geometry (dimensions in mm), simulation results of the hybrid tubes under quasi-static bending [22]

In [65], Lee et al. performed experimentally the tensile and three-point bending tests. The damage initiation criteria and the damage evolution for CR340 steel was realized in the simulation using the forming limit curve obtained from the forming limit diagram experiment. And for the CFRP, the damage initiation and damage evolution was predicted by the Hashin's theory inbuilt in ABAQUS<sup>TM</sup>/Explicit. Cohesive contact in the interaction property was used for the boundary layer instead of the cohesive elements and the \*TIE condition was used for contact condition between CR340 and CFRP in the case of three-point-bending simulation. Apart from the bending tests, there were also some investigations which tested the axial-loaded composite structures. One such study in [23], where the circular hybrid aluminium-CFRP tubes were examined experimentally and numerically. The metal adherend was EN AW 6060 T6 served as the core for the hybrid sample in which the CFRP layers are wound around it. The hybrid tubes constitutes a metal thickness of 1 mm and CFRP thickness of 1.7 mm. The hybrid tubes were cured at 120 °C for one hour and also the tubes were subjected to heat treatment at 180 °C for 30 minutes as in [10] to realize

the e-coat drying process. The experimental process was carried out and found that the specific energy absorption increased by about 37% to the pure aluminium sample tested by the drop tower. The experimental and numerical simulation setup is displayed in Figure 2.32.

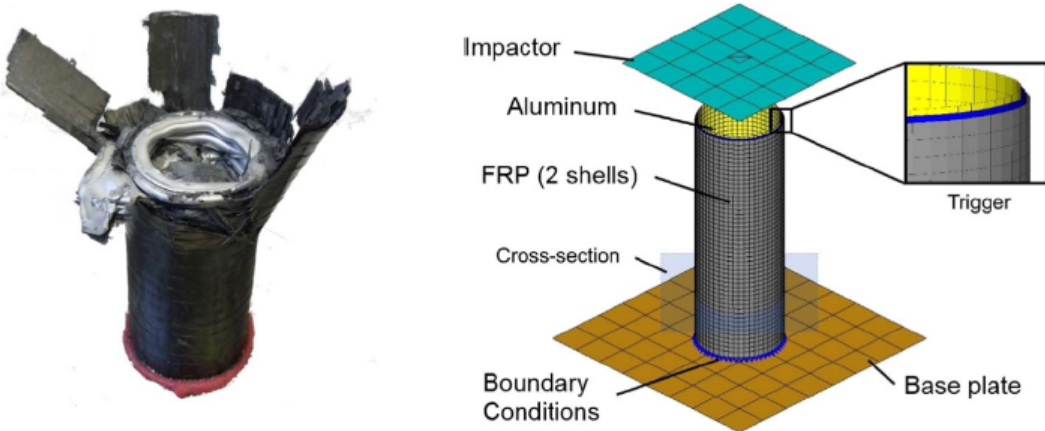


Figure 2.32: Experimental and numerical simulation setup of hybrid component [23]

The numerical simulation is carried out in FE code LS-DYNA. The CFRP component has an orthotropic material model with failure criterion provided by Chang-Chang. The aluminium and FRP-component were modelled by rectangular shell elements. The contact between them was realized by tiebreak options as in [19] and thus delamination between the shell elements could be taken into account. The contact between the impactor and tube was realized by the single surface contact algorithm provided by LS-DYNA. The bottom of the tube was fixed by displacement boundary conditions and the impactor was modelled with rigid elements. The force-displacement curves were generated and compared with the experimental trials and found that the peak forces and intrusions were calculated with high accuracy.

## 2.4 Review of process parameters

There are many aspects which are concerned about the manufacturing of hybrid connections. For instance, the surface pretreatment of the joining partners, storage stability of the fiber reinforced polymer material, joining temperature at the interface and the pressure applied to consolidate the joint. Even some of the unconcerned features such as the holding time, cooling rate and overlap area plays a significant role in determining the strength of the joint. The first apprehension is about deciding which of the process parameters that can be complied with the present investigation. Even though it is a slight combination of adhesive and fusion bonding techniques, the metal partner will not be heated since the bonding agent along with steel must be laid upon the heated FRP material. Hence, unlike the heating up of metallic partner

in fusion bonding technique (in this work it is not done), the joining temperature at the interface is one of the important aspects of this process. There are also some other parameters that were reviewed in the previous researches which are explained shortly and the things which are adapted in the present work are elucidated.

### **Surface pretreatment and storage stability of FRP material**

Lippky et al.[14] focussed on the laser pretreatment of the metal surface before joining with low and high intensities. The high intensity surface treatment leads to increase in surface roughness which provides better interlocking between the joining partners. In [69], different surface treatments of the metal partner such as acetone AT and corundum blasting were compared. Of this, the corundum blasting with additional polymer layer increased the polymer layer in the joining zone which further increased the joint strength. Haberstroh et al.[8] concentrated on the sandblasting of the metal partner which enhanced the mechanical adhesion. Robert et al.[10] investigated the storage of FRP material which also plays an important role in draping the composite onto the metal part. If the material is stored at high temperatures for a long period of time, it increases the physical ageing and viscosity of the material. In the present investigation, the joining partners were only pretreated with isopropyl alcohol for all the process related experiments as deliberated in section 4.2.

### **Joining temperature and Joining pressure**

The importance of heating up the metal partner is shown in [13]. Though the FRP adherend is heated above its melting temperature, while joining the two adherends if the temperature of the metal adherend is low it subsequently cools the molten plastic at the joining zone which in turn leads to improper wetting of the polymer over the metal surface. This decreases the bonding strength and hence with constant temperature (over melting point of FRP) and increasing metal temperatures the bond strength can be increased. Usually the temperature of the metal partner in the range between 235°C and 275°C and the FRP adherend in the range between 220°C and 280°C is sufficient to achieve higher strengths. As aforementioned previously, since the addition of the adhesive film in the interface, the heating of metal partner is not considered. From the previous studies [8, 66, 60, 13, 14], it is seen that the joining pressure applied should be in the range of 0.1 to 1 MPa. If it exceeds this pressure it leads to pressing out of either the adhesive or the polymer material from the joining zone which further leads to poor wetting of metal surface. In [8], an optimised pressure profile is illustrated to prevent this effect and also to counteract the thermal contraction of the thermoplastic during the cooling phase. Usually lower joining pressure with well prepared surface treatments of the joining partners is considered

a good technique to increase the strength. In the present investigation, it is considered to maintain the applied pressure within the permissible limit so as to avoid the outflow of the adhesive or thermoplastic from FRP material.

### Holding time and cooling rate

The emphasis of these two process parameters is very less. Even then the purpose of the longer holding time in the pure fusion bonding technique with low pressure and lower joining temperatures leads to a high lap shear strength as evaluated by experiments in [13]. The cooling rate importance is shown in [69], where a faster cooling rate leads to many quickly grown crystals at the interface and drives to achieve slightly higher tensile shear strength compared to slower cooling rate. In the present investigation, the holding time is the curing time of the bonding agent which occurs for 5 minutes and the free convective cooling is considered.

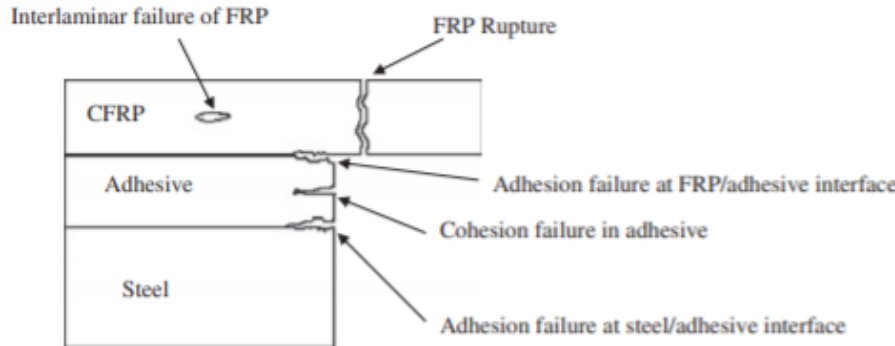
### Mechanical tests

Dhaliwal et al.[19] showed that the bending strength of the FML can be increased compared to the individual metal bending strength which is of same thickness. In [20], results demonstrated that keeping the metal volume fraction to a accepted value and increasing the volume fraction of the FRP tends to increase the bonding strength. Haberstroh et al.[8] showed the difference between the adhesive and fusion bonding techniques which serves the basis of combining both in this research. The results demonstrated that instead of increasing the overlap length in the lap shear specimens, the overlap width should be increased since for the large overlap lengths the stress distribution is inhomogenous. This is also proved by Kaempf et al.[13] where the overlap length is decreased with maintaining the overlap width as constant. In the present work, the mechanical test such as 3-point-bending tests according to the standard DIN EN ISO 14125 are carried out.

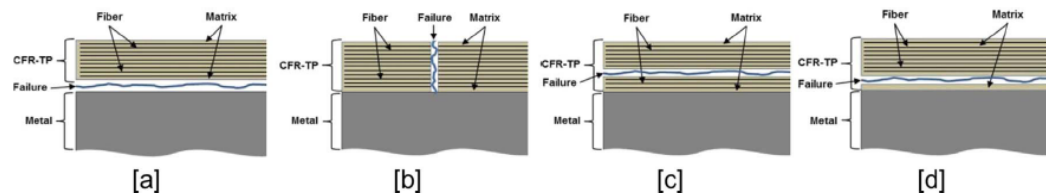
### Failure modes

The failure modes of the hybrid joints is investigated in [15, 20, 45]. The possible failure modes when connected with adhesive in 2.33a and pure fusion bonding technique (without adhesive) in 2.33b are shown. The interfacial failure can occur in two ways. One is at the interface of FRP and adhesive and other one occurs at the interface of steel and adhesive. There can also be the interlaminar failure which occurs at within the FRP in two ways. This can also be explained as the breakage of fibers and the matrix failure occurs in the matrix or the fiber-matrix interface. Usually the adhesive failure occurs depending on the bond capability of the adhesive and the surface treatment of the partners. In [10], based on the testing temperature the failure mode shifts from adhesive failure between steel and bonding agent at low temperatures to

a completely cohesive failure at glass transition temperature of the glue film. The failure modes were also investigated based on the testing speed and the material ageing of the FRP material.



(a) Failure mode of hybrid joints bonded with adhesive[45]



Evaluation of fracture patterns (interfacial failure [a], cohesion failure-tape breakage [b], cohesion failure-matrix breakage [c], substrate close cohesion failure [d]).

(b) Failure mode of hybrid joints manufactured by fusion bonding[15]

Figure 2.33: Failure modes

Thus the background about the technique, the process parameters which have to be adapted for the present work and the previous researches related to this investigation are elaborated in detail. In the next chapter, the methodology accustomed for this work is briefly conferred.

# 3 Objective and methodical approach

In this Chapter, the purpose of the research work and the direction in which the process is going to be explored is elaborated. In the following section a concise demonstration about the objectives of this work is provided. Then, the approach or the methodology to accomplish the objective is deliberated.

## 3.1 Questions in focus and research objectives

From the conclusions of the state-of-the-art researches, the preeminent question is how the industrial manufacturing process in [10] can be studied so as to improve the process and reduce the cycle time in the automotive industries. This question can be answered when the following sub-questions are focussed.

1. What will be the strategy to replicate the process with the available equipment in the laboratory?
2. What are the influence of process parameters and which one of them are taken into consideration?
3. What will be the optimal modelling procedure to simulate the process and how it can help with components in car model?
4. Which stage of the bonding process will be concentrated in detail?
5. How the devised process procedure will be validated?
6. What kind of mechanical tests are to be performed to analyze the strength of the hybrid samples?

When all these questions are resolved, the preeminent question can be answered. In view of these questions, the objectives of this work are formulated as follows:

1. To build up the material model for both the process and structural tests and validate it before using in the simulation.
2. To simulate the process using the ABAQUS<sup>TM</sup>/Standard FE software with temperature-dependent material properties.
3. To perform thermal and mechanical simulations for the process and verify them with the experimental results.

4. To perform the mechanical tests experimentally and verify them with the obtained simulation results by establishing a FE model.
5. To identify the critical components in a car model which are involved in crash analysis so that they can be patched.
6. To transfer the constructed simulation method to those critical components and analyse the deformations within those structures.

In the next section, the method which will be followed is elucidated briefly.

## 3.2 Definition of research workflow

The workflow of this investigation is illustrated in Figure 3.1. The two preliminary points with which the investigation could be commenced is exemplified as follows:

- The prospect of this technique combining the fusion bonding process with an additional glue film must be validated by the pre-tests.
- Ensuing that, the hybrid plates will be manufactured in the same procedure in which the pre-tests were done.

Thereafter, the analysis is done in two phases. The **phase one** can be break down into two series of events. The first set of events are concerned with only the process aspects such as deciding which stage of the process to concentrate, building up the required material model which could be used for realizing the numerical representation and finally a validation experiment and simulation. The second series of events are concerned with the mechanical tests to characterize the performance and strength of the hybrid samples manufactured from the process. The aforementioned series of events are explained in a nutshell in the following points.

- **First series of events:** The process will be simulated using a definitive modelling strategy called as Sequentially coupled thermal-stress analysis (explained in section 3.3.3) in ABAQUS™/Standard. Before applying the strategy, the decision was made to simulate the cooling stage of the process. This is done mainly because in the cooling stage the adhesive will be fully cured at this point and the relative displacements will start to decrease. So, in most cases it is sufficient to consider only the cooling phase [24]. Hence the temperature and deflections measurements are done in the hybrid plate after it has undergone the heating, pressing and holding phase. So, the material property which is required for the convective cooling of all the members of the hybrid plate has to be carried out separately and validated. After that it will be used in the final cooling stage of the process simulation. Further, to validate the process a validation experiment is done and verified numerically so as to ensure the exactness.

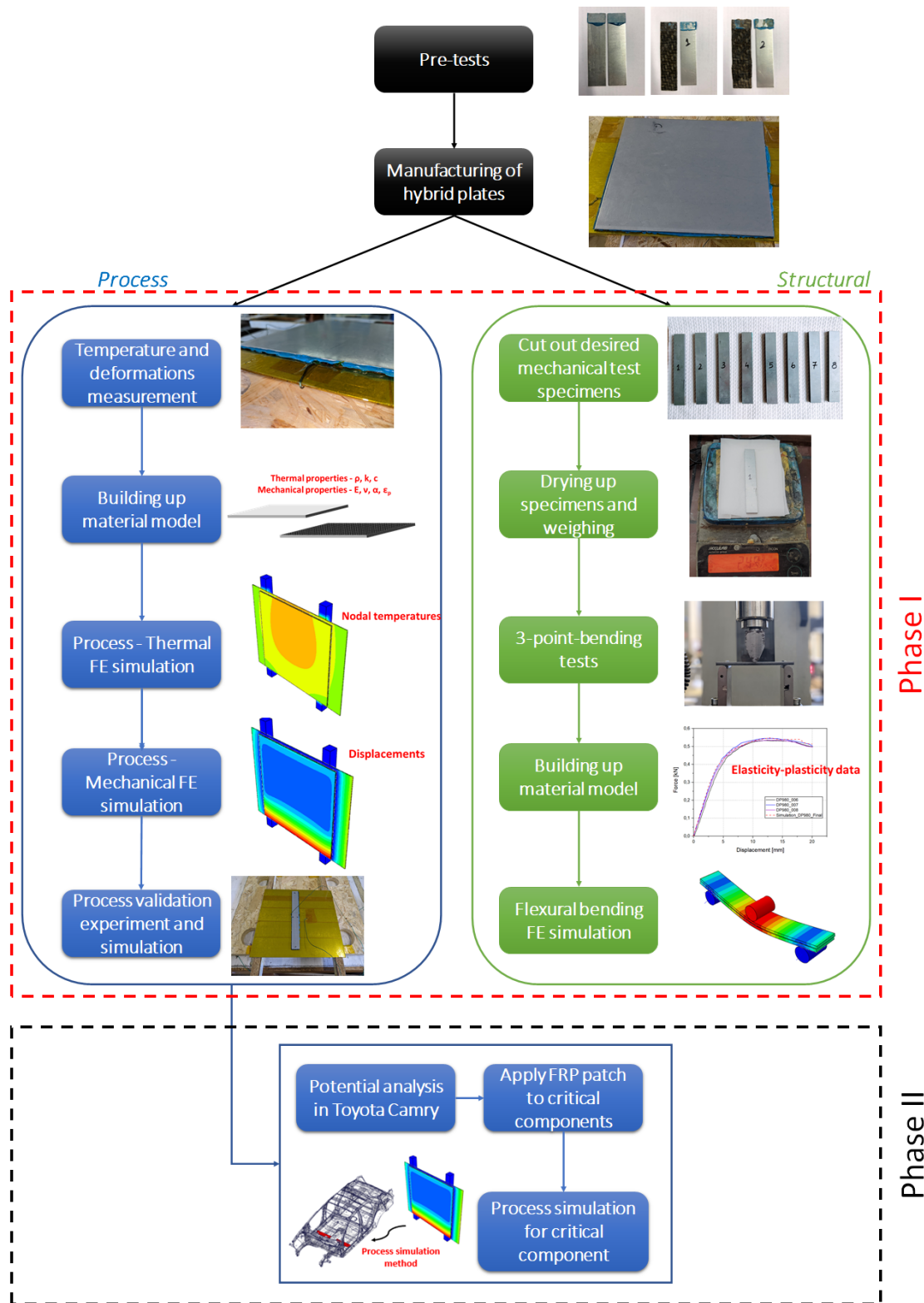


Figure 3.1: Research workflow

- **Second series of events:** Also, within the first phase, the samples which are required for the flexural tests will be cut out using the water jet cutting machine available at OHLF (Open hybrid lab factory). Then they will be subjected to

the experimental tests and further validated by using a 3-point-bending FE simulation model. The material properties which are required for the structural simulation will be validated individually before applying it for the hybrid specimen bending simulation model.

In the **second phase**, the potential analysis is carried out in the Toyota Camry model available at GNS mbH. The components are evaluated on some investigation criteria such as plasticity change, intrusions within the BIW structure and failures with the elements such as material, adhesive and spotwelds based upon different crash analysis. The critical parts will be identified and then patched to see if the weight of the car can be reduced or not which is the final goal after manufacturing the hybrid component in the industry. So, for those critical parts the constructed process simulation method will be transferred to analyze the deflections.

### 3.3 Methodology

The main concern is to know about the damage within the adhesive material and also deflections of the multi-material partners. Since the BIW is heated upto 200°C, due to the different thermal expansion coefficients of the materials, the adhesive will be exposed to mechanical loads during the paint drying process. This might lead to the residual stresses or even damage within the adhesive layer [70]. The important phase shown in figure 3.2 is the cooling phase where the adhesive is already cured and surpasses the glass transition state and the displacements just start to decrease at this point[24, 71] as previously mentioned in section 3.2. The resulting displacements are due to the different thermal expansion coefficients of the joining partners such as Steel, FRP and Aluminium [1]. Hence, it should be identified as early as possible to eliminate the adverse effects on the adhesive during the use phase.

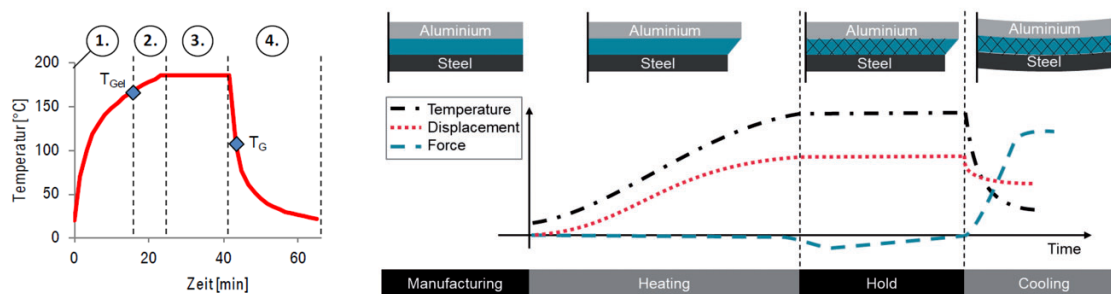


Figure 3.2: Importance of simulating cooling phase [1, 24]

In the subsequent sections, the components involved in the joining process, the mathematical relation of heat transfer and its implementation in FE software and simulation strategy of cooling process are deliberated.

### 3.3.1 Components in experimental process

To simulate the cooling process, the independent components of the experimental process must be subjected to separate cooling experiments so as to use the material data in the final simulation. The different members of the experimental joining process are displayed in the figure 3.3.

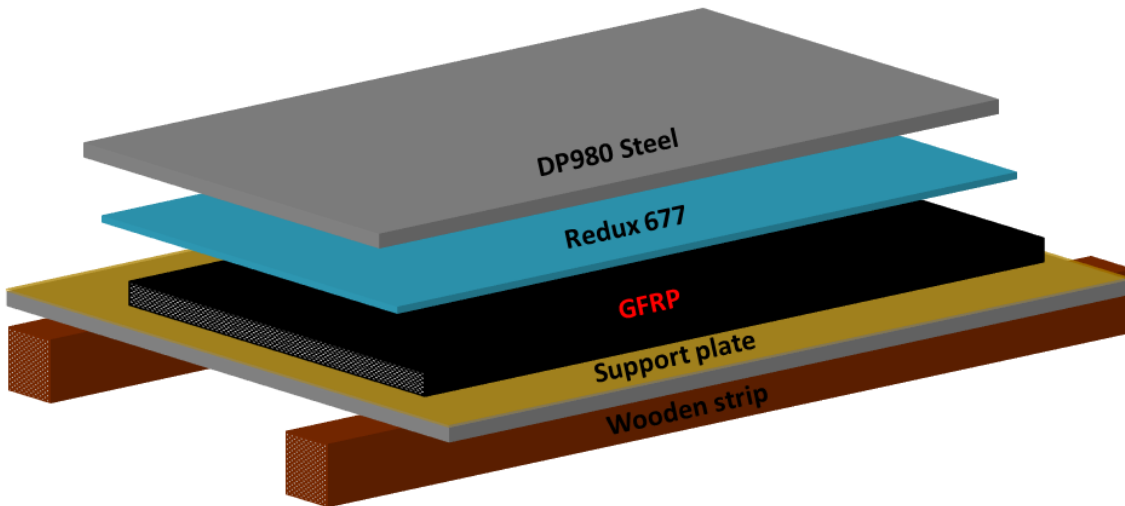


Figure 3.3: Key elements of the experimental process

Foremost, the joining partners Steel, GFRP, Support plate wounded with Kapton tape must be considered for the separate cooling experiments. Then, the temperatures results from the experiment will be validated using the FE software to ensure the correctness before using it in the final simulation. The different kinds of heat transfer which are involved and has to be modelled are listed below

1. Free convective heat transfer by dissipating the heat to the ambient plays an important role and its implementation is explained in the section 3.3.2
2. Conductive heat transfer between the Steel, adhesive, GFRP, Support plate and wood is realized by means of \*TIE functionality already available in the software.
3. Radiative heat transfer is not considered in any of the previous process simulation concerned researches and this is dominant in regions which involves temperatures above 2000 ° C [72] and this will not be included in the current work.

### 3.3.2 Cooling process implementation in ABAQUS™

The important heat transfer mechanism in this process is the convective cooling and the basic relationship is represented in the following equation.

$$\dot{Q} = -hA(T - T_s) [73]$$

where,  $\dot{Q}$  - Rate of heat transfer per unit time

$h$  - Heat transfer coefficient

$A$  - Area of the object

$T$  - Surface temperature of object

$T_s$  - Ambient or sink temperature

Mathematically, the rate at which the heat dissipates from an object to the surrounding is calculated using this equation. To implement this relation in ABAQUS™, there exists an interaction property namely \*FILM condition [67] where the sink temperature and the heat transfer rate based on temperature via the film coefficients can be defined and the cooling simulation can be replicated. This must be done for the individual components in the experimental process and validate it using this simulation technique so that the overall cooling process could be evaluated. A schematic representation of applying the film condition to the individual components in the software is depicted in the figure 3.4

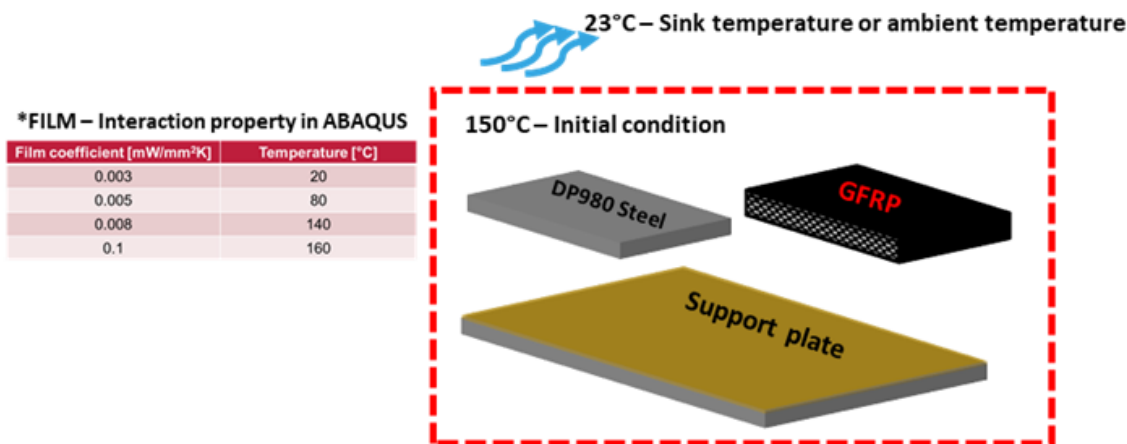


Figure 3.4: Illustration of film condition implementation in ABAQUS™

### 3.3.3 Simulation outline

#### Process

The simulation strategy adapted here is the Sequentially coupled thermal-stress analysis method in which the displacement or stress fields depend upon the temperature results. It is implemented in the software by performing an uncoupled heat transfer analysis followed by the stress/displacement analysis. It is a common example of sequential multiphysics workflow [74]. The outline of the simulation is represented in the figure 3.5. Initially, the separate cooling experiments will be conducted to know the cooling rate of the components involved in the experimental process.

Then, the thermal simulation FE model is created and the film condition is implemented so as to predict the cooling rate and compare it against the experimental values. If it has a closer match, then the film conditions for the separate components are carried forward for the process simulation and the same procedure is carried forward to calculate the temperatures. Further, the temperatures will be used as a load for the mechanical analysis and finally the resulting displacements and stress should be calculated.

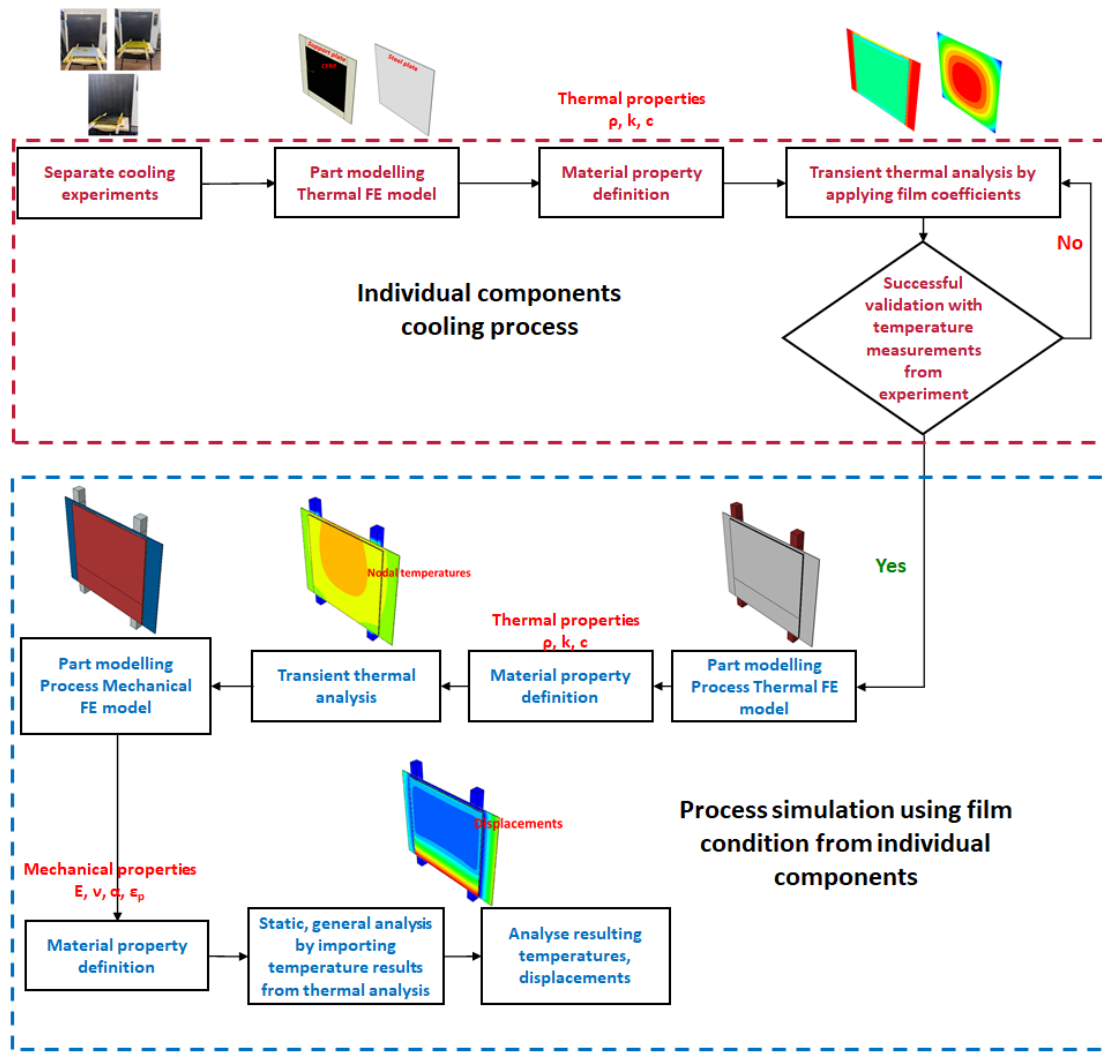


Figure 3.5: Outline of the simulation strategy for Process

## Structural

The outline which was built up for the mechanical tests simulation is shown in the figure 3.6. Initially separate flexural tests according to the standard DIN EN ISO 14125 must be performed for the Steel and GFRP materials. Then the 3-point-bending simulation for both the materials will be calculated with the elastic properties available. The plasticity data for the steel will be first evaluated using the swift-voce law and

must be used in the bending simulation. Once the simulation results of both individual simulations correlates with the individual flexural test experiments, then the material model is finalized and will be used for the hybrid specimens simulation. The hybrid specimens should be cut out from the manufactured hybrid plate using water jet cutting machine and should be dried in the oven for a certain period of time to remove the moisture content. Then the bending experiments for the hybrid specimens followed by the validation of simulation should be performed to analyze the strength of the hybrid joint.

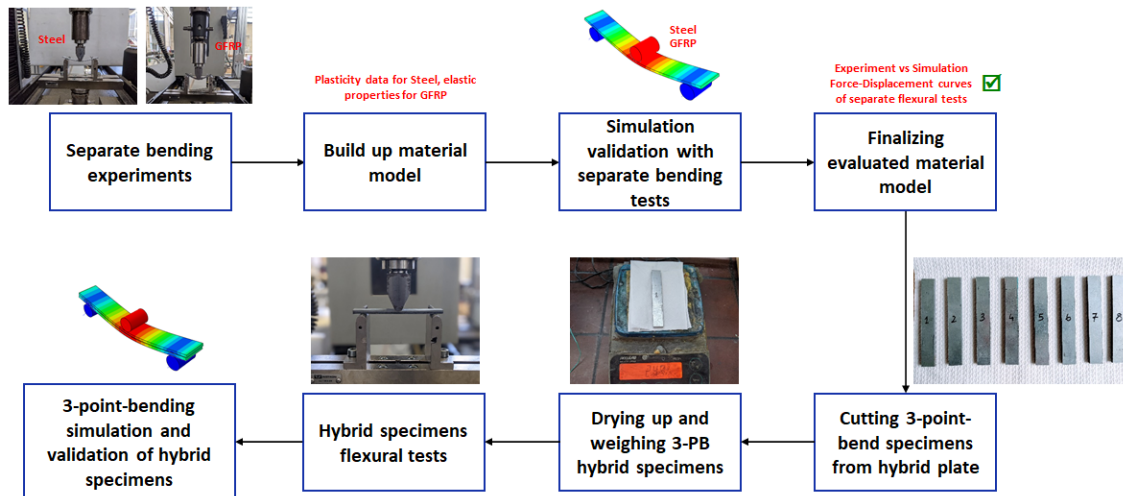


Figure 3.6: Outline of the simulation strategy for mechanical tests

Thus, the objectives and the methodical approach of this research is explained briefly. In the following chapter, the experiments which were carried out will be elaborated.

# 4 Experimental proceeding

The experiments which are conducted in relation to thermal and mechanical simulations are briefly elaborated in this chapter. Initially the equipment used, materials and the process experiments followed by the 3-point bending test are elucidated comprehensively.

## 4.1 Equipment and materials

The equipment used for the process and mechanical tests are described in the following sections. Ensuing that, the materials used for the process and mechanical characterization are explained.

### 4.1.1 Equipment used for the process and its validation

Lippky et al.[40] described the potential of heat-assisted press joining technique which involves lightweight hybrid structures based on thermoplastic systems. The heat-assisted press joining technique is also investigated in one of the researches [10] where the production of hybrid plates are performed. This serves as the motivation for adapting this technique and the equipment which is used for the experimental process is depicted in the figure 4.1



Figure 4.1: Press equipment used for the process

The first picture shown in the left side is used for the pre-test procedure. On the right side is a bench type heat-press equipment Polystat 200 T [75] from Servitec Maschinenservice GmbH which is used for the manufacturing of hybrid plates. This apparatus has heating plate size of 250 mm x 250 mm made up of Aluminium and a maximum working temperature of about 250 °C. A pressure of about 1 kN to 200 kN can be achieved based on the application. Since the maximum temperature is 250 °

C, the FRP material has to be heated in a separate oven for attaining temperatures nearly  $260^{\circ}\text{C}$  as it is very important to heat the FRP material above its melting point and carrying it to the heat press. The equipment used for heating the fiber reinforced thermoplastic material is shown in the figure 4.2. The housing is made of stainless steel sheets and has an integral heating element which attains temperature up to  $800^{\circ}\text{C}$  surrounded by a ceramic housing. After the successful completion of the experimental fusion bonding process, a validation was carried out to measure the deflections in the metal joining partner. The equipment used for measuring it is a laser radiation based linear extensometer opto NCDT 1800 from micro-optronic. It is also exhibited in the figure 4.2 on the right side.



Figure 4.2: Oven used for heating GFRP and laser based linear extensometer

#### 4.1.2 Equipment used for the mechanical test

The 3-point-bending tests were carried out for the mechanical characterization and performed on a Instron 30 universal testing machine. The equipment in the figure 4.3 shows the setup of a 3-point-bending carried out for a steel specimen.



Figure 4.3: Mechanical test using Instron 30 UTM

### 4.1.3 Materials applied

- **Metal joining partner** - The most widely applied steel sheets on the car bodies DP980 (Dual phase, 980 MPa) of thickness 1.6 mm is used.
- **FRP joining partner** - Usually CFRP is preferred over GFRP due to higher elastic modulus and in applications aiming to predict the buckling resistance. GFRP is preferred over CFRP since it is cheaper and in applications where the aim is enhancement of ductility [45]. In this work, due to the availability of GFRP, the Tepex® dynalite 102-RG600(x)/47%, a consolidated composite laminate from LANXESS AG is used. Roving glass fibers were employed as a reinforcement. The fibers used in the study are in the form of twill fabrics. The resin that is used to bind the fibers is a thermoplastic resin namely Polyamide 6. The fiber content is about 47% and the density of the laminate is 1.8 g/cm<sup>3</sup>.
- **Bonding agent** - The modified epoxy film adhesive Redux® 677 from Hexcel corporation enhances the bonding of Steel or Aluminium to composites to manufacture hybrid structures. The curing temperature is about 150 °C for about 4 minutes.

## 4.2 Process

The pre-tests were conducted to ensure that the process can be considered to join the hybrid materials. To characterize the mechanical strength of the joint it was decided to conduct the lap shear test according to the standard DIN EN 1465. Several attempts were made to examine the average strength of the samples. An Steel-Steel joint was also produced to serve as a reference against the hybrid specimens.

### 4.2.1 Pre-tests

- **Reference sample** - The steel samples were cut according to the standard with length 100 mm, width 25 mm and thickness 1.6 mm. As it is previously mentioned in section 4.1.1, the heat press was used for all the pre-test procedures. The specimens used for all the pre-test procedures were cleaned with isopropyl alcohol so as to remove any contamination. The bonding agent was cut for a certain overlap length of 12.5 mm and it was placed on the specimen. Then it is placed in the heat press and cured at 150 °C for about 4 minutes.
- **Attempt 1** - In the process of producing the hybrid specimens, first the GFRP sample was cut according to the standard specimen size. Then it was heated above its melting temperature of about 220 °C. For this heating, two different methods were tried. Since the GFRP after heating becomes flexible, a support

plate was used and the GFRP sample was placed over it. In the first method, the plate was heated to conduct the heat to the sample. In another method an Infrared (IR) emitter was used to heat up the FRP material. But the former of the above two methods was time consuming which was used only for this attempt and the latter was used for the subsequent attempts.

- **Attempts 2,3 & 4** - The GFRP was heated above its melting point by using IR emitter. The IR emitter completely burnt out the FRP material in attempt 4 and almost 90% of the resin evaporated. So in all the attempts from 2 to 4 except 4, the IR emitter was stably controlled to heat up the FRP material and bonded with the metal joining partner. Also, it was tried to maintain the temperature of the fusion zone above the melting temperature of GFRP for all the attempts. In the figure 4.4, is shown an example of the hybrid joint manufactured from the heat press-equipment.



Figure 4.4: Hybrid specimen manufactured using the adapted methodical process

### Inferences from pre-tests

After the successful manufacturing of the hybrid specimens, the specimens were tested using the Universal testing machine (UTM) Instron 150 available at IFS laboratory. The fracture patterns obtained from the lap shear tests are depicted in the figure 4.5. It was observed that cohesive failure in the Steel-Steel connection. Further to that, the pressure was bit high which pushed little bit of bonding agent along the length of the specimen. In the attempt 1, as discussed earlier the heating of the GFRP material was not in a favorable way and seemingly the pressure applied while pressing them against each other was also barely minimum. There was no fiber layer found on the steel specimen which indicates a poor bonding quality between the joining partners. In the attempts 2,3 the heat treatment and the temperature of the GFRP material was controlled in a way such that it leads to adequate bonding strength. The first layer of matrix along with the fibers are found on the steel specimen and the steel part indicates a partial adhesive failure in it.

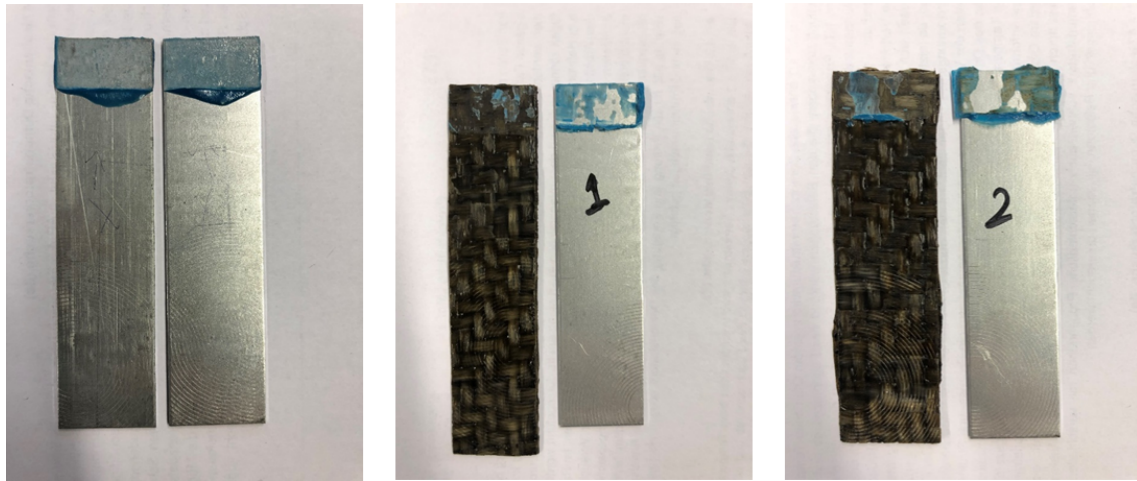


Figure 4.5: Fracture pattern from lap shear tests

The maximum amount of stress which the specimens can withstand obtained from the lap shear tests are compared against each other and found in figure 4.6. The Steel-Steel connection attained the maximum strength of about approximately 38 MPa. Except the attempt 1 in which the applied pressure was not high enough, the attempts 2 and 3 exhibited considerable strength of about 17 MPa when co-cured with additional glue film. Peter et al.[12] obtained a strength of about 14 MPa when co-cured with additional polyamide 66 sheet.

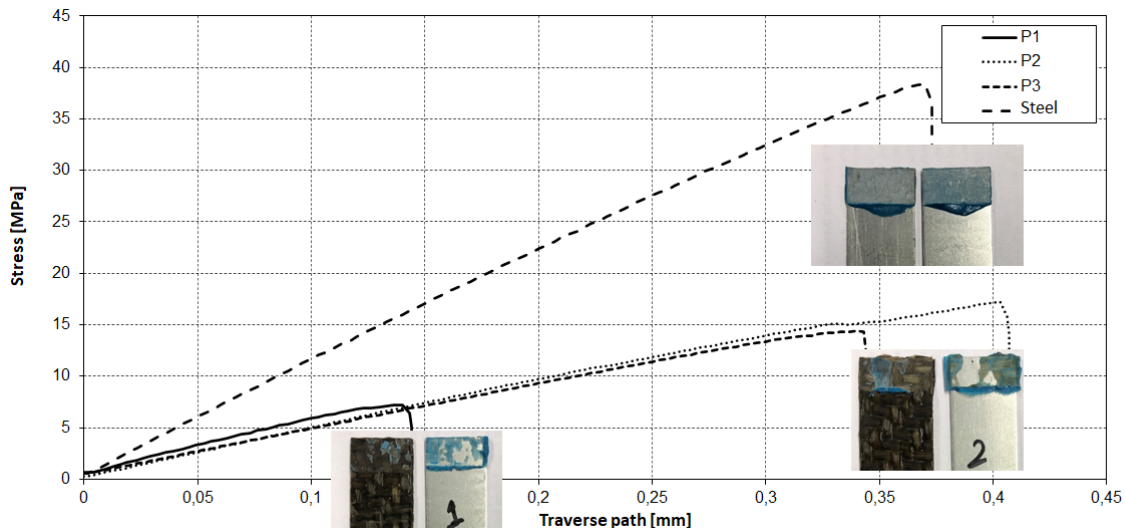


Figure 4.6: Comparison of different lap shear strengths

Kaempf et al.[13] was able to achieve 13.9 MPa when preparing the hybrid sample by induction heating. But the results in this research proves that, the lap shear strength obtained is higher than the previous fusion bonding research techniques and serves a potential to achieve even higher strengths when the joining partners' surface pre-treatment [14] is done. Although when it was compared with the [10] which forms

the base of this investigation, the process which had been adapted to produce the hybrid joints are still capable to analyse the deflections and damage which could occur within the adhesive layer. In the next subsection, the experimental process of producing the hybrid plates is discussed.

### 4.2.2 Cooling experiment for components of hybrid plate

The emphasis of cooling experiments for the individual members of the hybrid plate is already discussed in section 3.3.1. This serves as an important part of the work before proceeding into the cooling procedure of the complete hybrid plate after it is manufactured because the purpose of this subsection is to evaluate the cooling process of the components individually so that they can be validated before using it in the co-curing process simulation. The cooling experiments which were done for the Steel plate, Support plate with kapton tape and GFRP are deliberated in the following subsections.

#### Steel plate

The experiment is conducted in three attempts so as to eliminate the deviation based upon the procedure. The figure 4.7 shows a Steel plate of grade DP980 of thickness 1.63 mm, length and width of 229.5 mm. Initially the steel plate was heated in an oven at about 180°C. Then the setup is taken outside and placed on the wooden

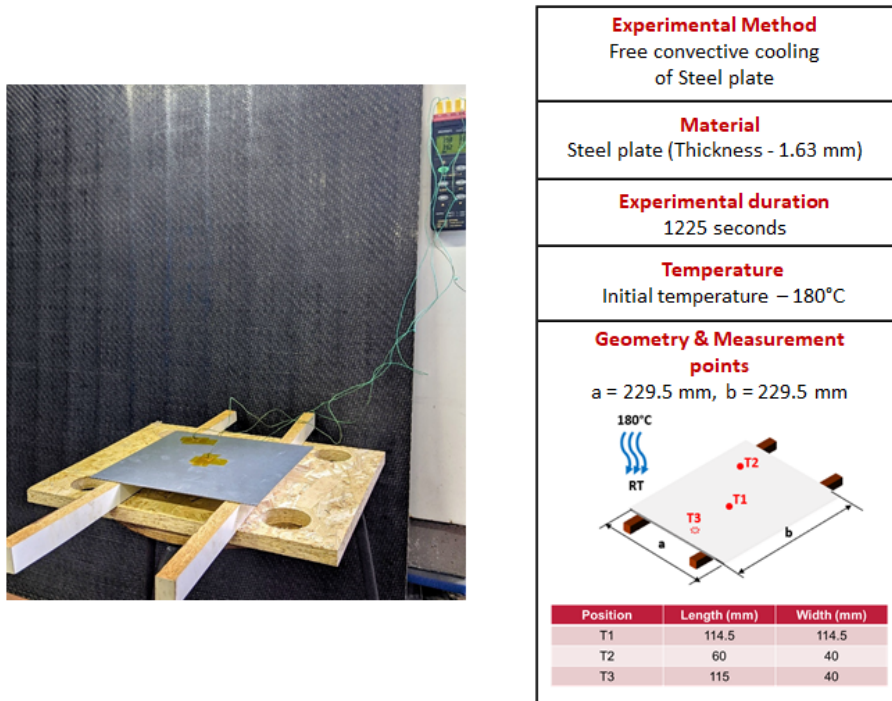


Figure 4.7: Cooling setup of DP980 Steel plate

platform to allow it cool to room temperature. The temperatures are measured at three different points using thermocouple and recorded using data logger so as to know about the temperature distribution through the whole process. In addition to this, another thermocouple was used to measure the room temperatures at which the different attempts were done. The wooden supports and the wooden platform serves as an insulation material to prevent the steel plate from coming into contact with ground surface. Figure 4.8 illustrates the cooling rate of the steel plates based upon the different trials.

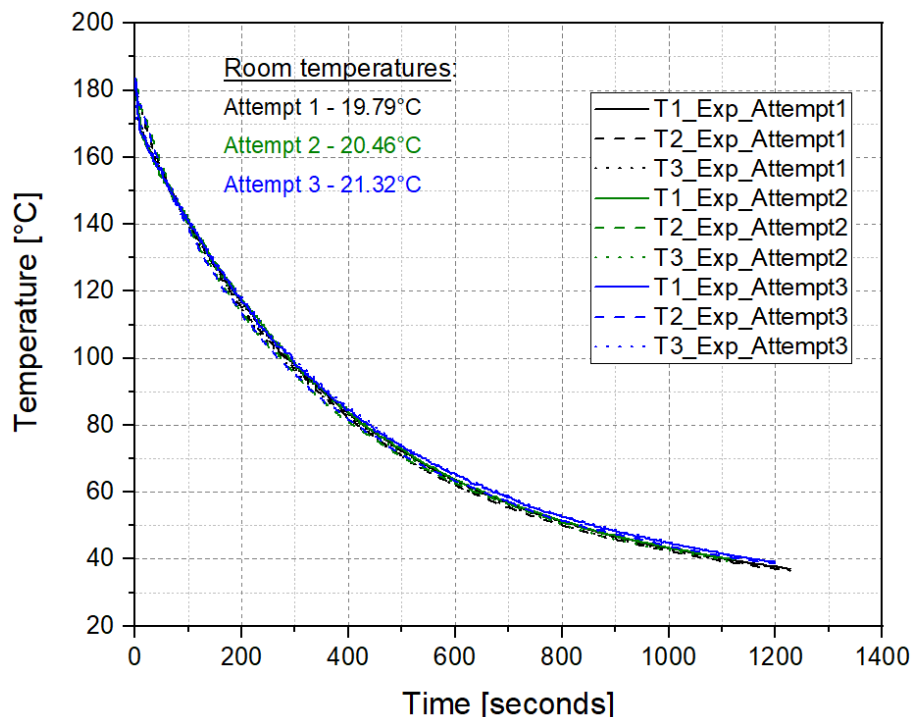


Figure 4.8: Experimental cooling trials of the DP980 Steel plate

### Support plate

The purpose of the support plate was to act as a backing structure when the GFRP material placed over it and heated above its melting point. Since the GFRP laminate bends or had the capacity of malleability above its melting temperature, the support plate was used to assist it from becoming pliable to a certain extent. Also, the AIRKAP 236 kapton tape was wounded over the steel support plate to prevent the GFRP laminate from sticking to it. Since the kapton tape was present, to make sure if the cooling behavior is the same with and without kapton tape, experiments were performed and compared. The experiment was attempted in two trials both for the support plate with and without kapton tape. The experiment was performed in the same way as described in the subsection 4.2.2 for the steel plate. The cooling setup is shown in the figure 4.9 and the experimental cooling curves for the both the support plate setups are depicted in the figure 4.10.

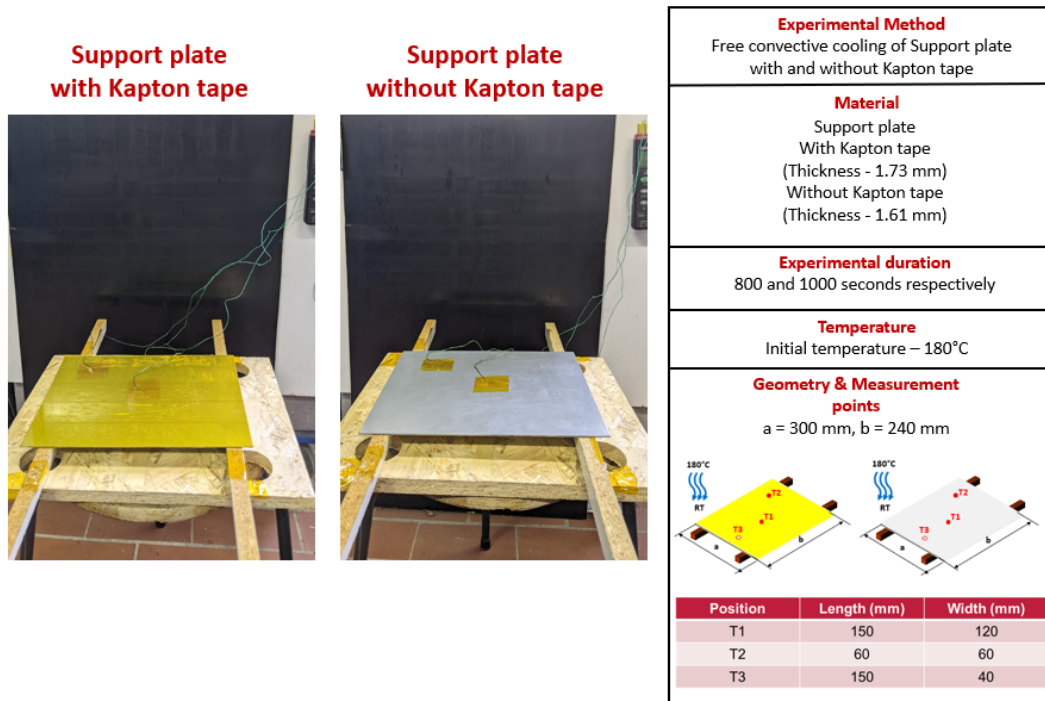


Figure 4.9: Cooling setup of the Support plate with and without Kapton tape

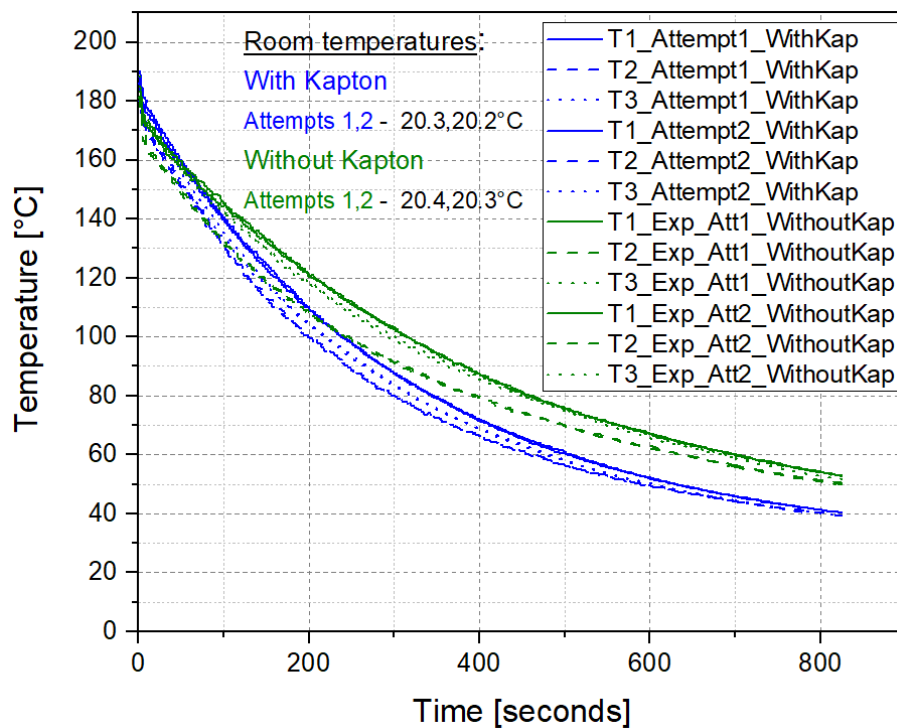


Figure 4.10: Experimental cooling trials of the support plate

It can be seen that even though the support plate made of steel, it behaved differently when the kapton tape was wounded over it. After 400 seconds, the support plate with kapton tape is 15 degrees lower than the support plate without kapton tape. This was

also due to the reason that the thermocouple was stucked to the upper surface of the tape (not in between the steel surface and kapton tape). Finally it is proved that the kapton tape plays a significant role and this should be taken into consideration while determining the temperature dependent film coefficients for the thermal FE model.

## GFRP

The same procedure was repeated to evaluate the cooling of the GFRP laminate after placing it on a support plate wounded with kapton tape. The setup is presented in the figure 4.11. This setup is bit different compared to the other two in the case where a certain amount of kapton tape was wounded over the GFRP laminate to not make it move while taking it from the oven. Also, it helps to replicate the final cooling process of the manufactured Double cantilever beam(DCB) hybrid plate(in subsection 4.2.3). The temperatures during the first attempt were above 180°C due to some complications within the experiment setup. But then, it was eradicated for the subsequent attempts. The temperatures were measured at three different points such on the GFRP surface, on the support plate and also beneath the GFRP surface which was in contact with the plate. The rate at which it cooled down is represented in figure 4.12. Initially the T3 was higher when compared with the other temperatures but towards the end of the experiment due to the heat conduction from the support plate it cools slightly faster than T1.

Thus, the individual components of hybrid plate involved in the cooling process were evaluated by separate experiments.

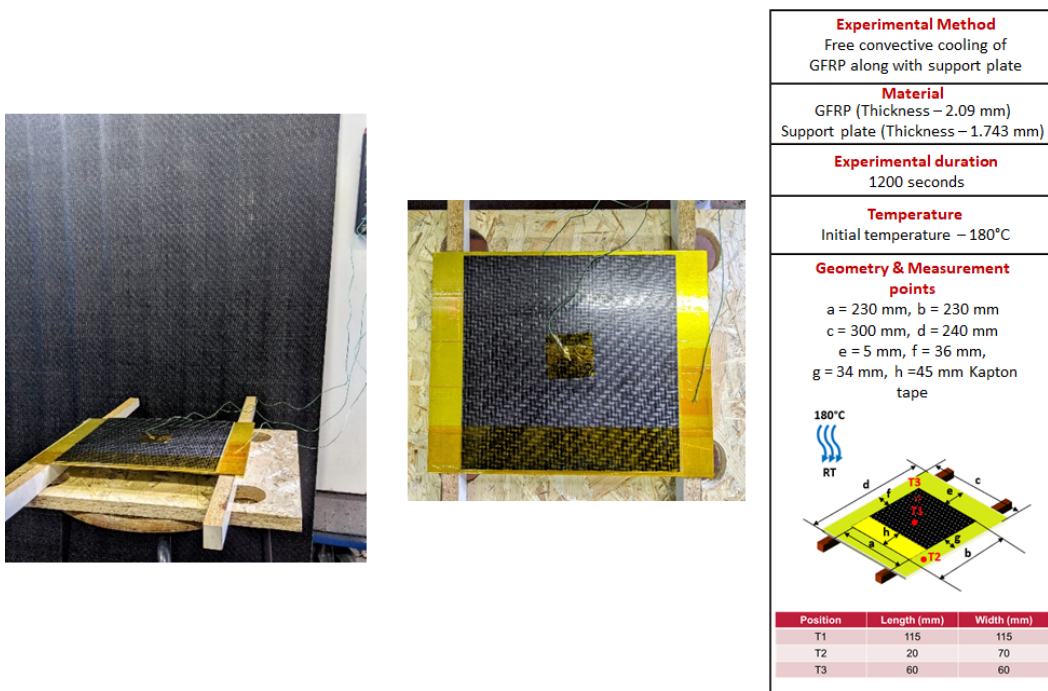


Figure 4.11: Cooling setup of the GFRP laminate

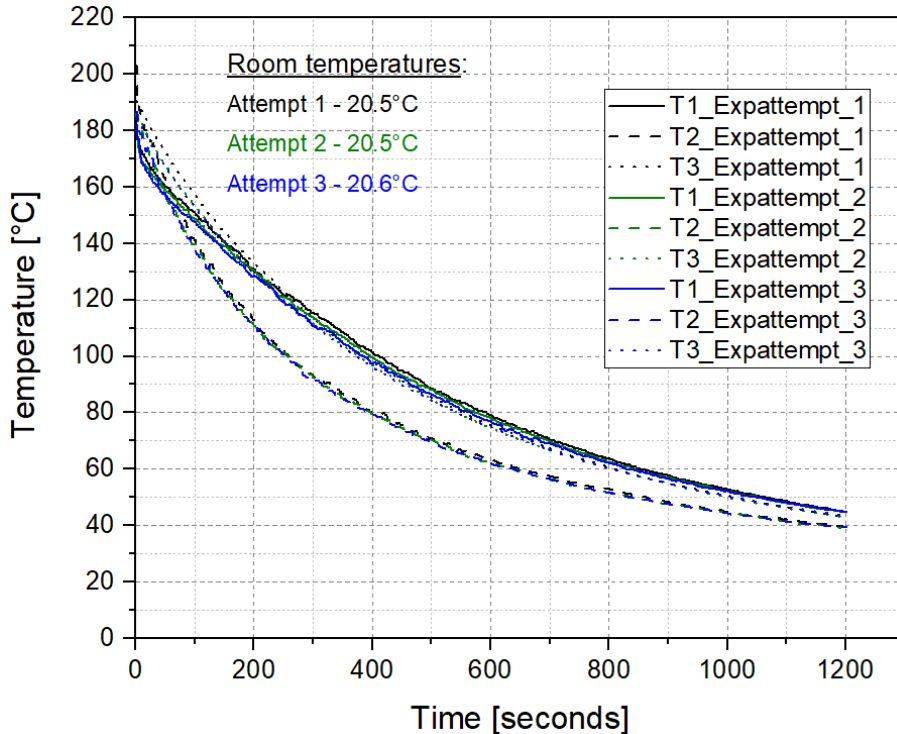


Figure 4.12: Experimental cooling trials of the GFRP

In the subsequent subsection, the production process of the hybrid plate and in particular the cooling stage of the process is discussed briefly.

### 4.2.3 Process of producing hybrid plate

The production of hybrid plate was done in two attempts. In the first attempt, the manufactured hybrid plate was used to cut out the 3-point-bend specimens. But in this production process, the measured temperature curve was not adequate enough to define a proper working cooling procedure. Hence, it was decided to manufacture a second DCB hybrid plate so that the temperatures could be properly recorded and be used for the simulation. Initially the GFRP laminate was fixed on the support plate using the kapton tape. The kapton tape was stucked for a initial crack propagation length of 60 mm. The temperatures were measured at two different points as displayed in the figure 4.13. These two points were chosen to know more about the temperature at the boundary of the adhesive and GFRP, also underneath the surface of the laminate and support plate since this was of important concern to validate the temperatures obtained from the cooling experiments in subsection 4.2.2. Hereupon the GFRP along with support plate was placed inside the oven and heated it upto 260° C. Once it had attained this temperature it was placed under the press (as deliberated in section 4.1.1 for producing hybrid plate) and the steel along with the adhesive placed over it and pressure of 0.25 N/mm<sup>2</sup> equivalent of force of 10 kN was applied. The platens of the press were already maintained at 150° C since the

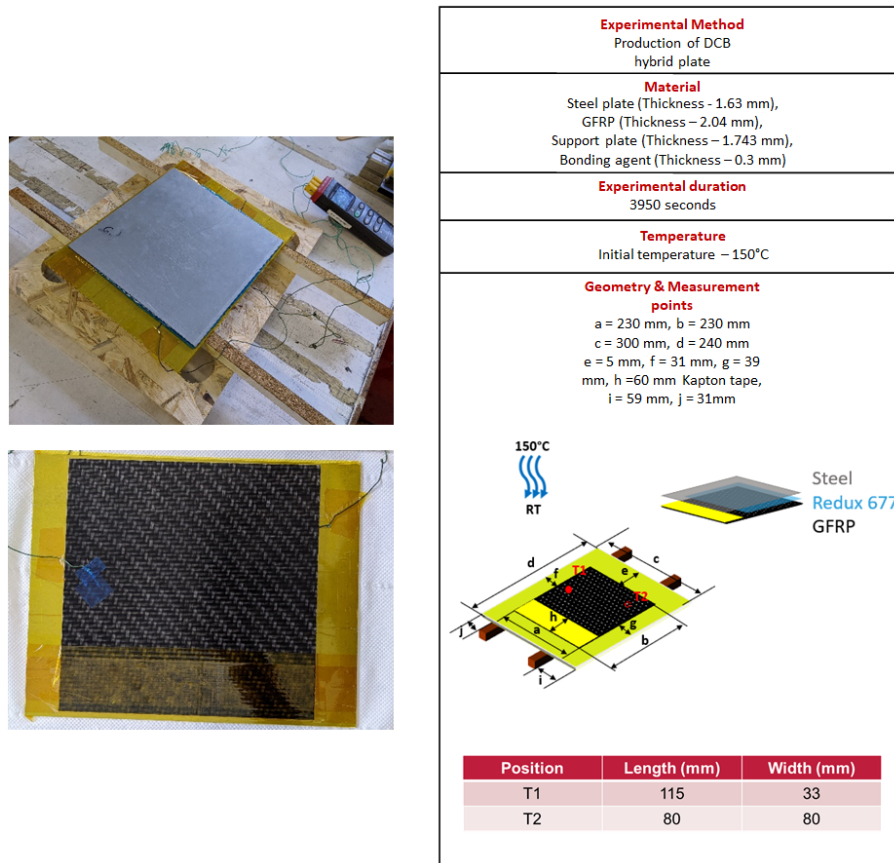


Figure 4.13: Production of DCB hybrid plate

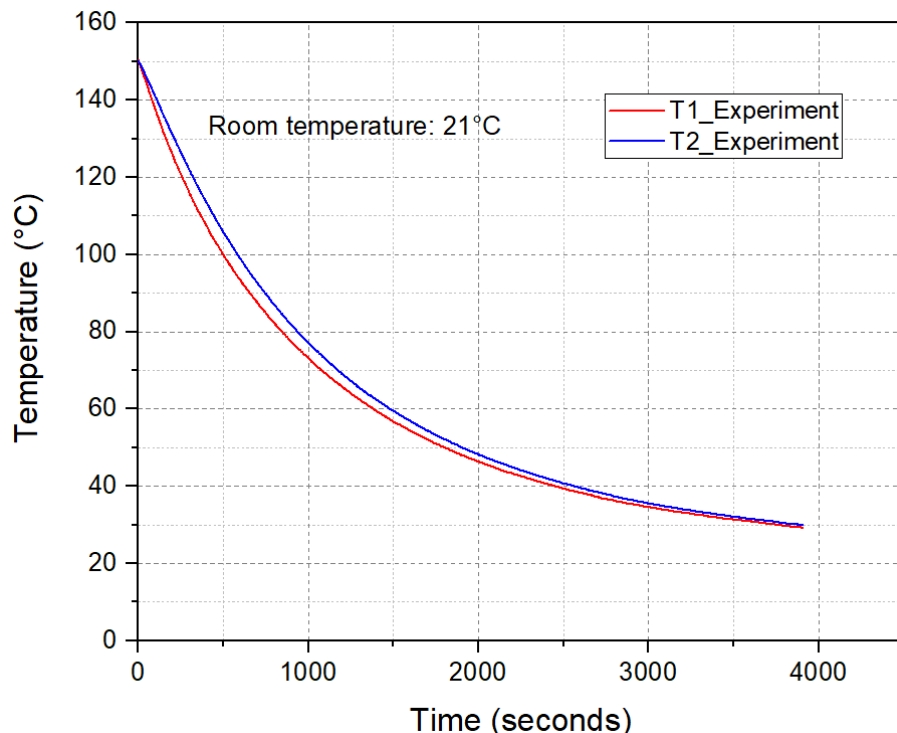


Figure 4.14: Cooling curves of the measured points

bonding agent had to be cured at this temperature for about 5 minutes. The temperature of the GFRP at which the Steel and BA pressed against it was 195 °C. This was bit lesser than the melting temperature of GFRP, since the transfer of GFRP from oven to the press was a tedious procedure. After the pressing procedure was completed, the complete setup was taken outside and placed on the wooden platform to allow it to cool it to room temperature. The temperatures were recorded using thermocouple which is presented in the figure 4.14. The temperatures were recorded for about 3950 seconds and as expected the temperature at the point measured underneath the surface of the GFRP in contact with the support plate cooled at a slower rate compared with the accomplice. In this way, the production of the hybrid plate was completed and to verify this process as an enlisted one by analyzing the deflections of the joining partners, a validation experiment was conducted which is contemplated in the following subsection.

#### 4.2.4 Validation of production procedure

To verify the procedure which had been adapted for producing the hybrid plate was validated using the setup shown in the figure 4.15.

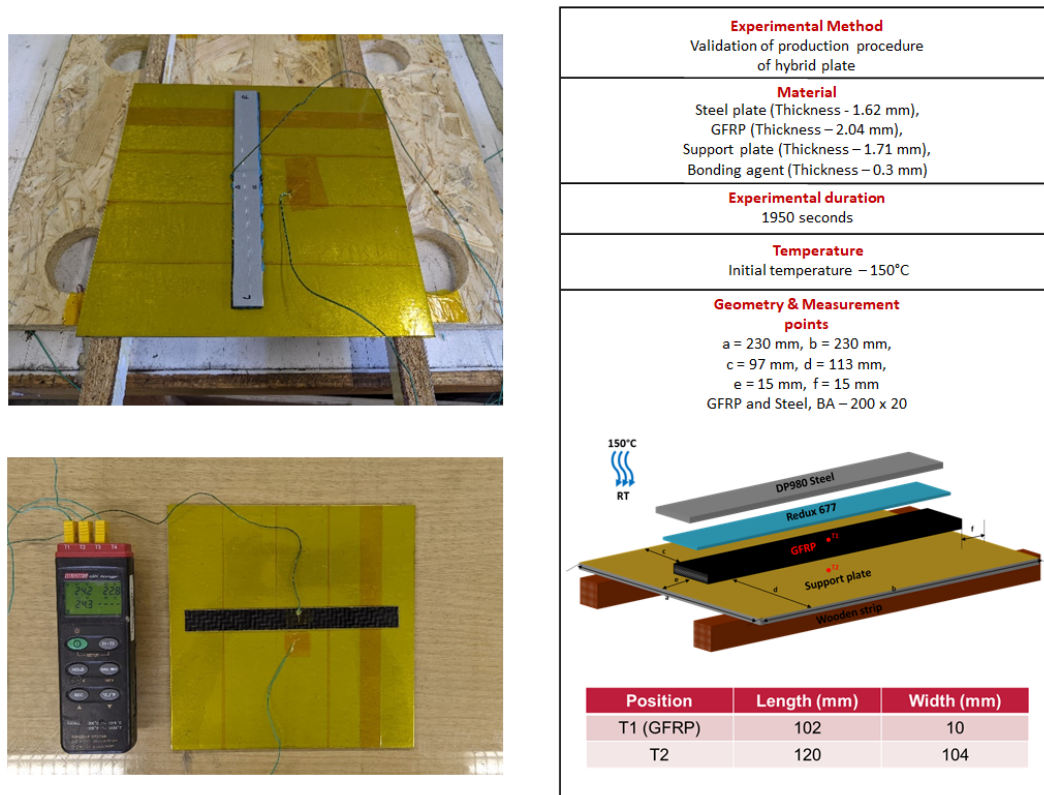


Figure 4.15: Validation setup of the experimental process

The same procedure had been carried out as illustrated in the subsection 4.2.3. But the specimen geometry alone and the applied pressure was different from the

hybrid plate production. Since a calculated pressure of  $0.14 \text{ N/mm}^2$  was not able to set in the machine, the next level of pressure of  $0.25 \text{ N/mm}^2$  which is an equivalent of  $1 \text{ kN}$  was applied. The temperatures were recorded on the surface of the GFRP specimen and on the support plate and displayed in the figure 4.16. It was decided to conduct at least three attempt of this validation procedure to ensure the correctness. But only two attempts were completed because of the need of the bonding agent for the experiments in near future to build up the temperature dependent cohesive zone model. Only two attempts were tried of which in the first trial, the pressure applied was too much and much of the bonding agent was lost at the joining zone as presented in figure 4.17.

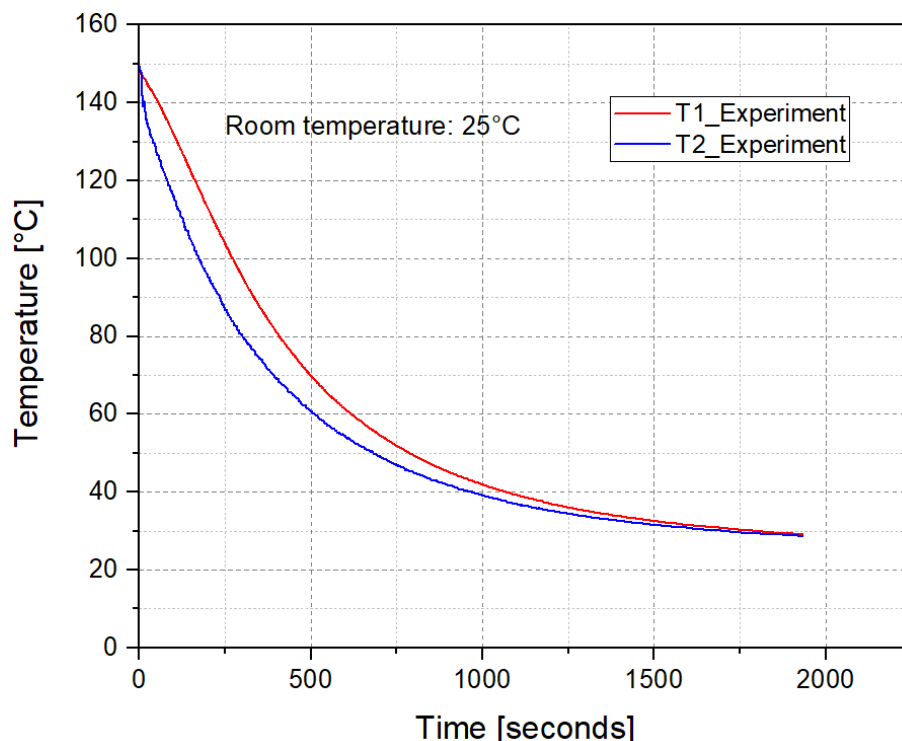


Figure 4.16: Cooling curves of the measured points

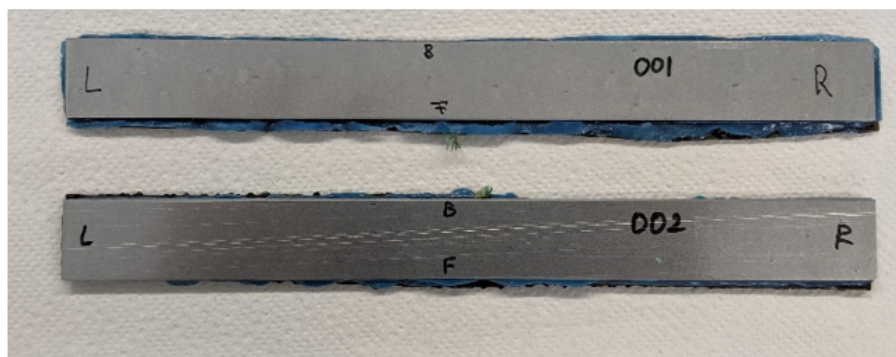


Figure 4.17: Trials made for validation experiment

The goal of this validation was to calculate the deflections in the Steel joining partner as a result of the CTE mismatch which happens during the cooling process. So, the steel joining partner was alone measured with the help of the linear extensometer available at IFS before and after the validation experiment. The deflections which occurred as a result of this cooling process is shown in the figure 4.18.

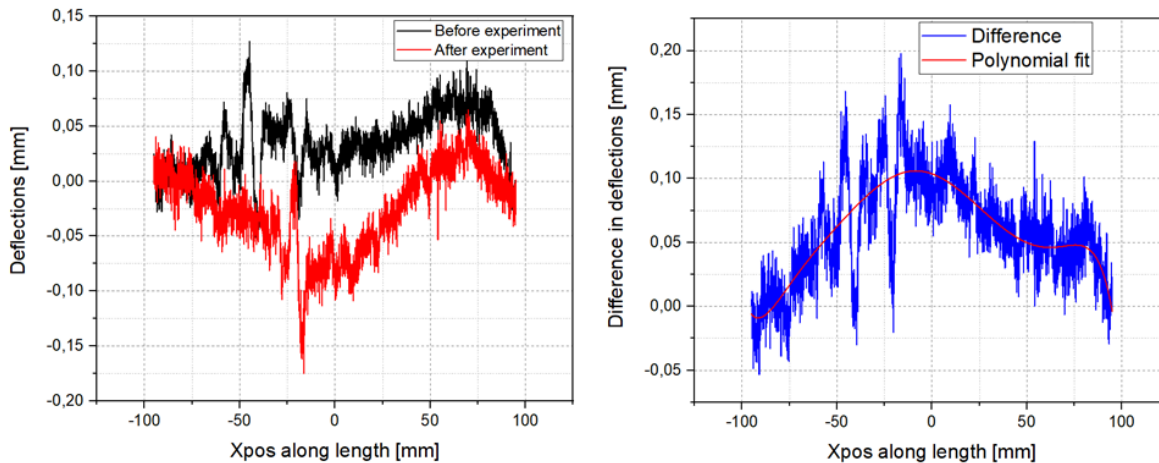


Figure 4.18: Deflections measured before and after experimental process

A maximum deflection of about 0.1 mm was found in the centre of the steel. But also there was an increase towards the end region, but this plateau was because of the reason that the steel along with the adhesive was not properly aligned over the GFRP when applying the pressure. This misalignment is shown in the figure 4.19. This should have induced some improper contractions within the metal partner and the reason for this behavior.



Figure 4.19: Misalignment of the steel joining partner on the GFRP

Thus the experiments related to the process and its validation were explained in detail in the above sections and the mechanical tests are explained in the following section.

## 4.3 3-point-bending experiments

The performed bending experiments according to the standard DIN EN ISO 14125 for the materials Steel, GFRP and the hybrid specimens in the Instron 30 UTM are interpreted in this section.

### 4.3.1 Flexural tests for Steel

Initially 8 steel specimens were decided for the flexural tests. Of that 5 specimens was initially subjected to the bending tests without performing the CDC process and remaining 3 specimens with CDC process. This was done to compare the effect of the CDC process on the DP980 steel specimens and also to harden it. The experimental setup and the force-displacement curves obtained are displayed in the figure 4.20.

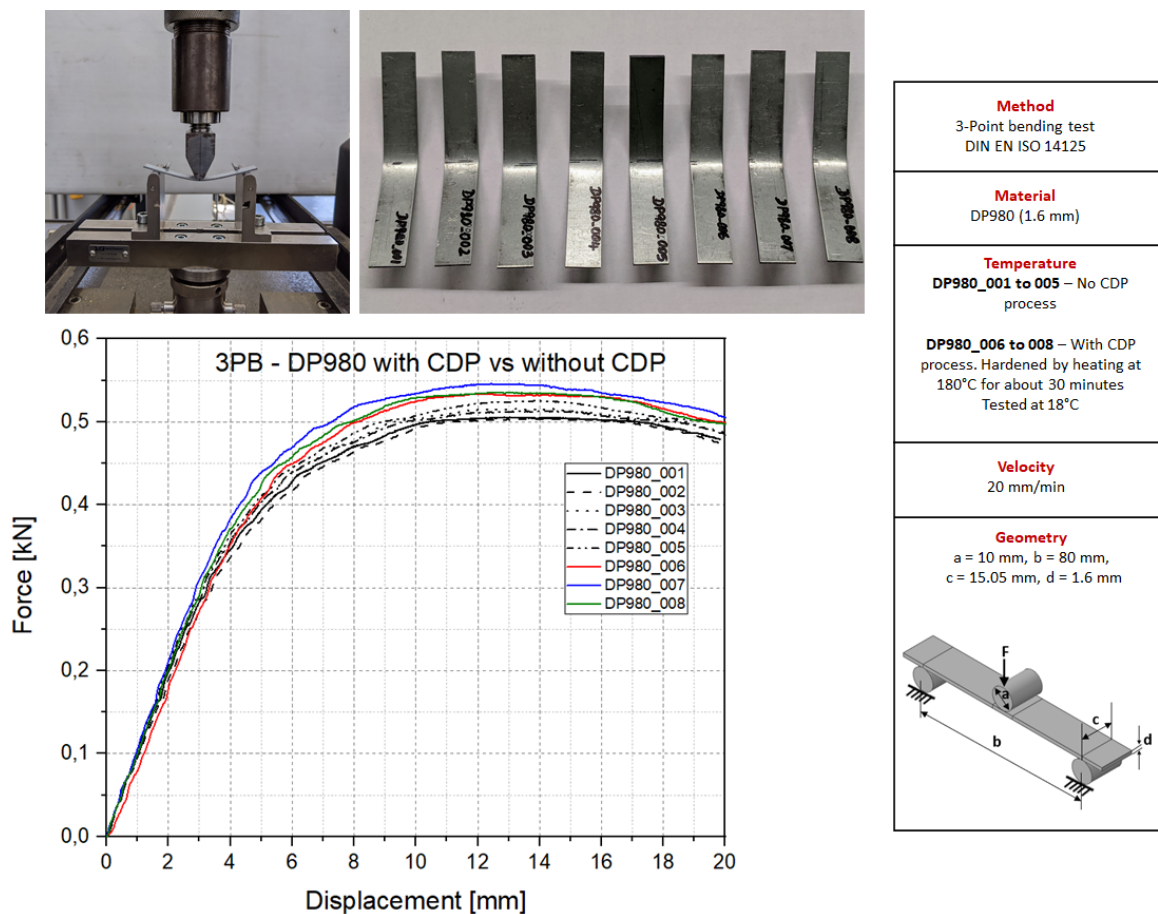


Figure 4.20: Force-Displacement curves of 3PB of DP980 Steel

It was found that the yield strength increased for the specimens 6 to 8 after being subjected to the hardening procedure. For the specimens 1 to 5, the width was measured only on the two edges whereas for the specimens 6 to 8, the width was

measured at five different places along the length to eliminate the deviations with regard to the dimensions. Finally, the specimens 1 to 5 were not considered while developing the simulation model as it was not subjected to the CDC process. The measurements of the specimens are summarized in the table 4.1.

Table 4.1: DP980 Steel 3PB specimen measurements

Specimen	Length [mm]	Width [mm]	Thickness [mm]
DP980_001	99.8	14.88	1.6
DP980_002	100.2	14.88	1.6
DP980_003	100.3	15.03	1.6
DP980_004	100.4	15.23	1.6
DP980_005	99.6	15.25	1.6
DP980_006	99.8	14.90	1.6
DP980_007	100.7	15.24	1.6
DP980_008	99.8	15.02	1.6

### 4.3.2 Flexural tests for GFRP

The experimental setup and the force-displacement curves obtained for the bending

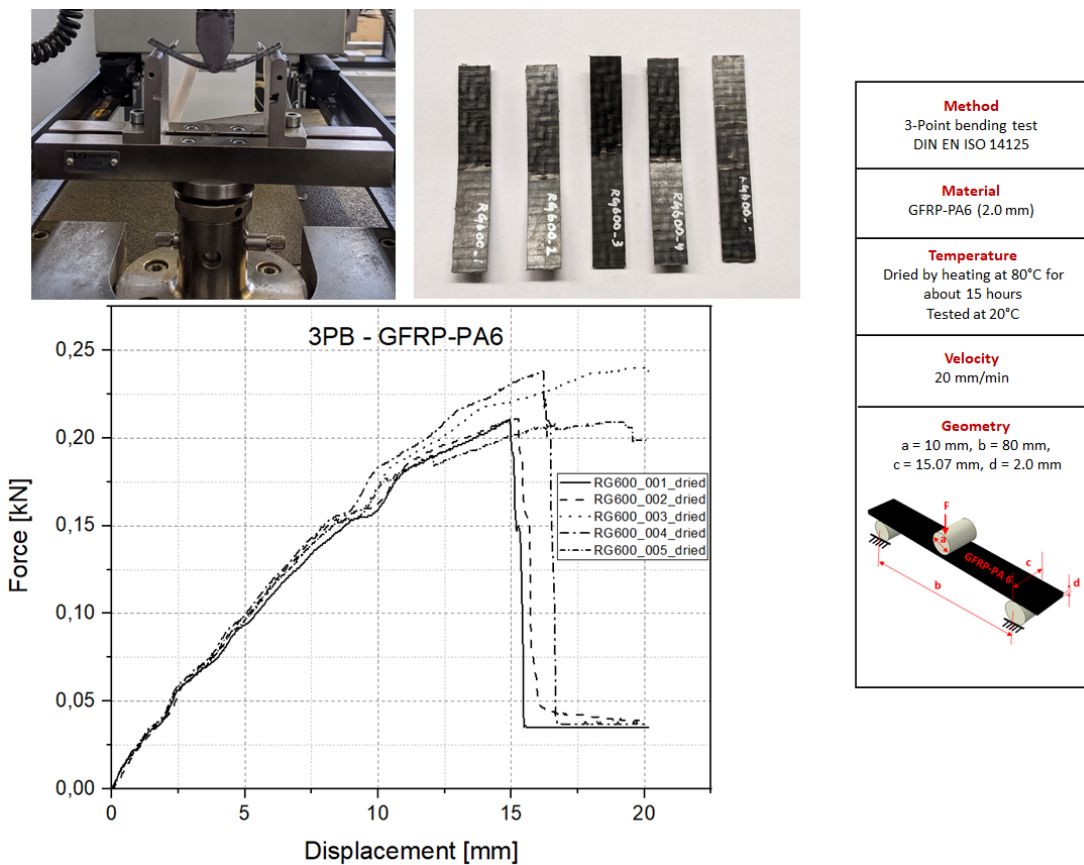


Figure 4.21: Force-Displacement curves of 3PB of GFRP-PA6

test of GFRP is presented in the figure 4.21. The 3-point-bending tests were done for 5 specimens of GFRP material to characterize the material properties which was needed for the simulation. The specimens were cut using the saw mill available at IFS. Since it was subjected to water cooling while cutting, to remove the moisture content the specimens were heated at 80 ° C for about 15 hours. The width was measured at five different points along the length of the specimen same as like steel. The measurements of the GFRP specimens are listed in the table 4.2.

Table 4.2: GFRP 3PB specimen measurements

Specimen	Length [mm]	Width [mm]	Thickness [mm]
RG600_001	99.08	15.04	2.01
RG600_002	99.97	15.08	2.04
RG600_003	99.20	15.04	1.97
RG600_004	99.50	15.12	1.98
RG600_005	99.65	15.11	2.01

### 4.3.3 Flexural tests for Hybrid Steel/GFRP-PA6 specimen

The experimental setup and the force-displacement curves obtained for bending of

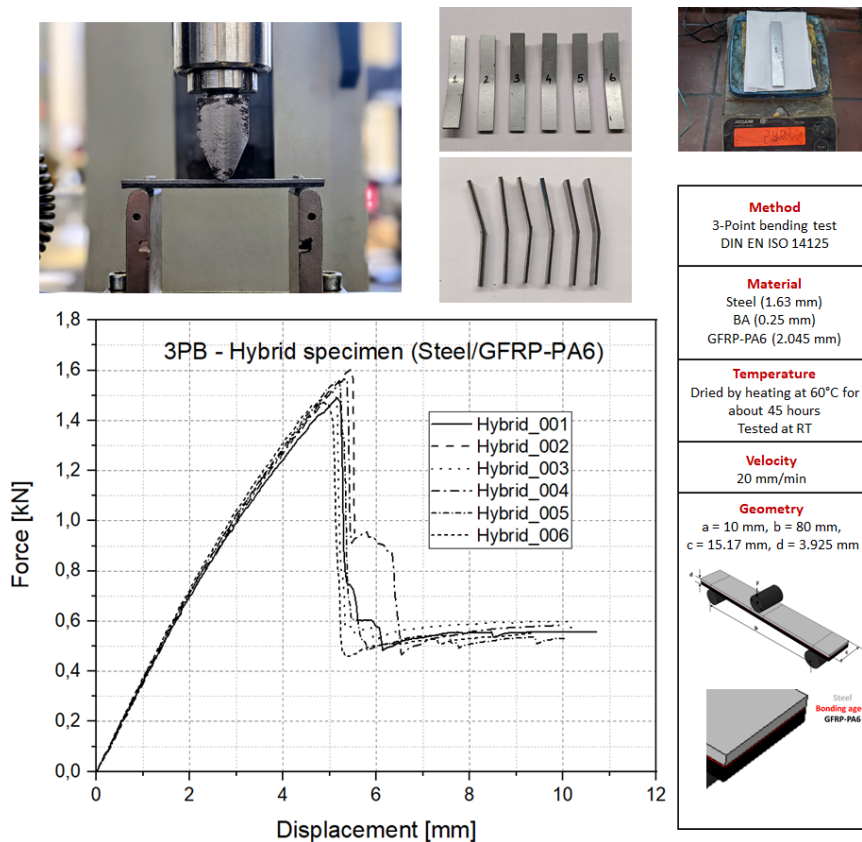


Figure 4.22: Force-Displacement curves of 3PB of Hybrid specimens

hybrid specimens is in the figure 4.22. The hybrid specimens were cut out from the water jet cutting machine available at OHLF. Since the specimens might had absorbed moisture during the cutting operation, they were dried for about 45 hours at 60° C. Also the specimens were weighed before and after the drying process to see if it had influenced the reduction of weight because of moisture content. The width of the specimens was measured in the same way as earlier discussed. The weight measurements before and after the drying process is listed in table 4.3 and the dimensions are provided in table 4.4. The thickness measurements (total thickness) for the hybrid specimens are also done at five places along the length.

Table 4.3: Weight measurements before and after drying

<b>Specimen</b>	<b>Weight [gm] Before putting into oven</b>	<b>Weight [gm] After taking from oven</b>
Hybrid_001	23.8	23.7
Hybrid_002	23.7	23.7
Hybrid_003	23.7	23.7
Hybrid_004	23.7	23.7
Hybrid_005	23.7	23.7
Hybrid_006	23.8	23.7

Table 4.4: Hybrid 3PB specimen measurements

<b>Specimen</b>	<b>Length [mm]</b>	<b>Width [mm]</b>	<b>Thickness [mm]</b>
Hybrid_001	100.14	15.18	3.98
Hybrid_002	100.05	15.20	3.97
Hybrid_003	100.15	15.16	3.98
Hybrid_004	100.15	15.17	3.97
Hybrid_005	100.15	15.16	3.96
Hybrid_006	100.14	15.15	3.99

It was found that the load-carrying capability of the hybrid specimen is almost three times than the DP980 steel specimen. The drop in the load indicates the failure which also occurred with the individual GFRP-PA6 bending specimens. The failure modes were local internal plasticity effects at the point of impact of the GFRP followed by the complete fracture and the debonding at the interface as shown in the figure 4.23. The failure mode is almost the similar in all the hybrid specimens as found in the figure for the **Hybrid-006**. Also there were some defects which arose as a result after the process as found in the figure for the specimen **Hybrid-004**. These defects are due to the resin evaporation forming cavities in certain regions which reduces the strength of the GFRP. These cavities were almost found in all other specimens also but on a minimal scale.

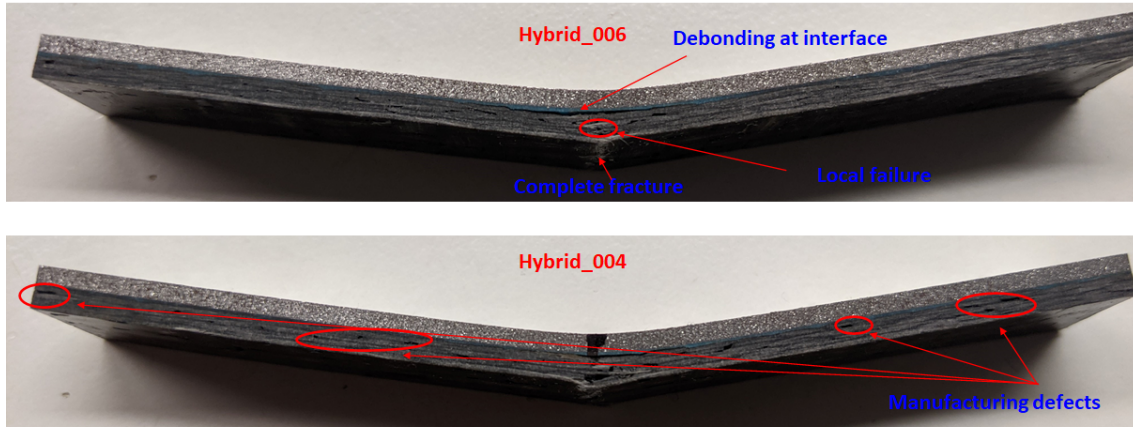


Figure 4.23: Failure mode and defects of the hybrid specimens

The hybrid specimens with fibers along the 0° direction were tested for the individual and hybrid specimen bending tests. As per [41], the fibers along the 90° direction exhibited little improvement and hence it is not considered in this investigation.

Thus, the experimental works related to both the process and the structural tests were performed and in the next chapter, the finite element modelling aspects of the experiments will be carried out.

# 5 FEM simulation

In this chapter, the findings from the cooling experiments (refer section 4.2.2) of the different materials will be validated by using the FE model. The material model built up to validate the experimental results will be carried forward for the final process simulation. The stages of building up the FE model and material model are elaborated in the following sections.

## 5.1 Process

### 5.1.1 Simulation strategy

The objective of the thesis is to analyze the cooling of the joining partners and the resultant structural deformations which would have a negative effect on the adhesive. The simulation strategy is based on the software capabilities of ABAQUS™. ABAQUS™ has two analysis types - Explicit and Standard. ABAQUS™/Standard is chosen in this research since it is efficient in solving smooth nonlinear problems whereas the ABAQUS™/Explicit solves every problem as a wave propagation analysis. Levent et al.[11] concentrated on the temperature and shear-rate dependent behavior of the plastic based on the simulation technique of ABAQUS™/Explicit and fully coupled thermal-stress analysis since the mechanical analysis is dependent on the temperature field and the temperature field is dependent on the stress/displacement solution. In this work, since the focus is on the cooling phase alone (refer section 3.3), a simulation strategy by conducting a free convective heat transfer analysis first and transferring the temperature results to the next stage so that the mechanical effect of the joining partners on the adhesive can be thoroughly studied. This strategy is known as the sequentially coupled thermal-stress analysis. Since the heat transfer to the surrounding is time-dependent the transient analysis is chosen for the heat transfer analysis and for the structural simulation the static, general analysis is chosen since there is no influence of inertia effects. Though the computational time is considerably less for a 2D case, the parts were modelled in the FE software in 3D space. Another disadvantage of the shell element parts is that the placement of the joining parts over each other will coincide in space and would not be realistic to visualise the results through the thickness [72]. Hence the element types such as heat transfer elements DC3D8 (An 8-node linear heat transfer brick) and structural elements C3D8R (An 8-node linear brick, reduced integration, hourglass control) and the cohesive element COH3D8 for the adhesive (An 8-node three-dimensional cohesive element) were used in the simulation. In the following sections, the validations were done for the individual components of the hybrid plate for which the cooling experiments were done.

### 5.1.2 Material model buildup

At the beginning of this section, the film condition which is required for the individual joining partners are validated by comparing against the experimental results. Ensuring that, material properties such as the elastic and thermal expansion parameters for few materials are reviewed.

#### Steel plate

A steel plate FE model depicted in the figure 5.1 in accordance with the dimensions of the steel plate (refer subsection 4.2.2) which was used for the cooling experiments is modelled. The thermal properties such as the Density, Thermal conductivity and Specific heat capacity used for the thermal analysis is summarized in table 5.1.

Table 5.1: Thermal properties used for Steel FE model [25]

Property	Symbol	Unit	Steel
Density	$\rho$	ton mm <sup>-3</sup>	7.85e <sup>-9</sup>
Thermal conductivity	$k$	mW mm <sup>-1</sup> K <sup>-1</sup>	52
Specific heat capacity	$c_p$	mJ ton <sup>-1</sup> K <sup>-1</sup>	0.48e <sup>9</sup>

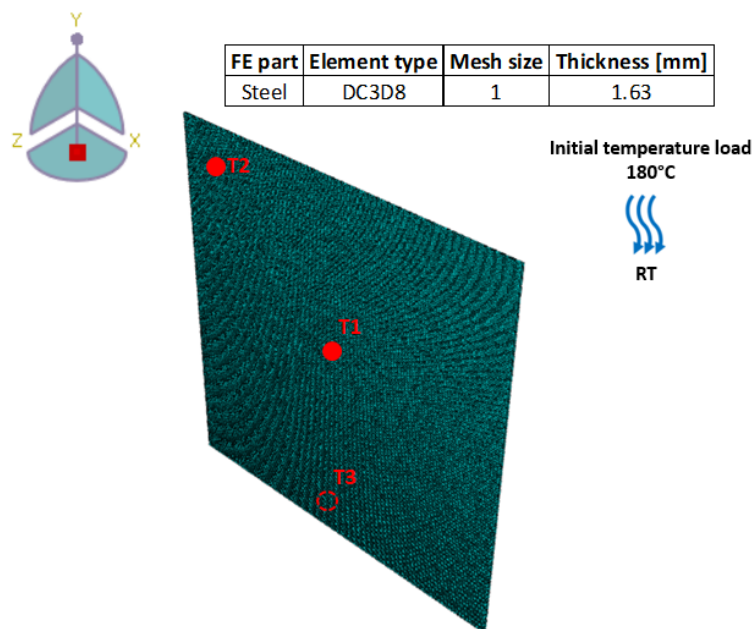


Figure 5.1: Steel plate FE model

A predefined temperature load of about 180 °C is applied to the model and the film condition coefficients were sorted so that it is cooled down to the room temperature 20.5 °C which is the average of the experimental trials. The simulation was done only once since the room temperatures almost remained the same and the cooling rate

did not have much difference between all the experimental trials. The temperature was measured exactly at the respective nodes and to facilitate this a global mesh size of 1 is applied. The film condition is employed temperature dependent so as to capture the actual cooling behavior of the experiment. The film coefficients which were used to fit and the comparison between the simulation and experimental results is displayed in table 5.2 and figure 5.2 respectively.

Table 5.2: Temperature-dependent film coefficients finalized for Steel plate

<b>Steel film coefficient</b> [mW mm <sup>-2</sup> K <sup>-1</sup> ]	<b>Temperature</b> [°C]
0.003	20
0.0065	80
0.0065	140
0.011	160

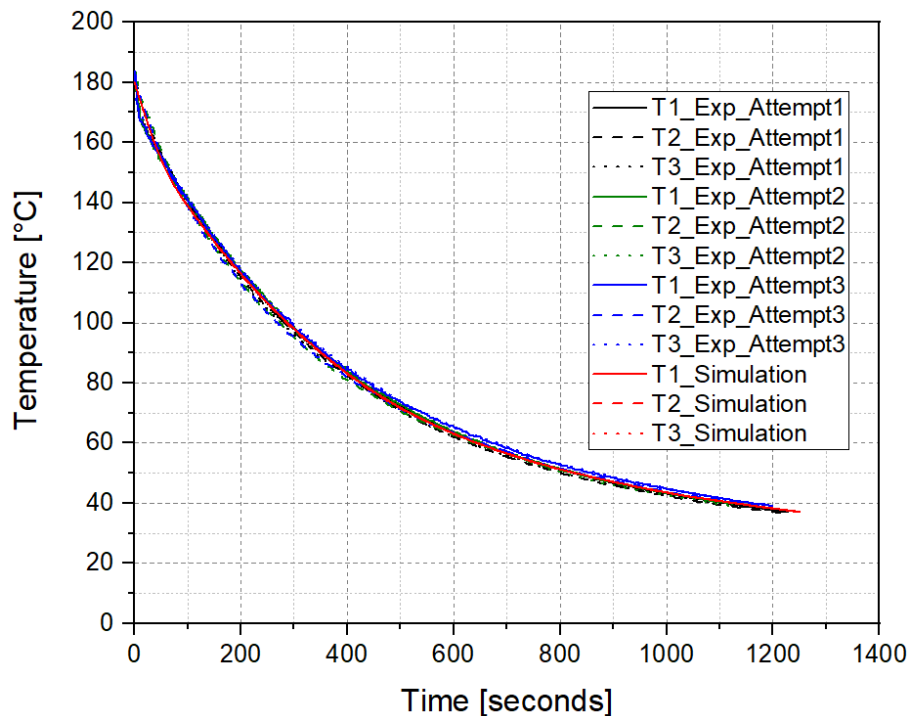


Figure 5.2: Experimental vs Simulation results comparison for Steel plate

It was found that the temperature at the measured points in the simulation model replicated the behavior of the experimental trials. The difference between the measured points in the experiment differed little bit such as the T3 cooled slower than T1 and T2. But this difference was not seen in the simulation and it is very minimal such that it can be ignored.

## Support plate

As it is known that, the support plate with kapton and without kapton behaves in a different way (refer subsection 4.2.2) the support plate FE model differs a bit from the Steel plate FE model. The FE model of the support plate is shown in the figure 5.3. In order to exactly apprehend the physical behavior of the support plate, different film conditions were applied on the top and the bottom side. This was due to the faster cooling rate which happens on the top side where it is wounded with kapton tape and on the bottom has a slower cooling rate where it is not wounded with kapton tape. The film coefficients obtained from steel plate is applied on the bottom side and on the top side it was sorted to have a proper fit to the experimental results.

Table 5.3: Thermal properties used for Support plate FE model [26]

Property	Symbol	Unit	Support plate	Wooden strip
Density	$\rho$	ton mm <sup>-3</sup>	7.85e <sup>-9</sup>	5.48e <sup>-10</sup>
Thermal conductivity	$k$	mW mm <sup>-1</sup> K <sup>-1</sup>	52	0.14
Specific heat capacity	$c_p$	mJ ton <sup>-1</sup> K <sup>-1</sup>	0.48e <sup>9</sup>	1.63e <sup>9</sup>

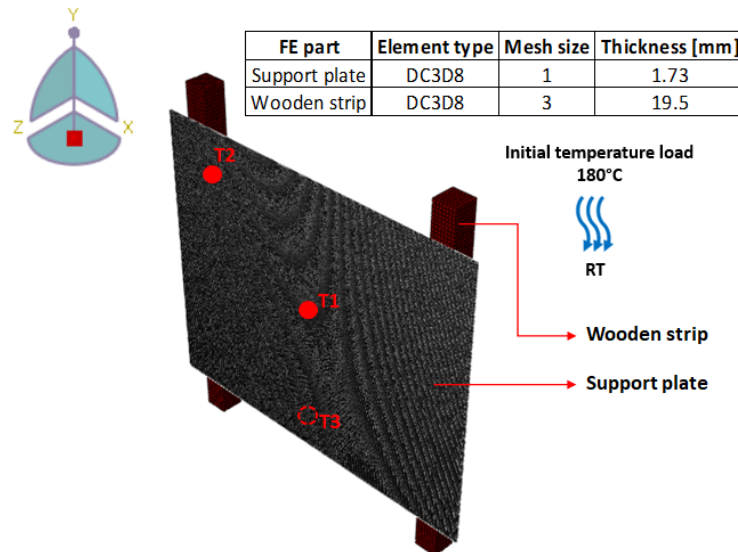


Figure 5.3: Support plate FE model

There was also the necessity of adding the wooden strips in the model since in the actual hybrid plate cooling process the temperature difference between the top and the bottom part of the support plate was high since the insulation material serves as an element for a gradual cooling on the bottom surface. But it will not be required for the steel plate (in section 5.1.2) because in the hybrid plate cooling process it is not in direct contact with the wooden strips unlike the support plate and GFRP laminate. So in order to correlate with actual cooling behavior of the support plate and GFRP,

the wooden strips were added. The wooden strips were precisely placed in the FE model according to the measurements from the experiment where it was bonded by tape to the wooden base to eliminate the movement of the strips after the support plate is placed on it. The dimension of the wooden strips is (19.5 mm x 19.5 mm x 300 mm). The thermal properties such as the Density, Thermal conductivity and specific heat capacity is employed according to [26] which is listed in the table 5.3. In this case, the boundary conditions are not required for the transient heat transfer analysis. An initial temperature load of 180 °C was applied only to the support plate and it cooled down to room temperature of 20.3 °C which is the average of the experimental attempts. The film condition from Steel plate is applied on the areas of bottom surface of support plate which are not in contact with the wooden strips. The support plate is connected with the strips by means of \*TIE connection so that the heat transfers from steel to wood. The simulation results compared against the experimental results of support plate with kapton tape having measurement points (from section 4.2.2) is depicted in the figure 5.4. The film coefficients adapted to fit the experimental cooling curves are summarized in the table 5.4. It was found that the T2 temperature initially did not have good correlation with the experimental results. But if the film coefficients are changed incorrectly then the actual physical behavior will be violated which is not accepted. Hence, the coefficients were fitted in a way that it compromises all the temperature measurement results.

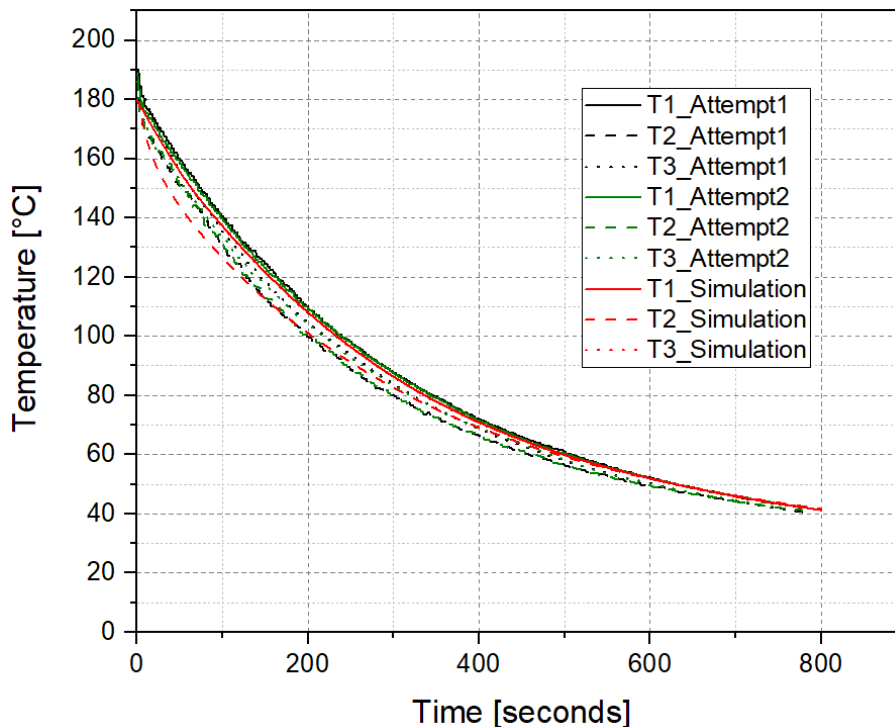


Figure 5.4: Experimental vs Simulation results comparison for Support plate

Table 5.4: Temperature-dependent film coefficients finalized for Support plate

<b>Support plate top film coefficient [mW mm<sup>-2</sup> K<sup>-1</sup>]</b>	<b>Support plate bottom film coefficient [mW mm<sup>-2</sup> K<sup>-1</sup>]</b>	<b>Temperature [°C]</b>
0.003	0.003	20
0.0105	0.0065	80
0.0105	0.0065	140
0.0105	0.011	160

## GFRP

To validate the experimental cooling trials of the GFRP laminate (refer subsection 4.2.2), the simulation model is created as shown in the figure 5.5. The procedure for simulating the cooling process is similar to the steel and support plates. The temperatures T2 was recorded at the support plate and also the T3 at the interface of the GFRP and the support plate. The intention is to use the film coefficients obtained from the support plate (in table 5.4) to find out the temperature dependent film coefficients for the GFRP laminate.

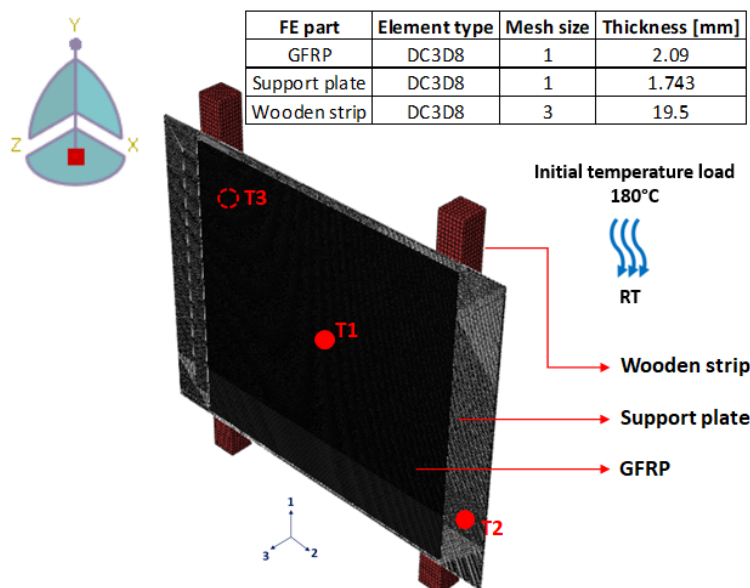


Figure 5.5: GFRP cooling FE model

Table 5.5: Thermal properties used for GFRP FE model [27]

<b>Property</b>	<b>Symbol</b>	<b>Unit</b>	<b>GFRP</b>
Density	$\rho$	ton mm <sup>-3</sup>	1.8e <sup>-9</sup>
Specific heat capacity	$c_p$	mJ ton <sup>-1</sup> K <sup>-1</sup>	0.948e <sup>9</sup>

Table 5.6: Thermal conductivity of GFRP in unit convention  $\text{mW mm}^{-1}\text{K}^{-1}$  [27]

Property	k11	k22	k33
Thermal conductivity	0.599	0.383	0.383

The thermal properties of the wooden strip and also the support plate (in table 5.3) was used. The thermal properties of the GFRP listed in the tables 5.5,5.6 is collected from the research article [27]. Apart from the previous steel and support plate simulation models, one different aspect of this model is assigning the material orientation for the GFRP. This is because the thermal conductivities of the FRP materials are different along the longitudinal and transverse directions. The orientation is defined by creating a coordinate system and assigning it to this material in order to be the properties implemented for it. The numbering system provided in the figure 5.5 shows the material orientation direction for which the properties from the table 5.6 will be applied. An initial condition of  $180^\circ\text{C}$  is applied as a predefined temperature load and cooled down to room temperature  $20.5^\circ\text{C}$  which is the average of the three experimental attempts. The GFRP is connected to the support plate and in return the support plate is connected to the strips by means of \*TIE connection. The experimental and the simulation results are compared in the graph shown in the figure 5.6.

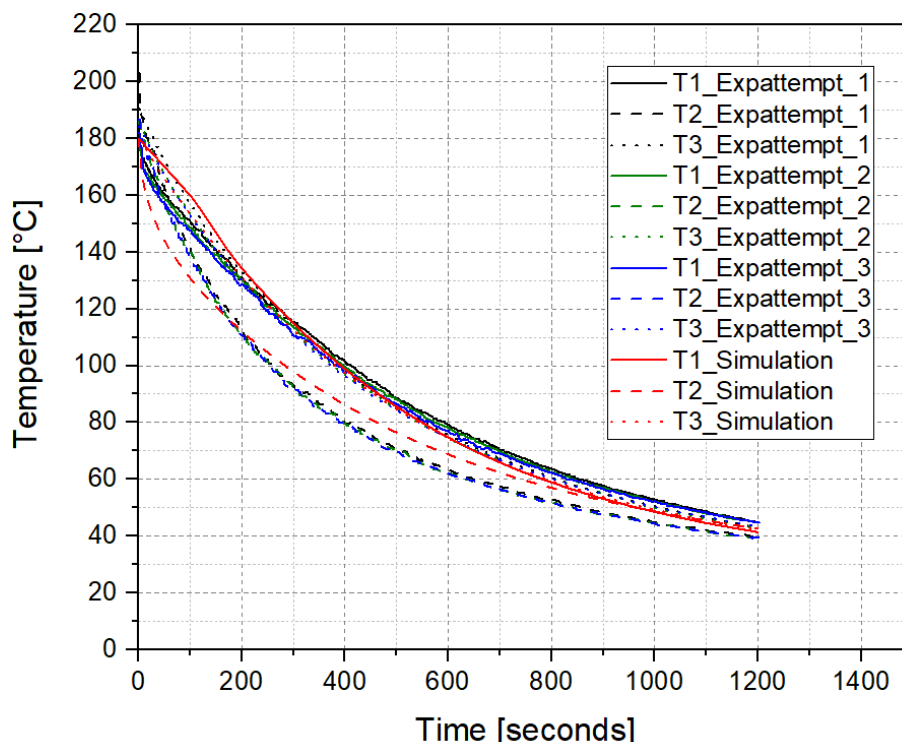


Figure 5.6: Experimental vs Simulation results comparison for GFRP

It was seen that T2 cooled faster since the support plate is wound with kapton tape. Although, a maximum difference of about 5 to 6 degrees is found for the support plate

experimental and simulation results, if the film coefficients are changed again then it will lead to the higher temperature difference of T1 and T3 as they are inter related to this. Hence a final list of temperature dependent film coefficients for the GFRP is summarized in the table 5.7.

Table 5.7: Temperature-dependent film coefficients finalized for GFRP

GFRP film coefficient [mW mm <sup>-2</sup> K <sup>-1</sup> ]	Temperature [°C]
0.012	20
0.01	80
0.009	140
0.002	160

Thus the film coefficients of the individual components of the hybrid plate required for the cooling simulation are evaluated. The need of the elastic properties of the bonding agent and GFRP will be evaluated by conducting the Dynamic mechanical analysis (DMA) experiments. Since this is not part of the task, only the results are reviewed in the following subsection.

### DMA analysis - GFRP and Redux® 677

Firstly, the DMA experiment for the dried GFRP laminates of length 90 mm, width 7 mm and thickness 2.01 mm was carried out. The purpose of this is to know about the elastic properties of the laminate based upon the temperature since it is an essential behavior prospect under higher temperatures. The results are depicted in figure 5.7.

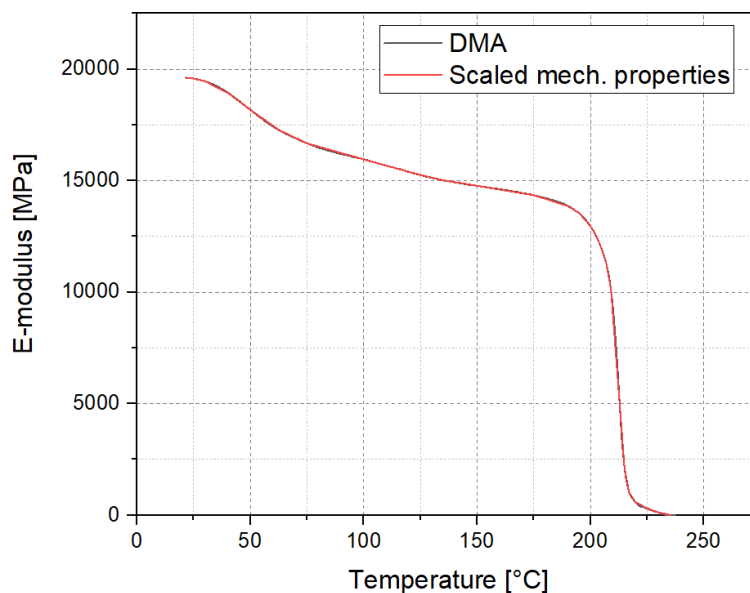


Figure 5.7: Scaled temperature dependent elastic properties of GFRP

It is clearly seen that as the temperature increases, the elastic modulus decreases gradually and once it reached the melting temperature of 220 °C, there is a sudden drop in the values since the resin which binds the fibers tends to evaporate and the laminates loses its strength subsequently. These properties are to be used in the cooling process simulation by defining them as engineering constants. Secondly the DMA experiment for the bonding agent or the adhesive Redux® 677 of length 9 mm, width 4.1 mm and thickness 0.5 mm was carried out. Two attempts were done of which the elastic properties of the first attempt was scaled to fit the experimental result. The result is represented in the figure 5.8.

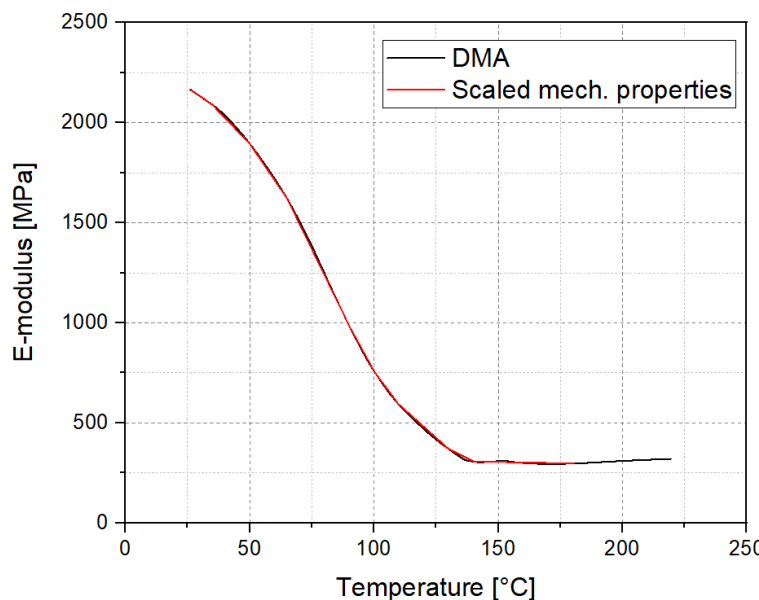


Figure 5.8: Scaled temperature dependent elastic properties of Redux® 677

It is seen that a maximum strength of about 2000 MPa at room temperature and it decreases where it attains a minimum value of around approximately 350 MPa after it crosses 100 °C. Hence, the temperature dependent elastic properties of the bonding agent will be employed in the process simulation model to predict the stresses which could occur as a result of the contraction of the joining partners.

### Thermal expansion coefficient - GFRP

The thermal expansion coefficient values of the laminate was experimentally observed and the temperature dependent values are displayed in the figure 5.9. The geometry which is used for measuring the thermal expansion coefficient has length of 11.5 mm, width 5.2 mm and thickness of about 2.1 mm. It was found that a value of  $1.77e^{-5}$  between 20 °C and 100 °C. Above that till 180 °C, a value of  $1.94e^{-5}$  was observed and these values has also to be employed in the simulation model. Also the thermal expansion coefficient values in the fiber as well as perpendicular to the fiber

direction should also be evaluated to know how the laminate behaves with respect to the cooling process which will be elaborated in the following section.

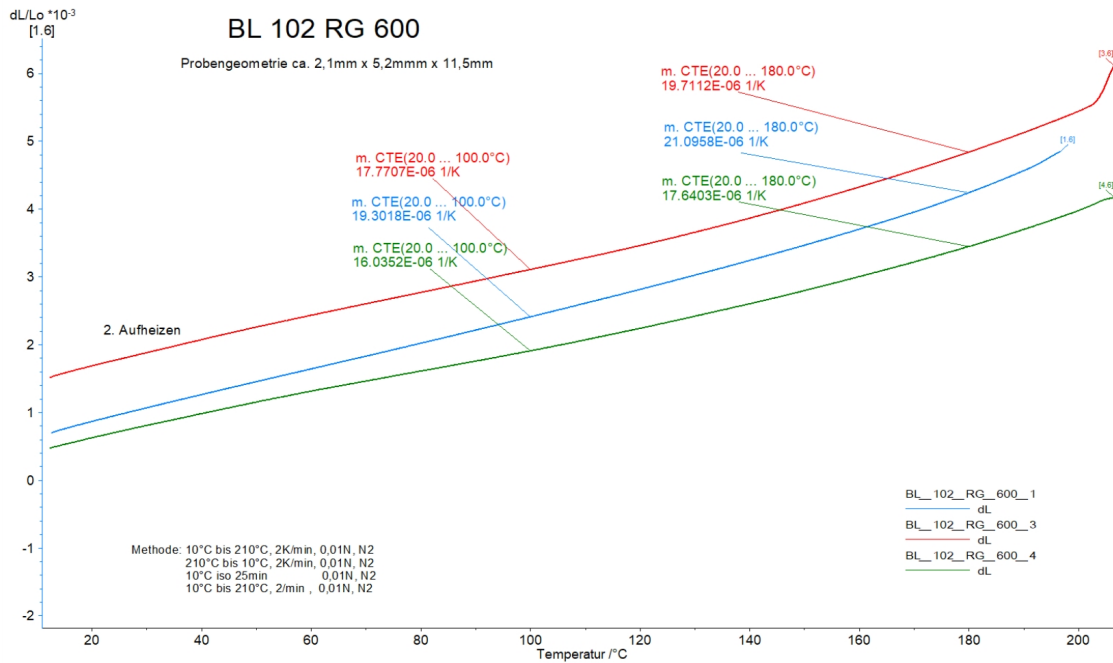


Figure 5.9: Thermal expansion coefficient of GFRP

Thus the required material properties for the process simulation are acknowledged and in the next section, the simulation results of the process will be deliberated.

### 5.1.3 Cooling process simulation FE model

The process simulation according to the simulation strategy provided in section 5.1.1 can be divided in two stages. The first stage is the free convective heat transfer analysis of the hybrid plate after taking it out of the press. Following that, the nodal temperatures can be transferred to carry out the mechanical analysis and interpret the results. Initially, the heat transfer simulation results are provided followed by the mechanical analysis results.

#### Thermal analysis

The thermal analysis FE model presented in the figure 5.10 has all the individual components from the preceding sections. The geometry is created exactly based upon the dimensions from the section 4.2.3. All the components are connected to each other by means of \*TIE connection. Since the cohesive elements in software does not have the heat transfer capability, the bonding agent is also meshed by the normal heat transfer elements. This will again be changed to the cohesive elements

in the mechanical analysis. Since the curing of the adhesive takes place at 150 °C for 4 to 5 minutes in the press, the initial temperature load will be 150 °C. But the cooling experiments for the individual components were done from 180 °C to the room temperature which could be used for simulating the CDP process at a later stage.

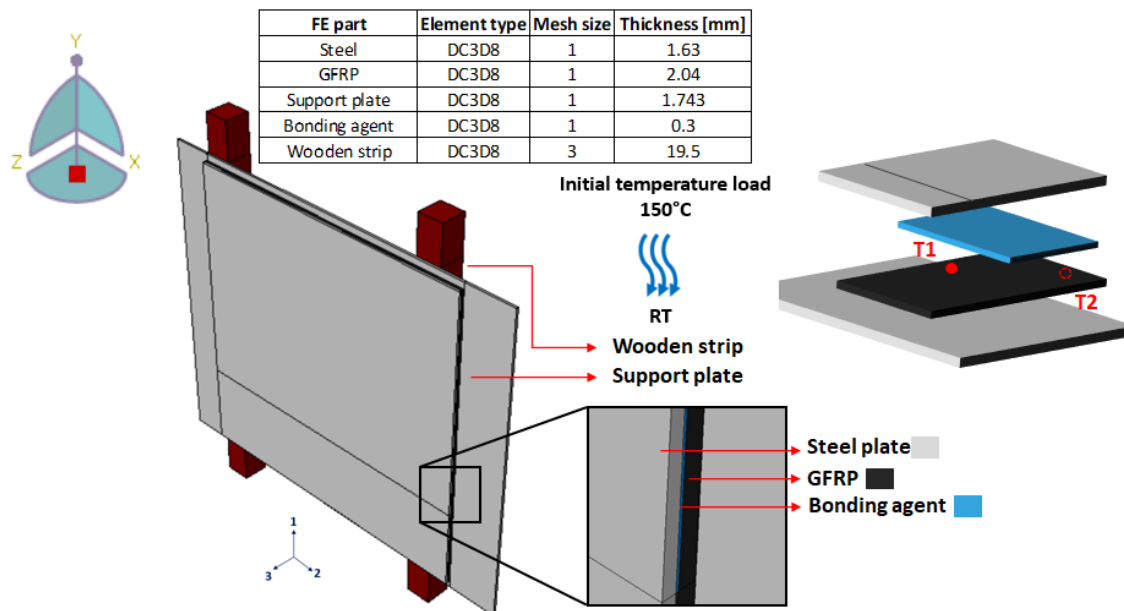


Figure 5.10: Process simulation thermal analysis FE model

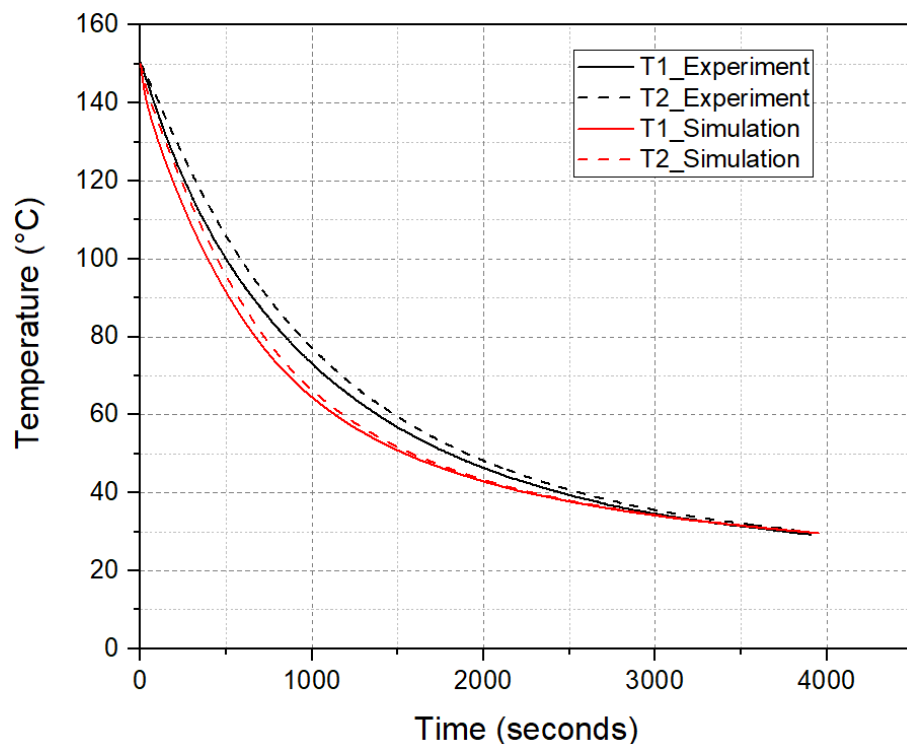


Figure 5.11: Cooling curves of the process simulation

By any means, the film coefficients from 150 °C is already available from the cooling simulations for the individual components and it can be applied to the process simulation. This was done to validate the film coefficients obtained from the preceding sections (refer tables 5.2, 5.4, 5.7) and correlate with the experimental result. An initial temperature of 150 °C is employed to all the components of the hybrid plate and it is cooled down to the room temperature of 21 °C. The simulation time period will be similar to the experiment for about 3950 seconds. The temperatures were measured at two different points as depicted in the figure 5.10. The thermal properties for the simulation is also based on the properties used in the sections before (refer tables 5.1, 5.3, 5.5, 5.6). The properties used for the bonding agent is listed in the table below 5.8. The simulation results had a difference of about 5 to 10 degrees when correlated with the experimental results which is acceptable. The nodal temperatures from the thermal analysis model has to be transferred to the mechanical analysis model which is contemplated in the following subsection.

Table 5.8: Thermal properties used for Bonding agent [28]

<b>Property</b>	<b>Symbol</b>	<b>Unit</b>	<b>Steel</b>
Density	$\rho$	ton mm <sup>-3</sup>	1.2e <sup>-9</sup>
. Thermal conductivity	$k$	mW mm <sup>-1</sup> K <sup>-1</sup>	2
Specific heat capacity	$c_p$	mJ ton <sup>-1</sup> K <sup>-1</sup>	1.2e <sup>9</sup>

## Mechanical analysis

The mechanical analysis is also similar to the thermal analysis FE model but it differs in only one aspect where the mechanical boundary conditions and the temperature results from the thermal simulation are to be applied. The mesh will be the same so as to facilitate the transfer of temperature results to the respective nodes. The load will be defined as the predefined field by importing the output database file (odb) from thermal simulation. The boundary conditions employed and the model setup is shown in the figure 5.12. The simulation time period is the same as that of the thermal analysis. The individual components are connected by means of \*TIE connection. The mechanical properties such as the elastic modulus and thermal expansion coefficients for the steel, support plate and wood (from [29, 30, 31]) are summarized in the table 5.9. The expansion of the insulation material is negligible and hence it is ignored. The elastic modulus and thermal expansion coefficient of the GFRP were measured by DMA experiments (refer figures 5.7, 5.9). Since engineering constants are used to define the elastic properties of GFRP, the elastic modulus is interpolated based on temperatures for the other two directions from [32]. The elastic properties of the bonding agent was also measured by the DMA experiment and found in figure 5.8. Since the CZM for the Redux® 677 is yet to be developed and hence the CZM already available for the structural adhesive BM1480 [24]

Table 5.9: Mechanical properties of components of hybrid plate [29, 30, 31]

Material	Young's modulus [MPa]	Poisson ratio [-]	Thermal expansion coefficient [ $\text{K}^{-1}$ ]
Steel	210000	0.3	$1.3\text{e}^{-5}$
Support plate	210000	0.3	$1.3\text{e}^{-5}$
Wood	10000	0.4	-

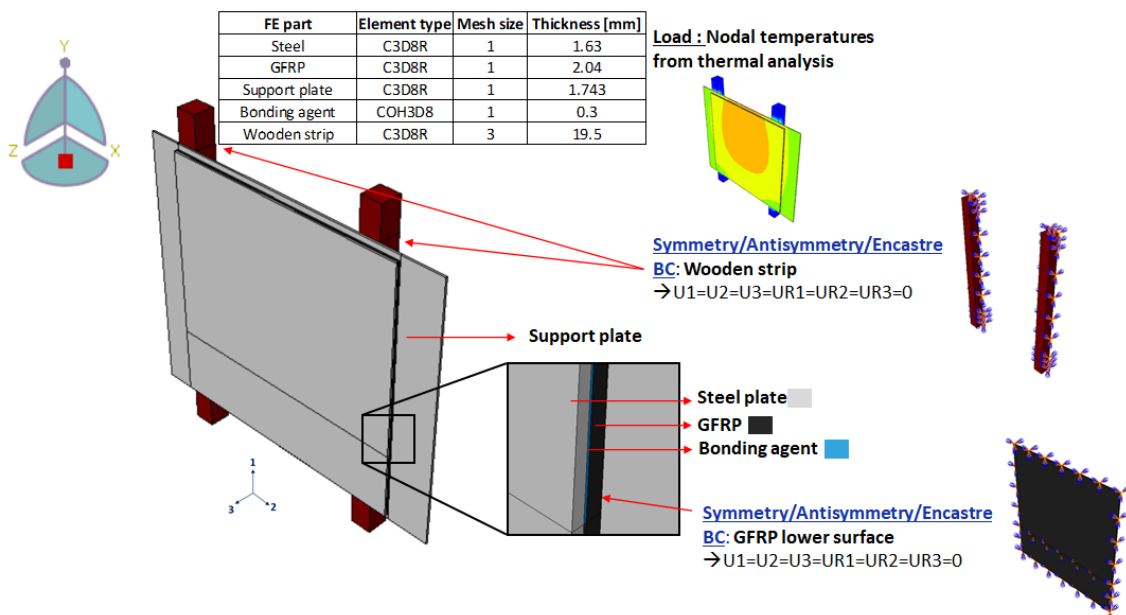


Figure 5.12: Process simulation mechanical analysis FE model

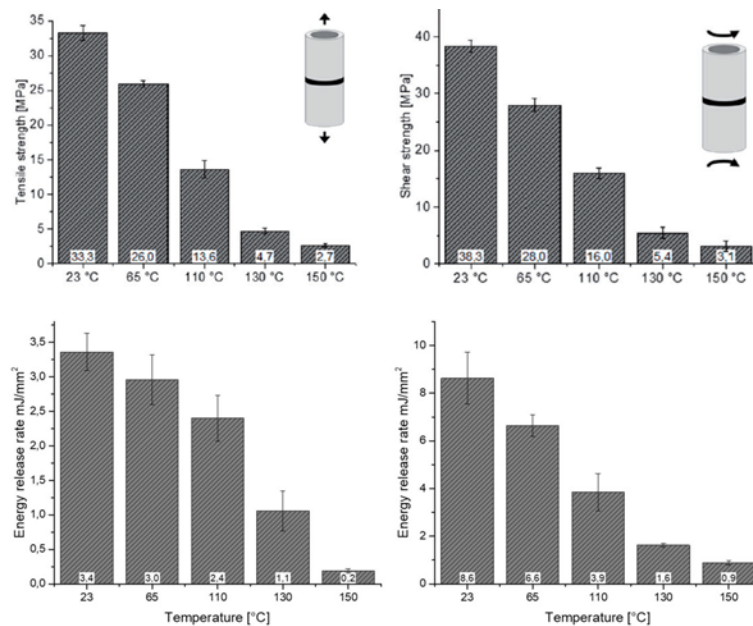


Figure 5.13: Tensile, shear and energy release rates used for the bonding agent [24]

shown in figure 5.13 is used for predicting the adhesive damage. The thermal expansion coefficients for the bonding agent is accessed from literature [28] is summarized in the table 5.10.

Table 5.10: Thermal expansion coefficients used for Redux® 677 [28]

<b>Thermal expansion coefficient</b> $[10^{-4}K^{-1}]$	<b>Temperature</b> $[^{\circ}C]$
2.28	23
3	115
3.65	160
4	180

The mechanical analysis results are based on the different thermal expansion coefficients of GFRP with wooden strip and GFRP lower surface fixed to evaluate the adhesive stresses and deflections of the joining partners. Since the results of this subsection is of predominant importance, they are discussed in the results chapter in section 7.0.1.

## 5.1.4 Process validation simulation

### Thermal analysis

The process validation simulation is done to compare the experimental results from the performed validation experiment (refer section 4.2.4). The validation is also done in two stages namely the heat transfer analysis initially followed by the mechanical analysis. The FE model which was used for the heat transfer analysis is displayed in the figure 5.14. An initial predefined temperature field of about 150 °C is applied to all the components except the wooden strips. Then it is allowed to cool based on the validated film coefficients (refer tables 5.2, 5.4, 5.7) to the room temperature of 25 °C. The thermal properties used for the steel, support plate, gfrp, bonding agent are provided in the previous sections (refer tables 5.1, 5.3, 5.5, 5.6). All the components were connected to each other by means of \*TIE connection. The temperatures were measured at two different points namely T1 on the interface between bonding agent and GFRP and other on the support plate exactly at the respective nodes same as the experiment. The cooling curves obtained from the two points are compared against the experimental results and shown in figure 5.15. As it is expected, the temperature T2 must cool down faster than the temperature T1 at the interface zone. This was due to the reason that the support plate with kapton tape cools quickly than the GFRP which is conducting heat from both the steel and support plate. It was found that towards the end of the simulation, the cooling happened quickly than the experimental trials. This will be also due to the reason that for the experimental attempts, mostly after reaching down to 40 °C, it is stopped as it was

time consuming to measure the further cooling process. But since after this temperature the displacements will be almost constant, it is not so important to correlate the experimental trials with the simulation results. The nodal temperatures are to be transferred now for the mechanical analysis.

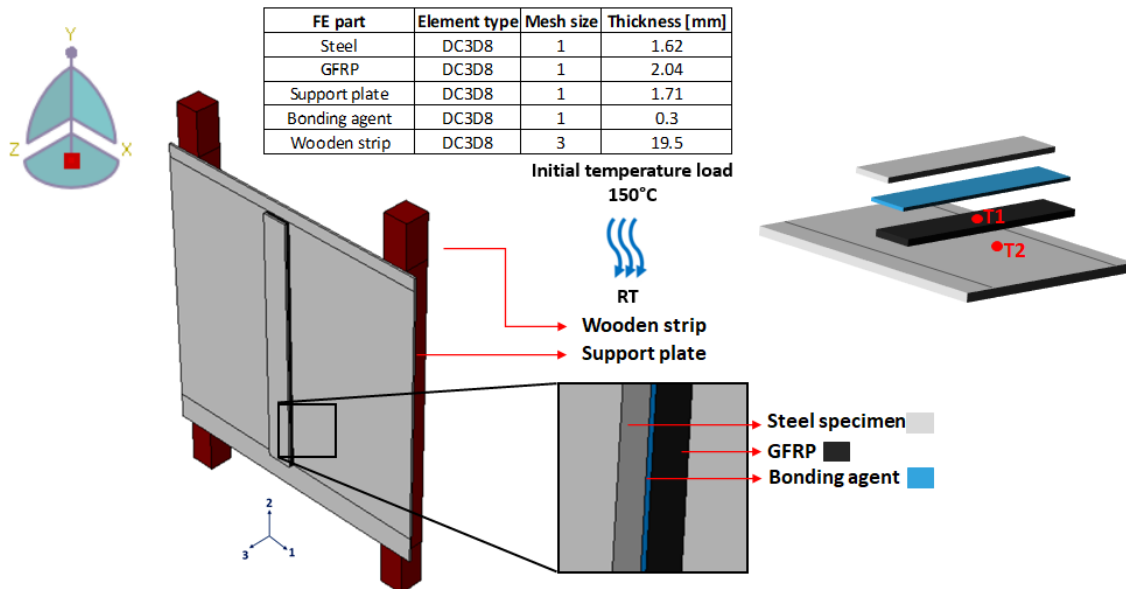


Figure 5.14: Process simulation validation thermal analysis FE model

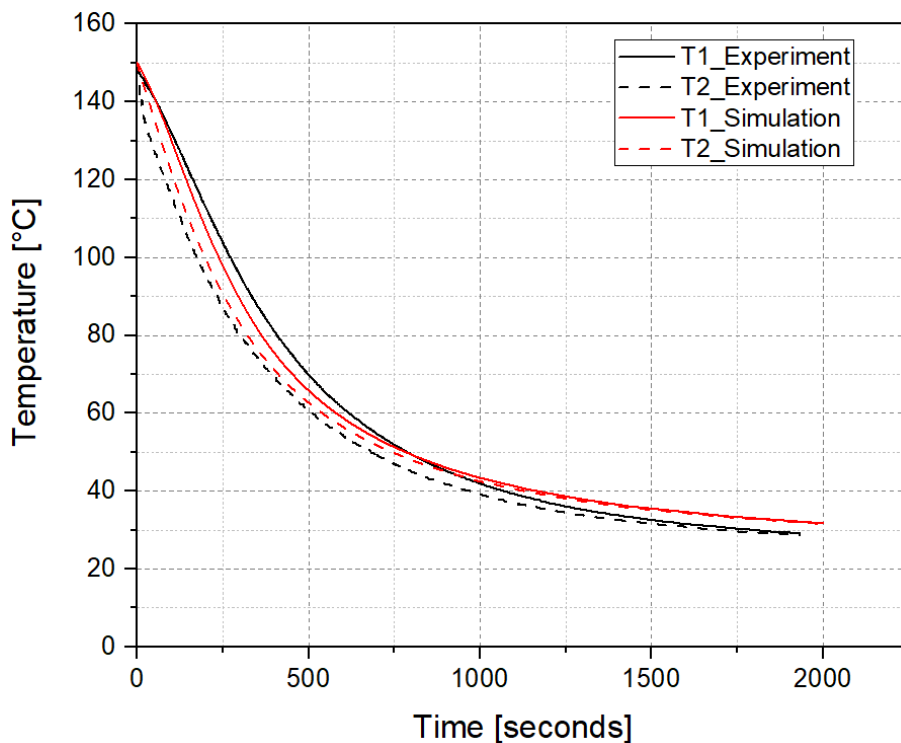


Figure 5.15: Cooling curves of the process validation simulation

## Mechanical analysis

The mechanical analysis FE model was also built in the same way as discussed in the preceding section 5.1.3. The FE model presented in the figure 5.16 is created from the exact dimensions of the experiment (in section 4.2.4). The mechanical properties which are required for the simulation are employed according to the tables 5.9,5.10 and figures 5.7, 5.8, 5.9, 5.13. Since the simulation strategy is almost similar to the mechanical process simulation it is not elaborated further and the results will be contemplated in chapter 7.

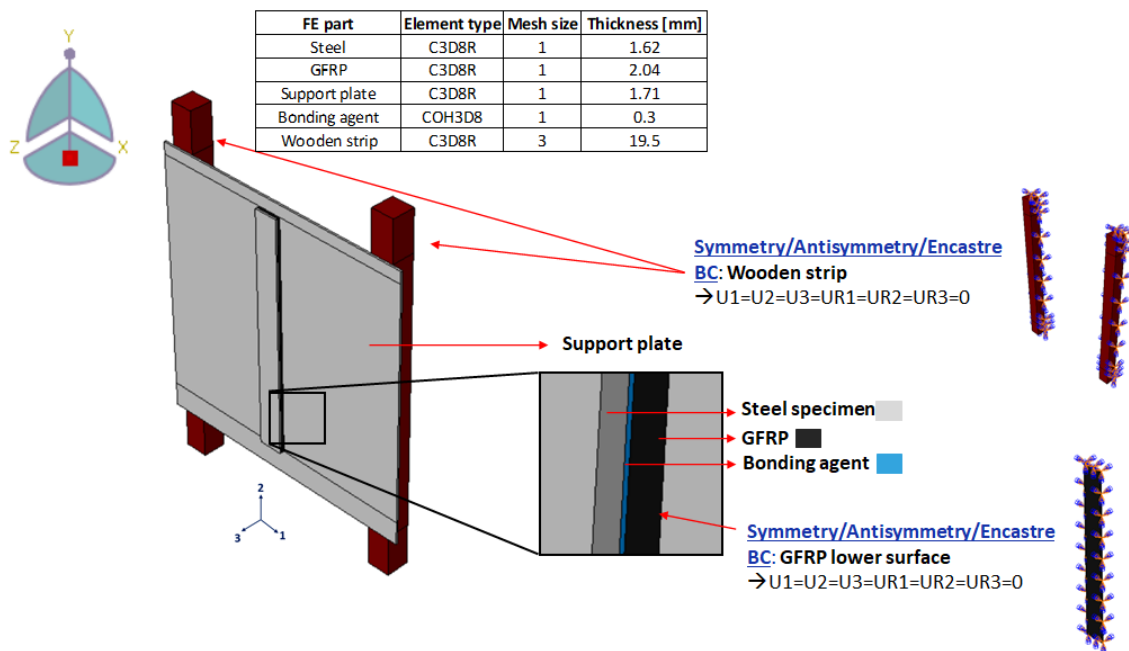


Figure 5.16: Process simulation validation mechanical analysis FE model

## 5.2 Structural

### 5.2.1 Simulation strategy

The simulation strategy is based on the software capabilities of ABAQUS™. The strategies which had been used in the previous investigations were discussed in the section 2.3.2. ABAQUS™/Standard is chosen in this work where static,general procedure is used and the damage modelling is not considered. The parts were modelled in 3D space and the \*TIE connection is used for the connection between the joining partners and bonding agent. The element types such as the C3D8R (An 8-node linearbrick, reduced integration, hourglass control) is used for the rigid bodies, C3D20R (A 20-node quadratic brick, reduced integration) for the steel, GFRP adherends and COH3D8 (An 8-node three-dimensional cohesive element) for the bonding agent. The steel and GFRP adherends had the element types which pre-

dicts the bending problems meticulously [76]. In the following section, the material model is calibrated for the individual components of the hybrid 3-point-bend specimens so as to apply for the final hybrid specimen simulation.

### 5.2.2 Material model buildup

The individual components of the 3PB hybrid specimen are Steel, GFRP and bonding agent. Initially the plasticity properties of the steel specimen are evaluated followed by the elastic properties of the GFRP specimen. Then sensitivity analysis had been performed on various parameters to look deeply which influences the elasticity of the fiber reinforced polymer material. Finally the above specified calibrated properties will be used in the simulation.

#### Steel material model

To substantiate the elastic and plastic material properties of the DP980 steel, the yield curve must be fitted foremost to have a perfect foresee over the pliable nature of the material during bending. Therefore, to fit the yield curve , a set of DP980 steel specimens were subject to tensile loading. Then the yielding properties was adapted based on the Swift-voce law. The yield curve which is fitted properly using this relation over the tensile test stress-strain curves is displayed in the figure 5.17.

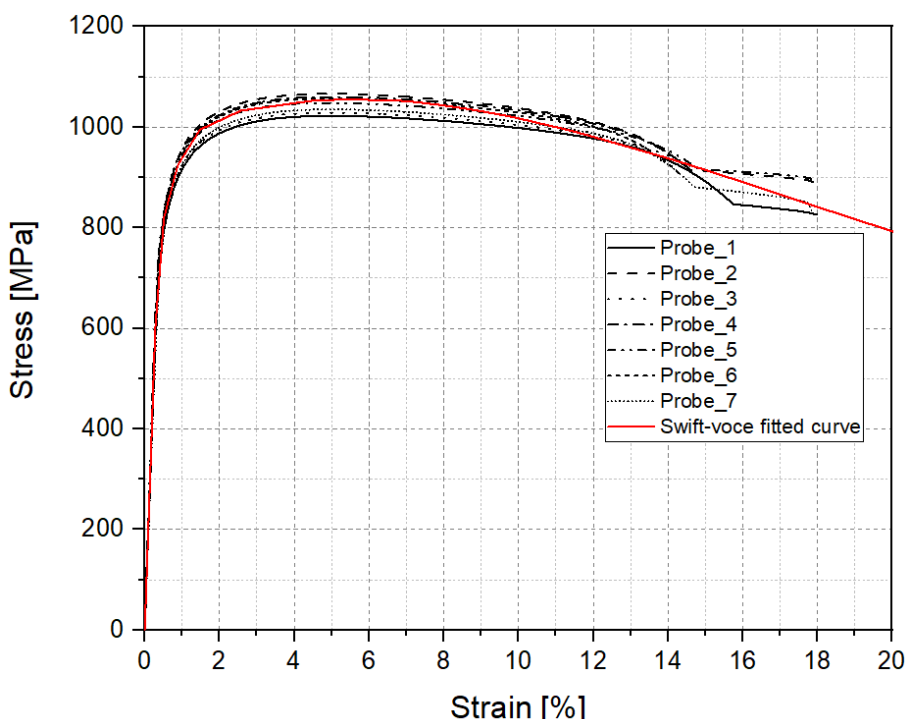


Figure 5.17: Plasticity data legitimized by Swift-voce relation Vs Tensile tests of DP980

Since the fitting procedure was not part of this work, it is not briefed. The elastic property of the DP980 Steel (refer table 5.9) and the plastic strain curve adapted will be used in the simulation to validate the experimental results (refer section 4.3.1). The 3-point-bending FE model is illustrated in the figure 5.18.

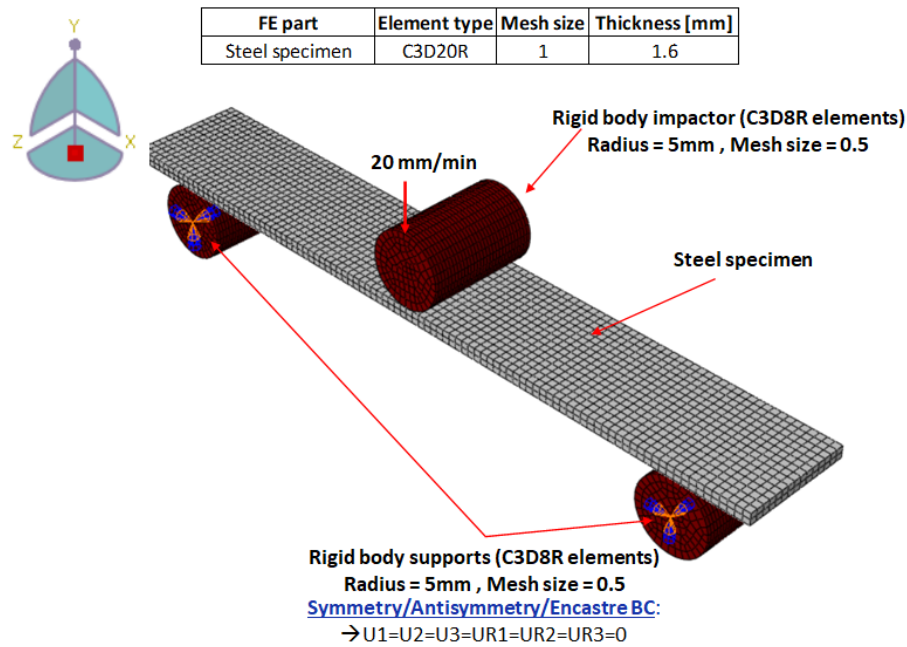


Figure 5.18: Steel specimen bending simulation FE model

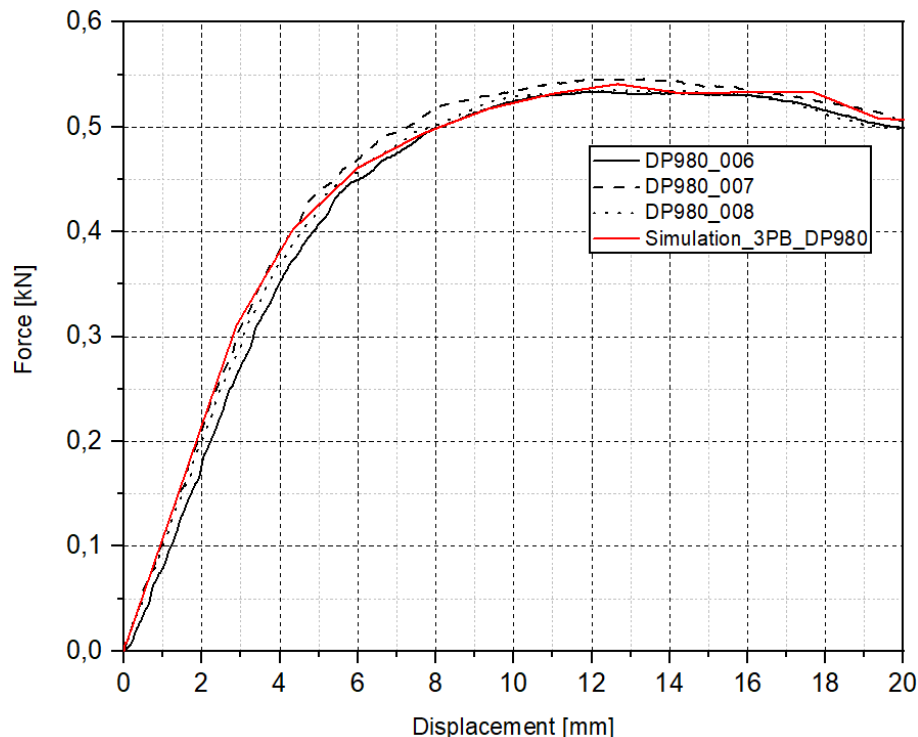


Figure 5.19: Force-Displacement curves of 3PB simulation of Steel

The steel specimens from 1 to 5 were not considered as it did not undergo the hardening process (refer section 4.3.1). The dimensions of the FE model was taken from three specimens (6 to 8) subjected to hardening process. The steel specimen was meshed with C3D20R elements with 2 elements through the thickness. The accuracy of the element type subjected to bending has a good correlation value of 1.001 with the basis normalized tip deflection results of a cantilever beam [76]. The interaction between the impactor and the surface of steel specimen was defined by the penalty friction formulation with a friction coefficient of 0.25. The tangential behavior between the supports and the steel was defined again by the same formulation with a friction coefficient of 0.15. The normal behavior between the impactor, supports and the steel specimen was defined by the hard contact. The model was simulated for about 60 seconds same as the experiment. A reference point was created in the impactor to measure the applied force and displacement at every step. The force-displacement simulation curve depicted in figure 5.19 is compared against the experimental curves where it is found that from the onset of plasticity region the simulation results finds a good equivalence. So the employed elastic and plastic properties of the steel material are validated and it could be used for the steel part of hybrid specimen final simulation.

### GFRP material model

The GFRP bending simulation model developed to validate the experimental results from section 4.3.2 is illustrated in the figure 5.20. The model shown in the image is the final configuration of the simulation. Heretofore, a sensitivity analysis had been

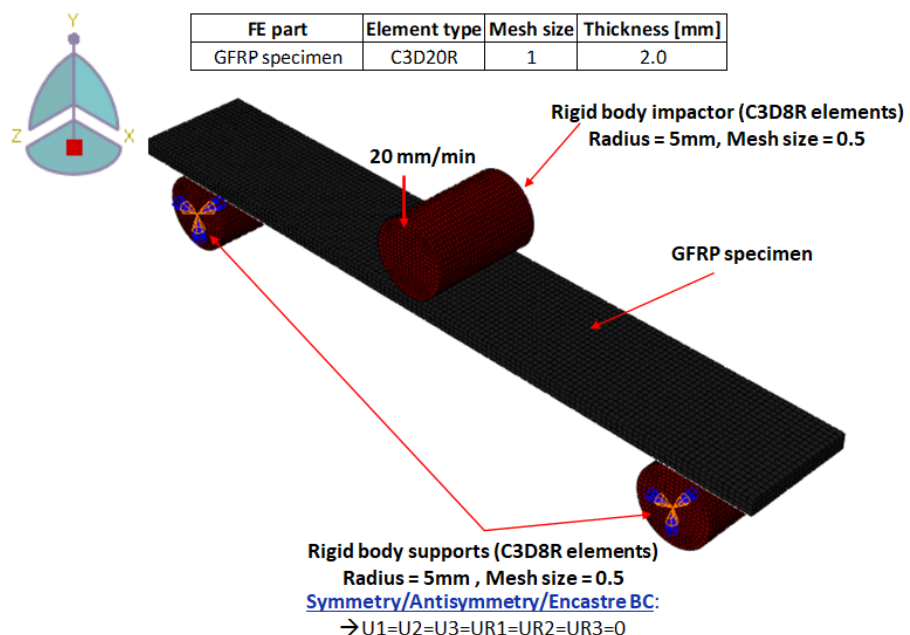


Figure 5.20: GFRP specimen bending simulation FE model

carried out to have a look into the parameters which influences the simulation. The parameters considered in the sensitivity analysis were elastic modulus, thickness, friction coefficient, element size and type of element used in meshing. To commence with, the elastic properties of the laminate obtained from the experiment [32] is summarized in table 5.11.

Table 5.11: Elastic properties of GFRP [32]

<b>Properties</b>	<b>Values</b> <b>[Unit]</b>	
<b>Velocity →</b>	<b>2 mm/min</b>	<b>1 mm/min</b>
$E_{11}$	21025.08 [MPa]	21898.68 [MPa]
$E_{22} = E_{33}$	21144.73 [MPa]	19381.26 [MPa]
$\nu_{12} = \nu_{13}$	0.14	0.11
$\nu_{21} = \nu_{31}$	0.16	0.15
$\nu_{23}$	0.23	0.23
$G_{12} = G_{13}$	1875.86 [MPa]	1689.10 [MPa]
$G_{21} = G_{31}$	1875.86 [MPa]	1689.10 [MPa]
$G_{23} = E_{22}/2(1+\nu_{23})$	8595.42 [MPa]	7878.56 [MPa]

It was decided to use the average of the elastic properties since it was unsure about to select which velocity dependent parameters. The properties which are used for the GFRP material for the sensitivity analysis are listed in the table below 5.12.

Table 5.12: GFRP properties used in simulation[32]

<b>Properties</b>	<b>Values</b> <b>[Unit]</b>
$E_{11}$	20262.99 [MPa]
$E_{22} = E_{33}$	20262.99 [MPa]
$\nu_{12} = \nu_{13}$	0.12
$\nu_{21} = \nu_{31}$	0.15
$\nu_{23}$	0.23
$G_{12} = G_{13}$	1782.42 [MPa]
$G_{21} = G_{31}$	1782.42 [MPa]
$G_{23} = E_{22}/2(1+\nu_{23})$	8236.99 [MPa]

Initially the parameters such as the thickness and the friction coefficient were differed by nominal values to check the influence. The elastic properties summarized in the table 5.12 is used. To start with, the maximum (2.04 mm) and the minimum **thickness** (1.97 mm) from the experiments (refer table 4.2) was used for the gfrp specimen. The friction coefficient of 0.3 for both the supports and impactor, element type C3D20R and global element size of 0.75 was used for the simulation. Secondly keeping the thickness value (1.97 mm) as constant, the **friction coefficient** was varied from 0.25 to 0.35, element type C3D20R, global element size of 0.75 to check

the effect of friction coefficient on the simulation. The results from the simulation are displayed in the figure 5.21.

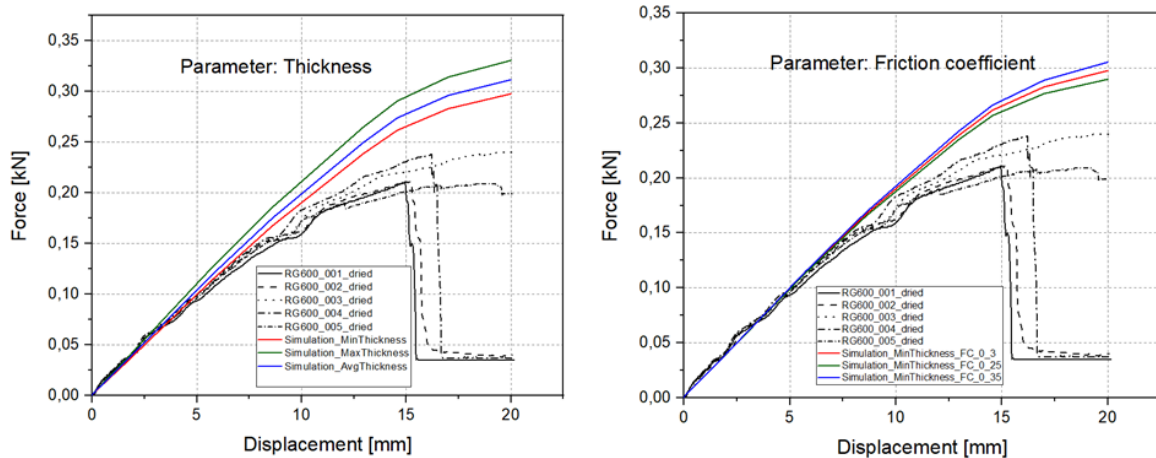


Figure 5.21: Sensitivity analysis of parameters thickness and friction coefficient

It was found that increasing the thickness plays an important role in increasing the force required but the friction coefficient did not have significant difference if it is varied. So, it was decided to use the friction coefficient of 0.3 for the subsequent simulations. Thirdly, the **elastic modulus** of the GFRP was increased and decreased by 10% from the average value to check its influence over the simulation. The values of the elastic modulus were average value of 20262.99 MPa, maximum value of 22289.28 MPa and minimum value of 18236.69 MPa used in the simulation. A friction coefficient of 0.3 for both the supports and impactor, element type C3D20R and global element size of 0.75 was used for this elastic modulus parameter. Finally the **element size** was varied such as 0.5, 0.75 and 0.825 with the average elastic modulus, minimum thickness value, friction coefficient of 0.3 for both the supports and impactor, element type C3D20R. The sensitivity of the above two parameters are shown in the figure 5.22. It was found that the element size did not have significance over the simulation whereas if the elastic modulus is increased by 10% from the average elastic modulus value, the force increases by about 22% which is bit high. Subsequently of the four parameters which were analyzed, the **thickness** and the **elastic modulus** played a major role in the 3-point-bending simulation of GFRP specimen. The sensitivity analysis was done to check the influence of these parameters and also to check if the elastic modulus of the GFRP material can be increased or decreased to obtain a good fit over the experimental attempts. But finally it was decided only to use the average properties listed in table 5.12 for the GFRP specimen simulation. The simulation result is presented in the figure 5.23. It is found that till a displacement of 5 mm, the simulation results correlates better with the experimental results. After that, since the damage modelling is not employed in the material model, the simulation results slightly differs from the experimental curves.

But the material model which is used in the simulation is considerable to be used for the final 3-point-bending simulation of hybrid specimen.

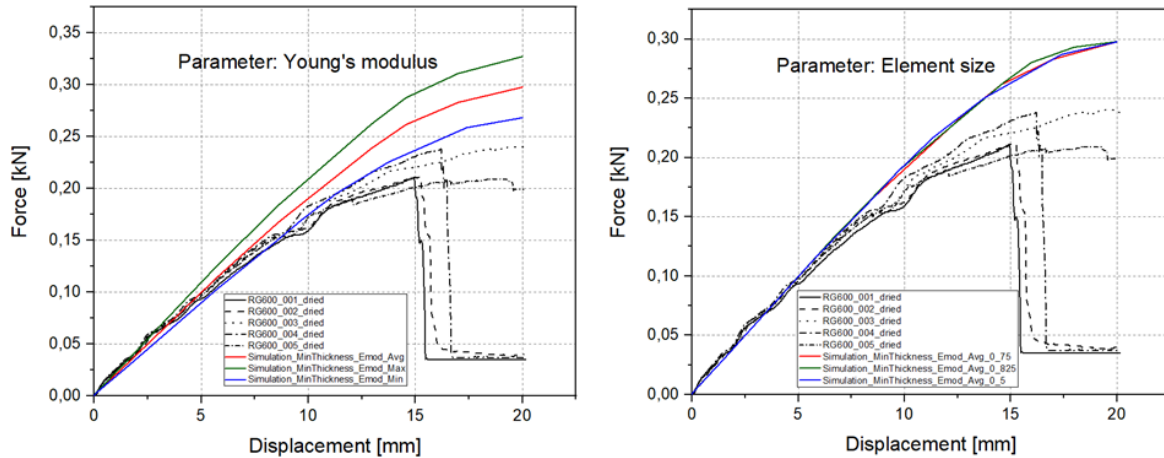


Figure 5.22: Sensitivity analysis of parameters elastic modulus and element size

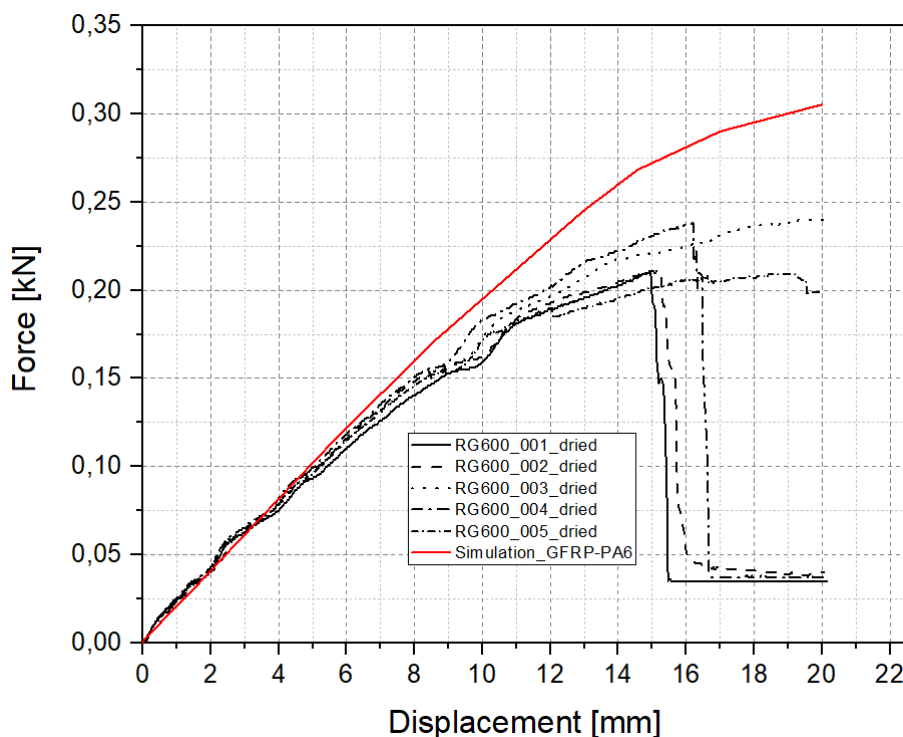


Figure 5.23: Force-Displacement curves of 3PB simulation of GFRP

### Bonding agent material model

The bonding agent material properties such as the elastic modulus was referenced from the material datasheet of Redux® 677. The temperature dependent CZM is yet to be developed and hence the properties listed in table 5.13 are to be used for the final 3-point-bending simulation of hybrid specimen.

Table 5.13: Material parameters used for Redux® 677 [33]

Tension			Shear		
Modulus [MPa]	Strength [MPa]	Energy [mJ/mm <sup>2</sup> ]	Modulus [MPa]	Strength [MPa]	Energy [mJ/mm <sup>2</sup> ]
2500	50	1.5	860	50	1.5

### 5.2.3 Hybrid specimen validation simulation

The hybrid specimen FE model is illustrated in the figure 5.24. The model is created exactly on the same procedure in which the Steel and GFRP versions were created (refer sections 5.2.2, 5.2.2). The mechanical properties which are required for the 3-point-bending simulation are from (**Steel** - table 5.9 & figure 5.17), **GFRP** - table 5.12 and **Bonding agent** - table 5.13).

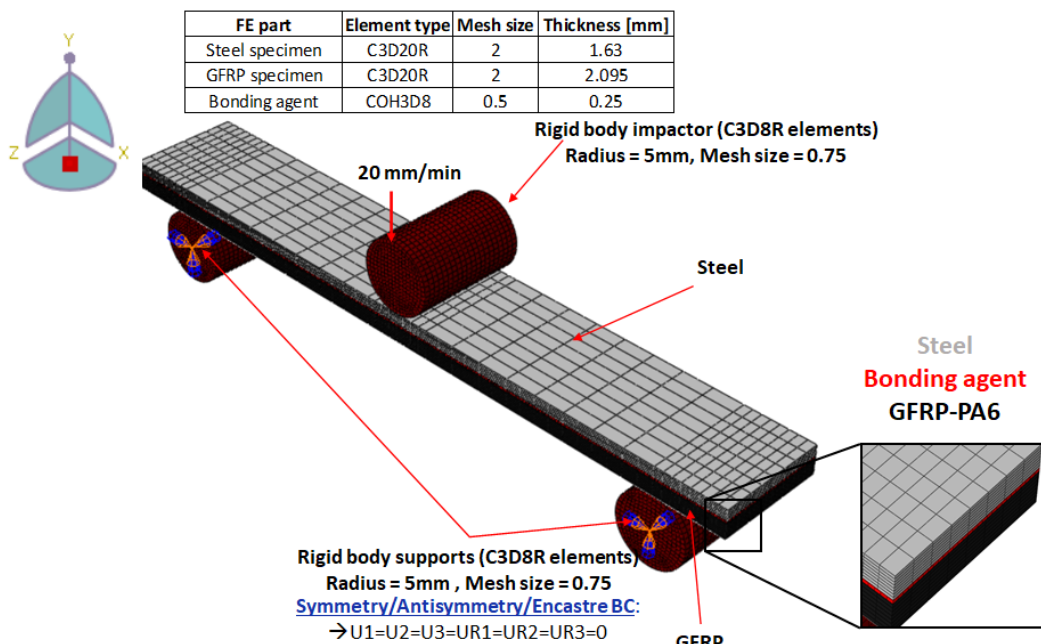


Figure 5.24: Hybrid specimen bending simulation FE model

To measure the thickness of the bonding agent, microsection of the hybrid specimen had been made. The thickness was found to be 0.25 mm which was applied in the simulation model. Also, the average thickness of the hybrid specimens was calculated (from table 4.4) so that the thickness of the GFRP was decided to be 2.095 mm since the steel thickness was 1.63 mm. The interaction between the impactor and the steel part was defined by the surface-to-surface contact with a friction coefficient of 0.25 and between the supports and the GFRP with a friction coefficient of 0.3 . A velocity boundary condition was applied in the y-direction of magnitude 0.333333 mm/s which is equivalent to the speed of 20 mm/min in the experiment. The supports at the bottom were fixed to enable the bending movement at the centre of the

hybrid specimen span. The force-displacement curve obtained is plotted against the experimental curves (refer section 4.3.3) and shown in the figure 5.25.

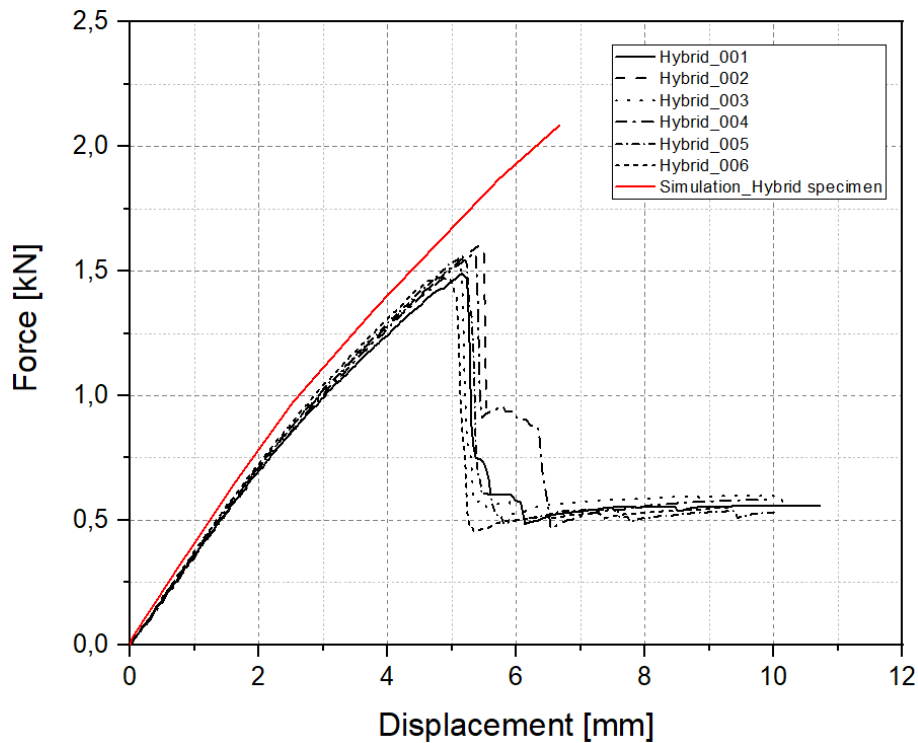


Figure 5.25: Force-Displacement curves of 3PB simulation of Hybrid specimen

It was found that initially till a displacement of 3 mm, the simulation results almost finds a good correspondence with the experimental results. But after 3 mm, due to the some internal plasticity effects of the GFRP which is not taken into account in the material model, the results cannot replicate this behavior. Also there were some defects after the production of hybrid plates explained in section 4.3.3. These were not included in the material model for either the individual GFRP flexural tests or the hybrid specimen bending tests. This is also another reason that the simulation cannot predict so accurately the mechanical test results. If the damage parameters of the GFRP is included in the material model, even a closer correspondence can be found with the experimental results.

The simulation comparison for the process and the mechanical 3-point-bending tests were carried out and in the next step the potential analysis of the car model will be done to evaluate the crash performance and the incorporation of hybrid parts into it so that the devised process simulation can be transferred to analyze the damage within the bonding agent.

# 6 Potential of hybrid components in Toyota Camry

In this chapter, the potential analysis of the different components of the Toyota Camry model is contemplated. The process simulation method which is finalized in the preceding chapter will be transferred to the critical components is also deliberated.

## 6.1 Analysis of different components in Camry

The Toyota Camry model was subjected to different crash load cases such as the Offset deformable barrier (ODB), Small overlap(SOL), Pole, Insurance institute for highway safety (IIHS)-Barrier. Initially the components were filtered out on basis of criterion such as the thickness, weight and energy absorption capability. Of that, finally 14 components made it for the final analysis of evaluating about the plasticity changes, intrusions and spot weld, adhesive, material failure if the thickness is reduced by about 20% and comparing it to the basis versions. The components which were finally evaluated is displayed in the figure 6.1.

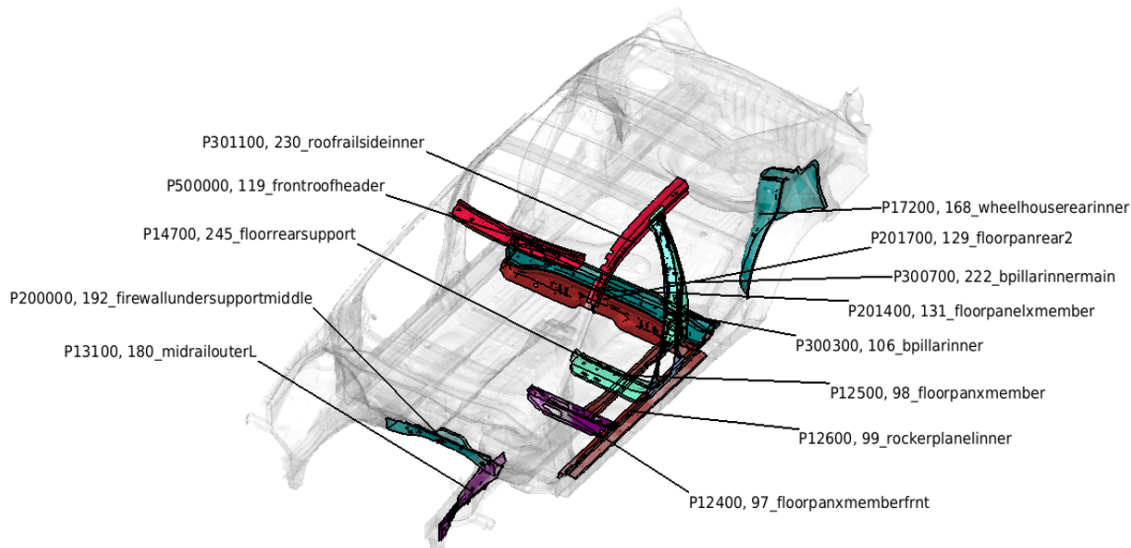


Figure 6.1: Components analyzed in Toyota Camry

To explain the idea behind this a bit more clearly, the figure 6.1 represents the basis version for which the crash simulation will be executed. Further, a variant V076 will be created for instance, the firewallundersupportmiddle's thickness reduced by 20% and the crash simulation will be performed. Then both the basis as well as the variant V076 results will be compared against each other to check the criticality of the component in terms of plasticity, intrusion and other failures. Likewise, 14 variants were

created and compared against the basis versions to sort the components which are to be patched based on priority (refer table 6.4). The priority 1 components alone are conferred below because of patching the FRP material to these critical components and conducting the process simulation for the same. The critical variants V064, V065 and V068 analyzed by the Pole and SOL load cases respectively are reviewed in the following subsections.

### 6.1.1 V064 - Floorpanxmemberfrnt

The front seat cross members represented in the figure 6.2 in which the thickness of the component ID 12400 is reduced by 20% as summarized in the table 6.1. Even though various characteristics such as the plasticity was analyzed for the component ID 103600, it did not have much impact after the crash. Hence, the component ID 12400 which is closer to the impact site will be discussed.

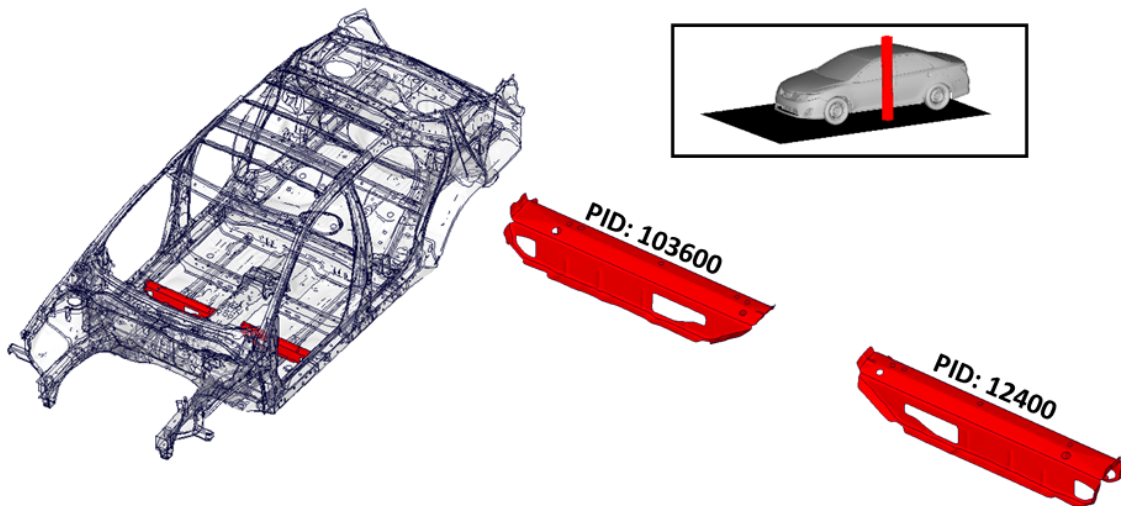


Figure 6.2: Front seat cross members in Toyota Camry

Table 6.1: Component characteristics comparison between basis and V064

Version	PID name	Mass [kg]	Thickness [mm]
Basis	Floorpanxmemberfrnt	1.38	1.4
V064	Floorpanxmemberfrnt	1.1	1.12

The various features such as the plasticity (6.3), intrusion (6.4), spot weld failure (6.5), adhesive failure (6.6) and material failure (6.7) are analysed for the variant V064. It was found that the plasticity increased to a higher level in the regions near the impact when compared to the basis version. It increased by about 43.5% after the thickness was reduced by 20%. The overall displacement increased by 12% and

visualised the increase in displacement in region of front seat cross member. In the case of spot weld failure, it remained almost the same compared to the basis version where 2 to 5 spotwelds in the marked region in (figure 6.5) failed. But this can be considered to be on the same level. Secondly, the adhesive failure also remained the same. The material failure increased a bit in the region of the floor front but it can

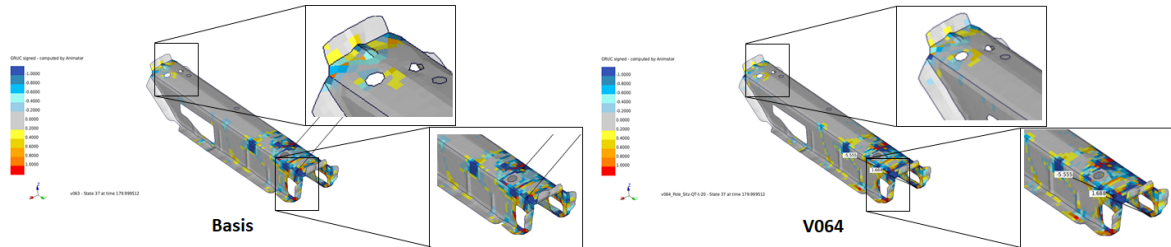


Figure 6.3: Plasticity comparison between basis and V064

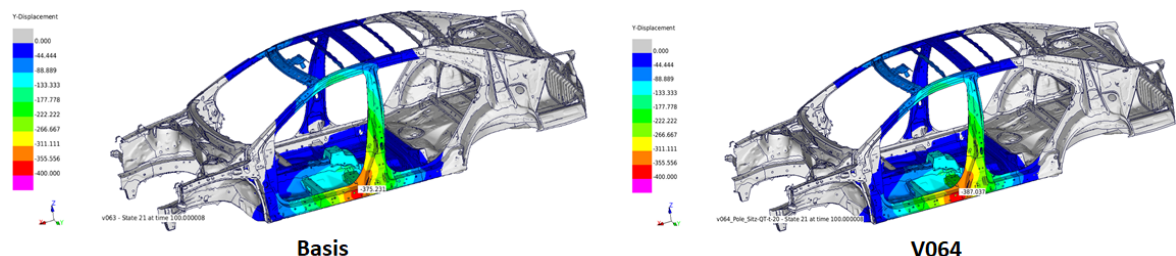


Figure 6.4: Intrusion comparison between basis and V064



Figure 6.5: Spot weld failure comparison between basis and V064

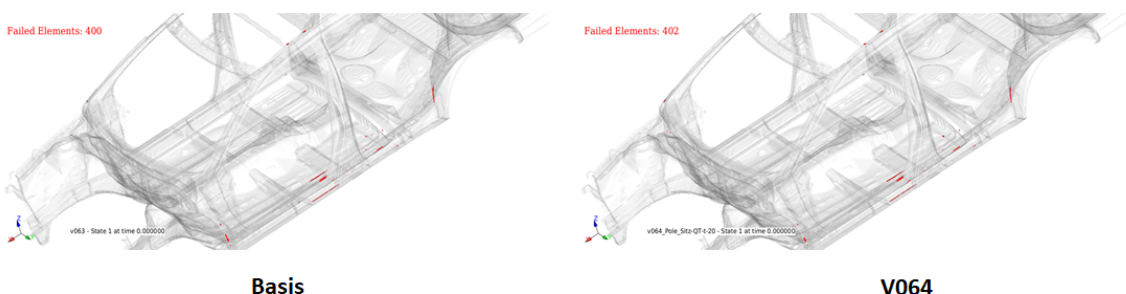


Figure 6.6: Adhesive failure comparison between basis and V064

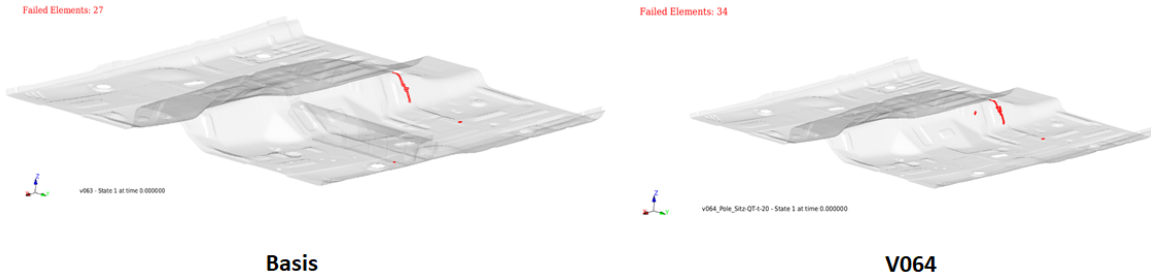


Figure 6.7: Material failure comparison between basis and V064

be considered to be on the same level. All these aspects combined together made it a better variant than the others to be chosen for the patching process.

### 6.1.2 V065 - Floorpanxmember

The second important components were the rear seat cross members in which for the component ID 12500, the thickness was reduced by 20% (table 6.2) and crash simulation was performed. Alike the front seat cross members, the component ID 103700 was excluded from evaluation as it was not so important to analyze.

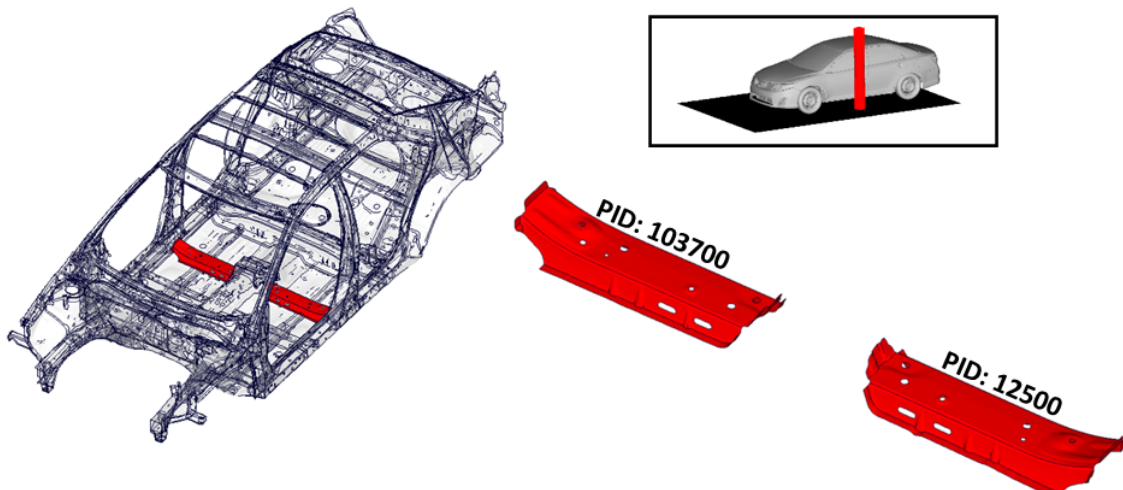


Figure 6.8: Rear seat cross members in Toyota Camry

Table 6.2: Component characteristics comparison between basis and V065

<b>Version</b>	<b>PID name</b>	<b>Mass [kg]</b>	<b>Thickness [mm]</b>
Basis	Floorpanxmember	2.09	2.0
V065	Floorpanxmember	1.67	1.6

The features such as the plasticity (6.9), intrusion (6.10), spot weld failure (6.11), adhesive failure (6.12) and material failure (6.13) are analysed for the variant V065.

It was seen that the plasticity increased by about 11% and few elements of the rear seat cross member attached to the rocker panel inner had already reached the maximum limit. The overall displacement increased by about 18 mm and subsequently a slight increase in the intrusion was found in areas of rocker panel and B-pillar.

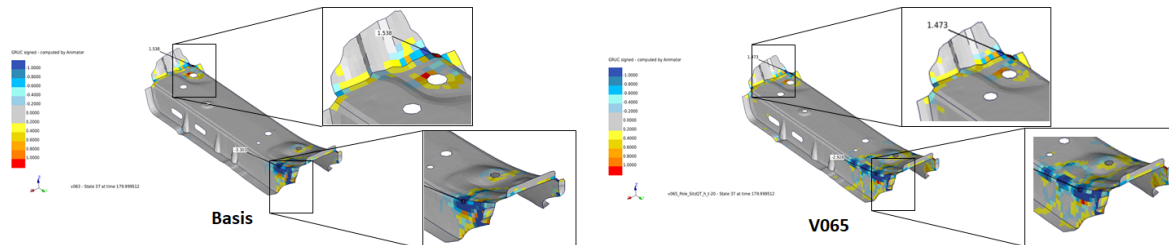


Figure 6.9: Plasticity comparison between basis and V065

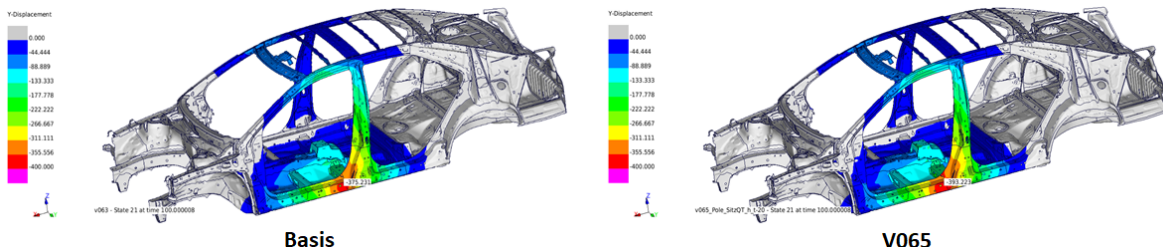


Figure 6.10: Intrusion comparison between basis and V065



Figure 6.11: Spot weld failure comparison between basis and V065

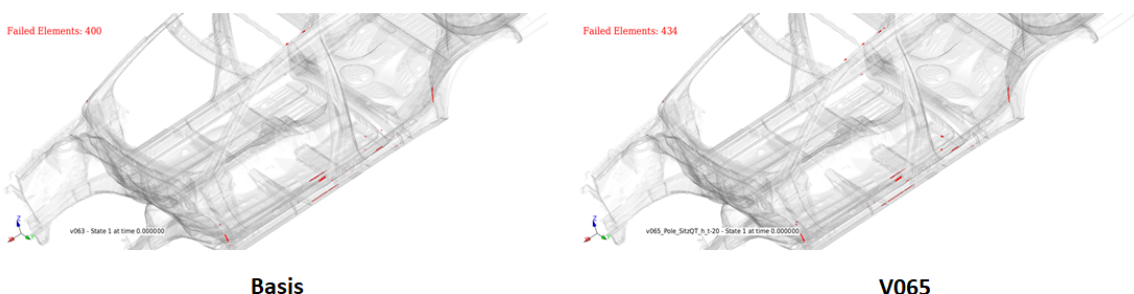


Figure 6.12: Adhesive failure comparison between basis and V065



Figure 6.13: Material failure comparison between basis and V065

The overall spot weld failure remained on the same level whereas in the region where the thickness was reduced, there was an increase in load transfer to the tunnel front and front seat cross member which leads to slight increase in spot weld failure. The overall adhesive elements failure had increased but in the floor front regions it remains on the same level. In case of material failure, since the failure of spot weld in front seat cross member and rocker inner front few elements had failed but this can be considered to be on the same level.

### 6.1.3 V068 - Midrailouter

The third important component was the mid outer rail in which for the component ID 13100, the thickness was reduced by 20% (table 6.3) and crash simulation was performed. The crash simulation was carried out with the SOL load case and the results were analyzed.

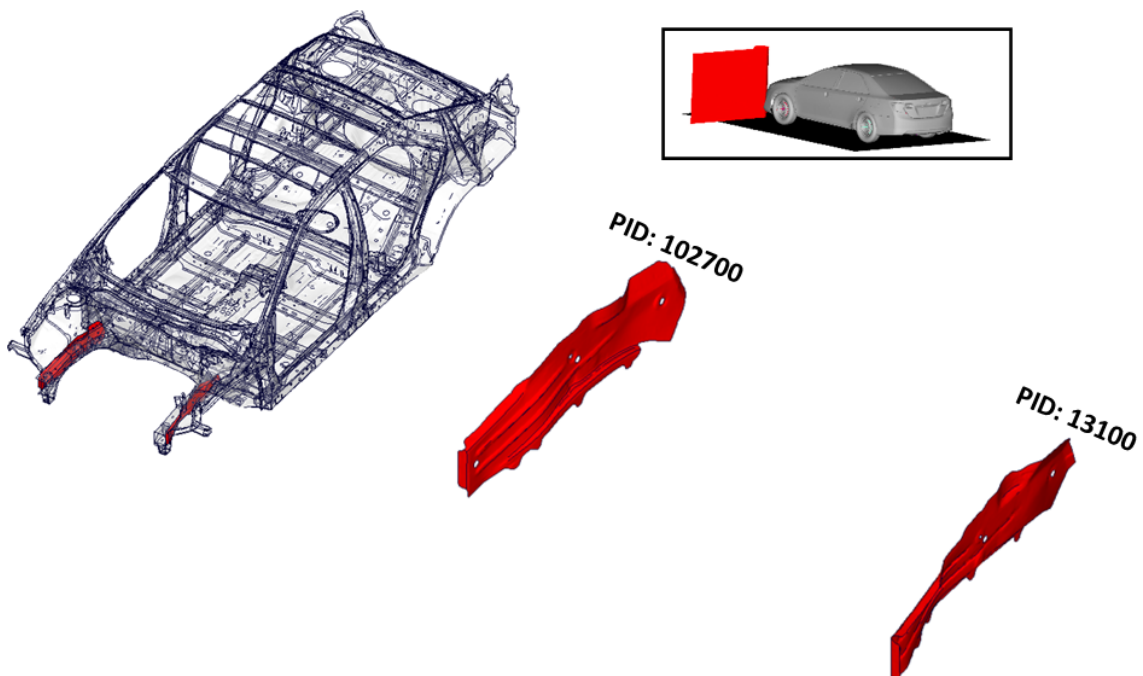


Figure 6.14: Mid rail outer component in Toyota Camry

Table 6.3: Component characteristics comparison between basis and V068

Version	PID name	Mass [kg]	Thickness [mm]
Basis	Floorpanxmember	2.09	2.0
V068	Floorpanxmember	1.67	1.6

The features such as the plasticity (6.15), intrusion (6.16), spot weld failure (6.17), adhesive failure (6.18) and material failure (6.19) are analysed for the variant V068.

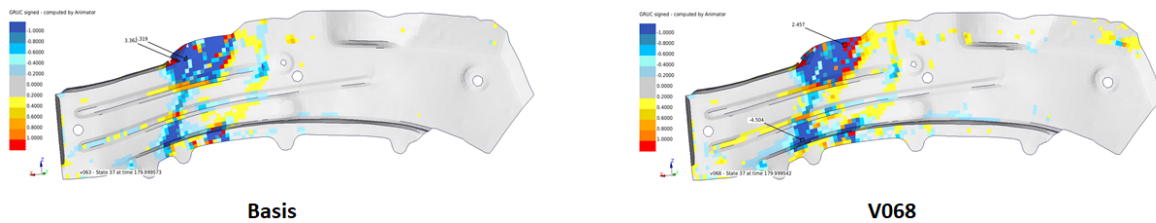


Figure 6.15: Plasticity comparison between basis and V068

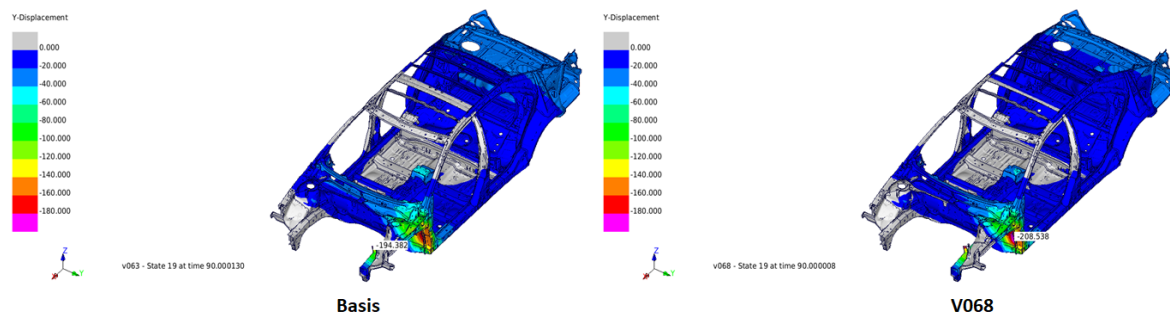


Figure 6.16: Intrusion comparison between basis and V068

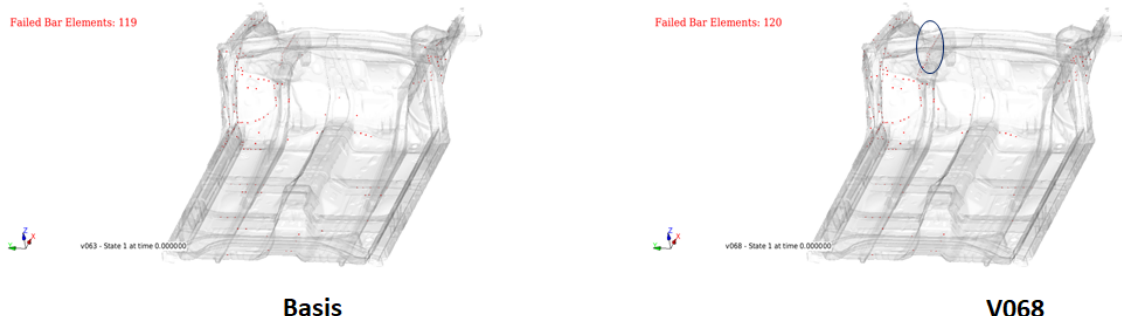


Figure 6.17: Spot weld failure comparison between basis and V068

The plasticity had increased drastically where many elements had already reached the maximum limit. The displacement increased by about 14 mm and the intrusion in the firewall is bit high compared to the basis version. The overall spot weld failure count remained the same but in regions of mid outer rail the spot weld failure

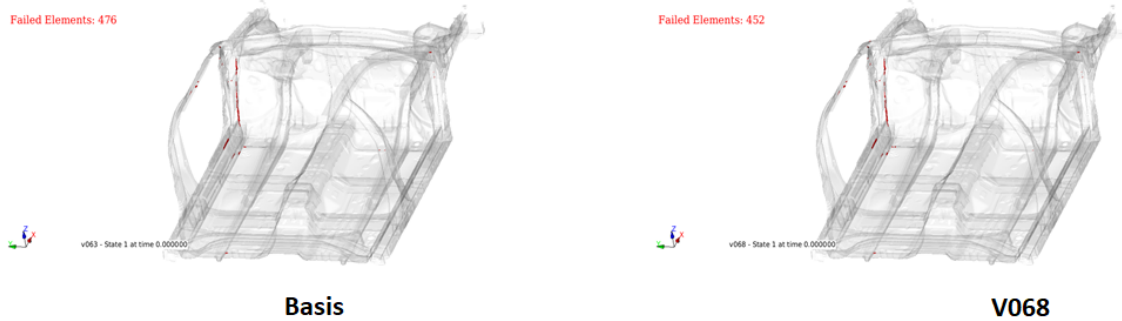


Figure 6.18: Adhesive failure comparison between basis and V068

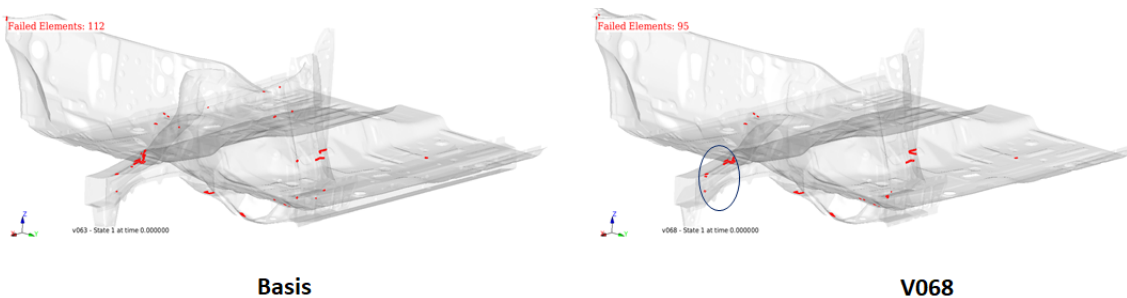


Figure 6.19: Material failure comparison between basis and V068

had increased. The overall adhesive failure count had decreased and in the case of material failure overall count had decreased. But in the region where the thickness was reduced, the element failure occurred in mid outer rail region where the plasticity had already crossed the maximum limit. Thus, the list of components with priority 1 had been analysed for various aspects. Likewise for the remaining 11 variants, the aforementioned features were analysed and evaluated the increase in spot weld failure, adhesive failure, material failure and whether the intrusion and plasticity had decreased and if the thickness of the component was reduced how much weight reduction could be obtained and so on. Based on these aspects the components were prioritized and the final list with the variants is shown in table 6.4. There was one exception about the variant V073. Although it was evaluated but the door front interior mid bracket does not belong to the BIW and hence it was ignored.

In the subsequent section, the variant V065 is chosen for the process of patching the component. This was done to analyze whether the patched component proves the potential of reducing the weight which is the ultimate motive without compromising the crash performance of the Toyota Camry model. If the patched component proves to be promising with the results, then the component will be subjected to the process simulation method which already had been devised. The purpose of this is to evaluate the damage in the adhesive layer which could happen as a result of the manufacturing the component in the industry.

Table 6.4: Critical components prioritized based on potential analysis

PID	Relevant load case	Variant	Name	Mass reduction [kg]	Original thickness [mm]	Variant thickness [mm]	Plastification	Intrusion [mm]	Spot weld failure [Spotweld count]	Adhesive failure [Adhesive count]	Material failure [Elements]	Suggestion	Priority
12400	POLE	V064	97_floormanxmemberfrnt	0.28	1.4	1.12	High	+12	+1	+2	+7	Yes	1
12500	POLE	V065	98_floormanxmember	0.42	2	1.6	High	+18	-4	-2	-5	Yes	1
12600	POLE	V066	99_rockerpantelinner	0.74	1.4	1.16	High	-4	-10	+69	-5	Yes	1.5
201400	Barriere	V078	131_floorpanelinner	1.2	2.7	2.16	Low	+5	+1	-7	None	No	NA
300700	Barriere	V071	222_bipolarinnermain	0.42	1.5	1.2	Same	+9	0	-2	None	No	NA
300300	Barriere	V070	106_bipolarinner	0.5	1.6	1.28	Bit High	-4	-5	-46	None	No	NA
17200	Barriere	V074	168_wheelhouseearinner	0.63	0.9	0.72	Same	+2	-3	-63	None	No	NA
201700	POLE	V077	129_floormanear2	0.7	0.9	0.72	High	-6	-19	+266	30	No	NA
14700	POLE	V075	245_floorarsupport	0.28	1.6	1.28	Bit High	0.7	0	-4	-2	No	NA
1100400	POLE	V073	427_doorfrontinteriormidbk	0.28	1.4	1.16	Same	+1	-1	+12	+2	No	NA
200000	ODB	V076	192_firewallundersupportmiddle	0.48	2	1.63	Bit High	+12	+11	+112	25	Maybe	1.5
13100	SOL	V068	180_midrailouterL	0.42	2	1.6	High	+14	+1	-24	-17	Yes	1
500000	POLE	V069	119_frontrotheadre	0.31	1.54	1.24	Bit High	+1	0	0	2	Maybe	2
301100	POLE	V072	230_roofrailsdeinier	0.35	1.6	1.28	Same	+2	-1	-2	4	Maybe	2

## 6.2 Hybrid component implementation analysis in Camry

The rear seat cross member which was chosen for patching was analyzed by preparing two different variants with two different thicknesses V095 (5 mm) and V097 (3 mm) patch of the FRP material. Then the crash simulation was performed and the results of the variants compared with the basis version are discussed in the following sections.

### 6.2.1 V095 - Floorpanxmember - 5 mm patch

The rear seat cross member which is reinforced with a part ID 12510 is illustrated in the figure 5.20. The geometry of the patch 12510 is designed by using the ANSA™ preprocessor [77] and imported into the Toyota Camry model. The patch is connected to the rear seat cross member by means of adhesive. The mass and thickness of the patch and the component are listed in the table 6.5. A mass reduction of **0.15 kg** was obtained for the rear seat cross member of part ID 12500.

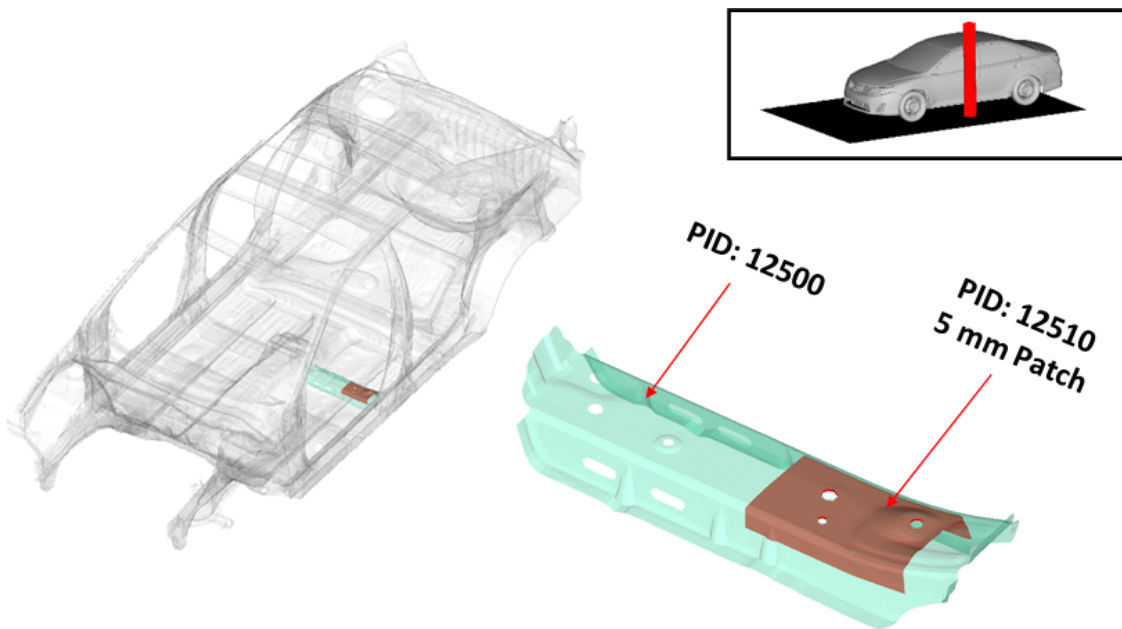


Figure 6.20: Rear seat cross member reinforced with patch thickness 5 mm

Table 6.5: Component characteristics comparison between basis and V095

Version	PID name	Mass [kg]	Thickness [mm]
Basis	Floorpanxmember	2.09	2
V095	Floorpanxmember	1.67	1.6
	Floorpanxmember_patch	0.272	5

The plasticity, intrusion and the failure comparisons are displayed in the figures 6.21, 6.22 and (6.23, 6.24, 6.25) respectively. The rear seat cross member was added with a more number of spot welds compared to the basis version. It was done to enhance the strength of the reinforced component. It was observed that the spotweld which

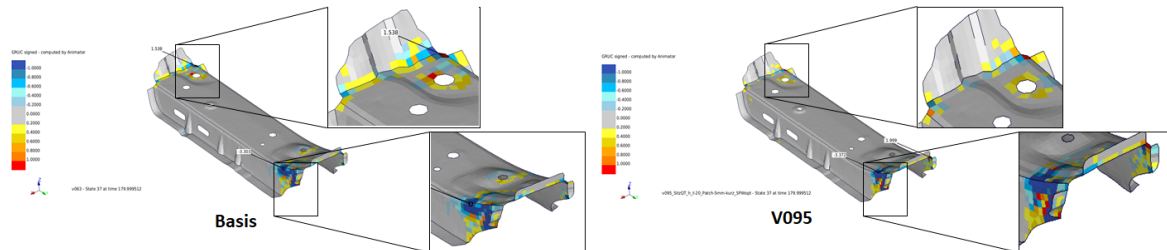


Figure 6.21: Plasticity comparison between basis and V095

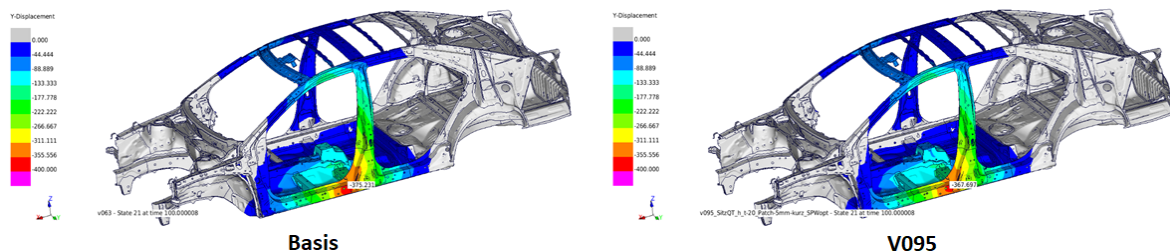


Figure 6.22: Intrusion comparison between basis and V095

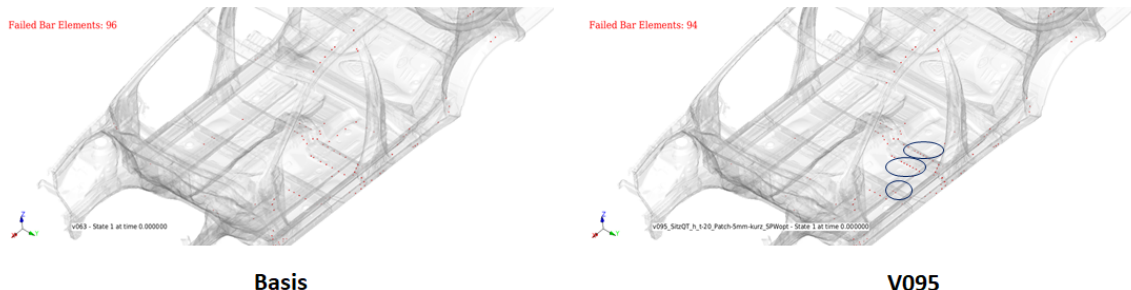


Figure 6.23: Spot weld failure comparison between basis and V095

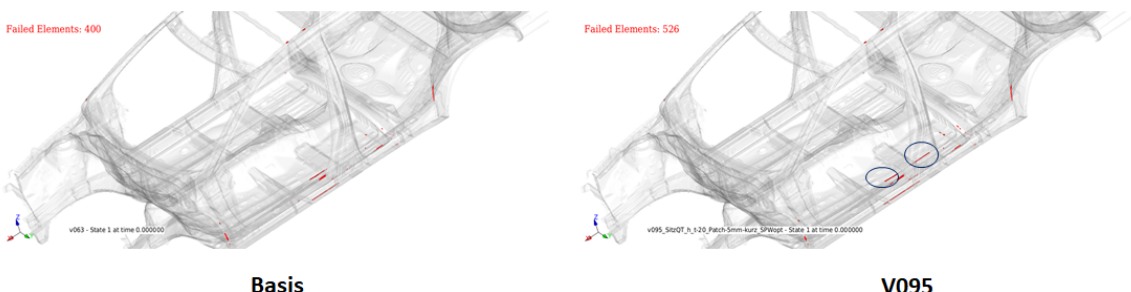


Figure 6.24: Adhesive failure comparison between basis and V095

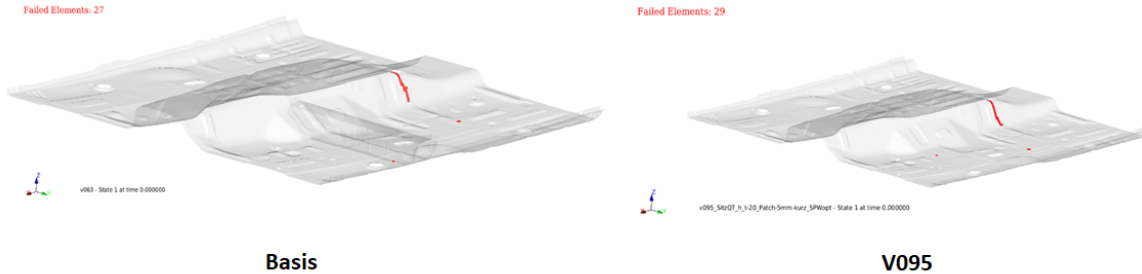


Figure 6.25: Material failure comparison between basis and V095

were in addition failed and the failure happens at a time period of 25 ms whereas the basis version spot welds fails much before at 15 ms. The adhesive failure also occurred at a later time of 50 ms whereas for the basis version it happens at 45 ms. The adhesive failure was bit increased due to the spot weld failure in the seat cross member region due to the increased load absorption capability near the impact site. In case of material failure, it remained on the same level and also the material failure happened slightly before at 50 ms whereas the basis version occurred at 60 ms. But the plasticity and displacement results showed good improvement as seen in the images shown. The plasticity of the variant V095 reduced to a greater extent on the top face of the cross member on both the leading and trailing edges because of the reinforcement. The overall displacement decreased by about 7.5 mm and also seen that the front seat cross member intrusion had increased. But on a general note, the variant performed better than the basis version.

### 6.2.2 V097 - Floorpanxmember - 3 mm patch

The rear seat cross member reinforced with the 3 mm thick patch is displayed in the figure 6.26. The component characteristics are summarized in the table 6.6. The crash simulation was performed and the results comparison for the different aspects were done in the same way as like the one done for the variant V095. As it is seen in the figure 6.27, the plasticity has reduced compared to the basis version because of the reinforcement. Also the criticality of the elements near the impact site for the 3 mm patch reduced when compared to the 5 mm patch. The displacement in figure 6.28 also decreased by about 6.8 mm and observed that the intrusions increased in regions of floor front and tunnel region.

Table 6.6: Component characteristics comparison between basis and V097

<b>Version</b>	<b>PID name</b>	<b>Mass [kg]</b>	<b>Thickness [mm]</b>
Basis	Floorpanxmember	2.09	2
V097	Floorpanxmember	1.67	1.6
	Floorpanxmember_patch	0.163	3

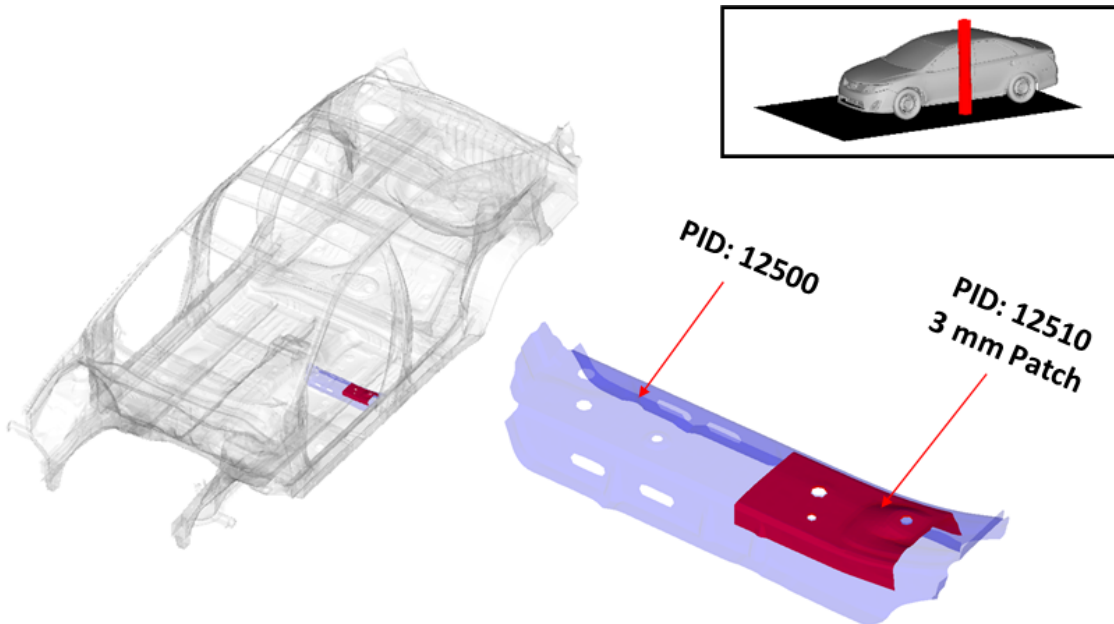


Figure 6.26: Rear seat cross member reinforced with patch thickness 3 mm

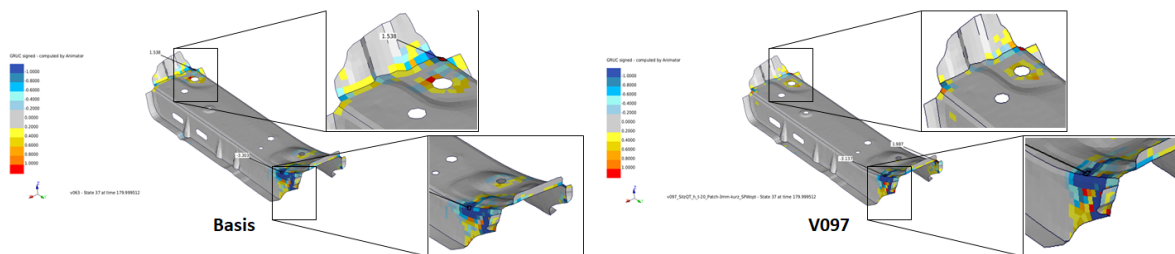


Figure 6.27: Plasticity comparison between basis and V097

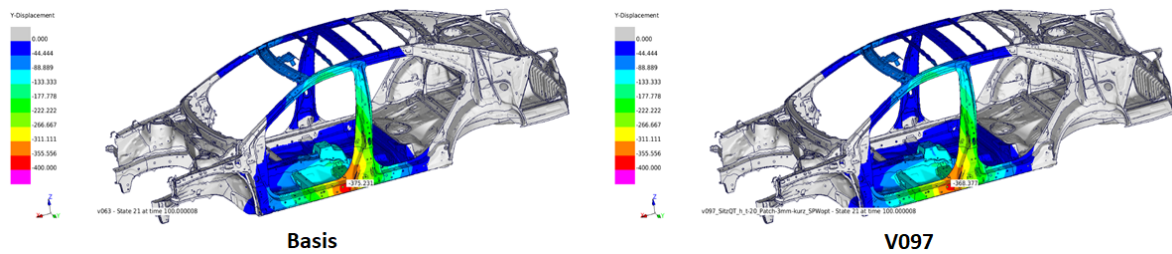


Figure 6.28: Intrusion comparison between basis and V097

The spot weld failure in figure 6.29 stayed on the same level but the newly added spot welds which were not present in the basis version failed. Even then, the failure happened at a much later time of 25 ms whereas the basis version spot failure occurred at 15 ms. The adhesive failure in figure 6.30 has increased underneath the region of the seat cross member and this is due to the buckling effect of the floor front with the increased resistance to load transfer in the mid region of the cross member due

to the presence of patch. But the failures happened at 50 ms whereas for the basis version it happens at 45 ms. So, it is concluded that the spot weld failure decreased and adhesive failure increased to a bit but they can be considered on the same level compared to the basis. Even though material failures occurred slightly before the basis version failure at 55 ms, the elements failed is also on the same level as shown in figure 6.31.

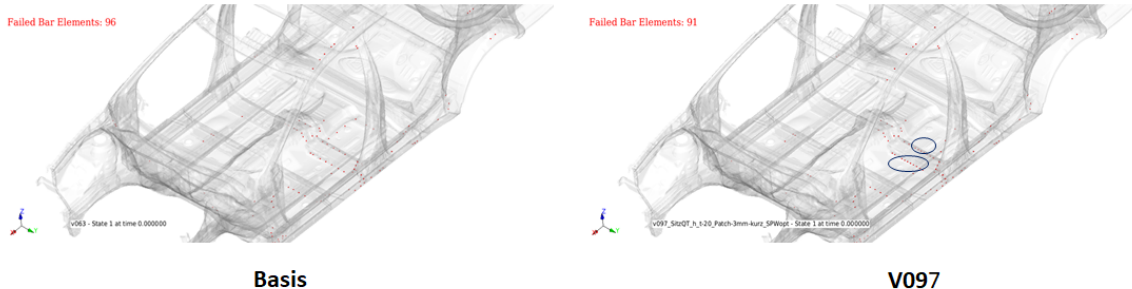


Figure 6.29: Spot weld failure comparison between basis and V097

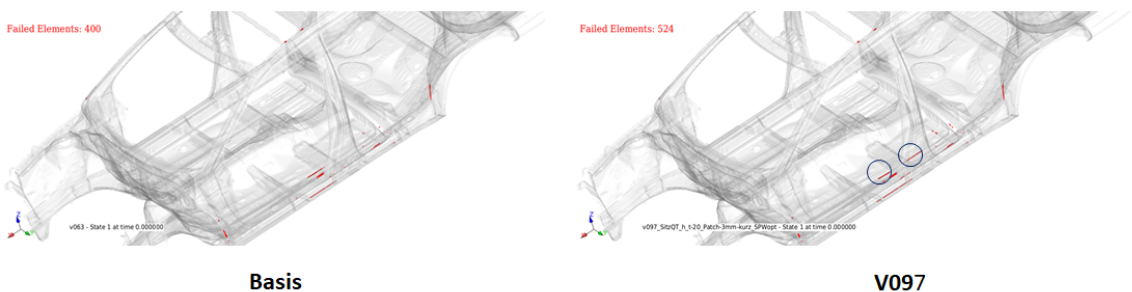


Figure 6.30: Adhesive failure comparison between basis and V097

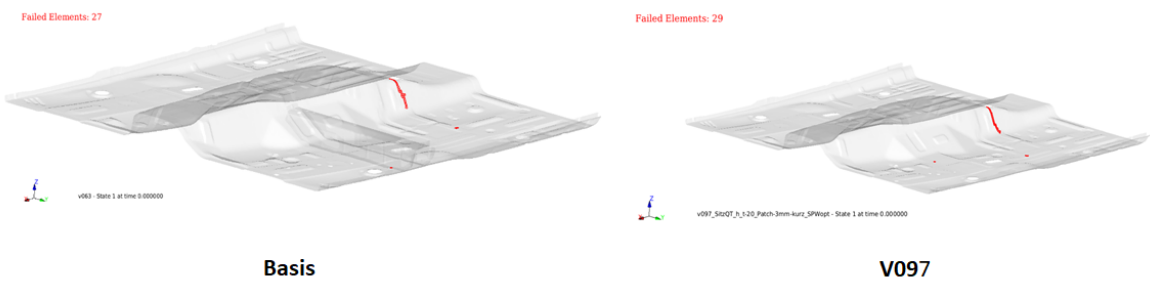


Figure 6.31: Material failure comparison between basis and V097

### 6.2.3 Preferred hybrid component variant

The comparison of the hybrid component versions V095 and V097 were compared against the basis versions in terms of reaction time at which the failures happened.

The results are catalogued in the table 6.7. It suggests that both the variants performed well after the addition of reinforcement into the seat cross member. The intrusion comparison is illustrated in the figure 6.32. The deformations almost remained the same after the impact at the maximum deformation time. It was observed that near the rear seat cross member, the tunnel front area was loaded more in the variants than in the base. This was due to the reinforcement which has higher load carrying capability and the floor front buckles more leading to a bit higher material and adhesive failures in the variants. But it can be concluded that the overall intrusion of the structure was reduced to a considerable extent. The plasticity was reduced in the patch reinforced regions but causing local plastification on the leading and trailing edges of the cross member and this cannot be avoided as the structure becomes weak specifically at those regions. The spot weld failures also occurred at a time later than the basis version and had decreased considerably in the variant V097 compared to the variant V095. Also the material failure occurred at a later time in variant V097 compared to both basis and V095. All these aspects leads to choose the variant **V097** as the reinforcement, since the amount of material which will be used as a reinforcement can be reduced and also further mass reduction of **0.52 kg/car** can be obtained compared to the V095 variant **0.30 kg/car**.

Table 6.7: Failure time comparison between basis, V095 & V097

Aspects	Basis	V095 5 mm patch	V097 3 mm patch
Spot weld failure	15 ms	25 ms	25 ms
Adhesive failure	45 ms	50 ms	50 ms
Material failure	60 ms	50 ms	55 ms
Intrusion	375.23 mm	367.6 mm	368.3 mm
Plasticity	High	Slightly increased	Slightly increased

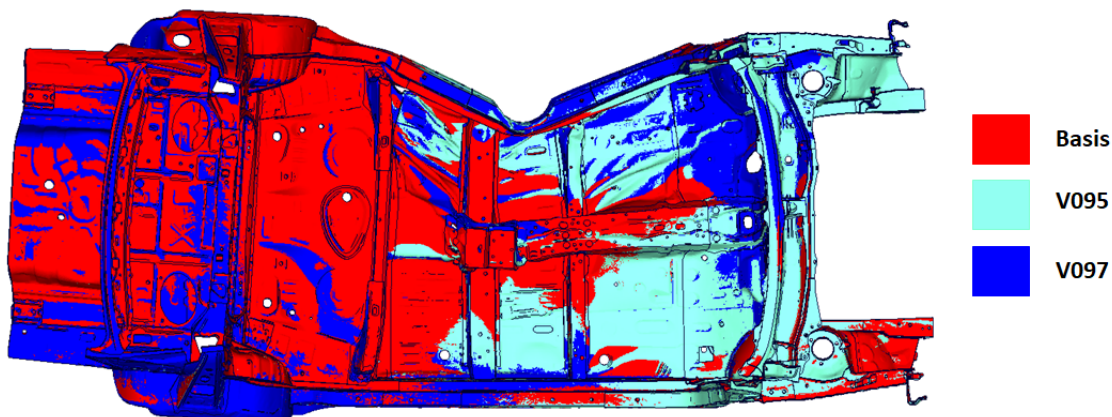


Figure 6.32: Intrusion comparison between basis, V095 & V097

The procedure of transferring the process simulation to the reinforced components

is contemplated in the following section.

### 6.2.4 Process simulation transfer to hybrid part

The procedure of transferring the process simulation to the rear seat cross member in the variants V095,V097 with patch thicknesses of 5 and 3 mm respectively can be done using the FE software ABAQUS™ in the same way as described in the section 5.1.3. The process simulation for the hybrid component will also be done in two steps. The first one is the thermal analysis and the second step is the mechanical analysis.

#### Thermal analysis of hybrid part

The cross member which will be imported into ABAQUS™ for thermal analysis is depicted in the figure 6.33. Since the parts were made up of shell elements, the surface of bonding agent overshadow certain regions of GFRP in the image. The geometry of the rear seat cross member is prepared by providing the material properties and defining the surface sets for assigning the film condition in ANSA™ preprocessor. The surface sets had to be defined so as to avoid the complication in the FE software since the imported part will be an orphan mesh [25].

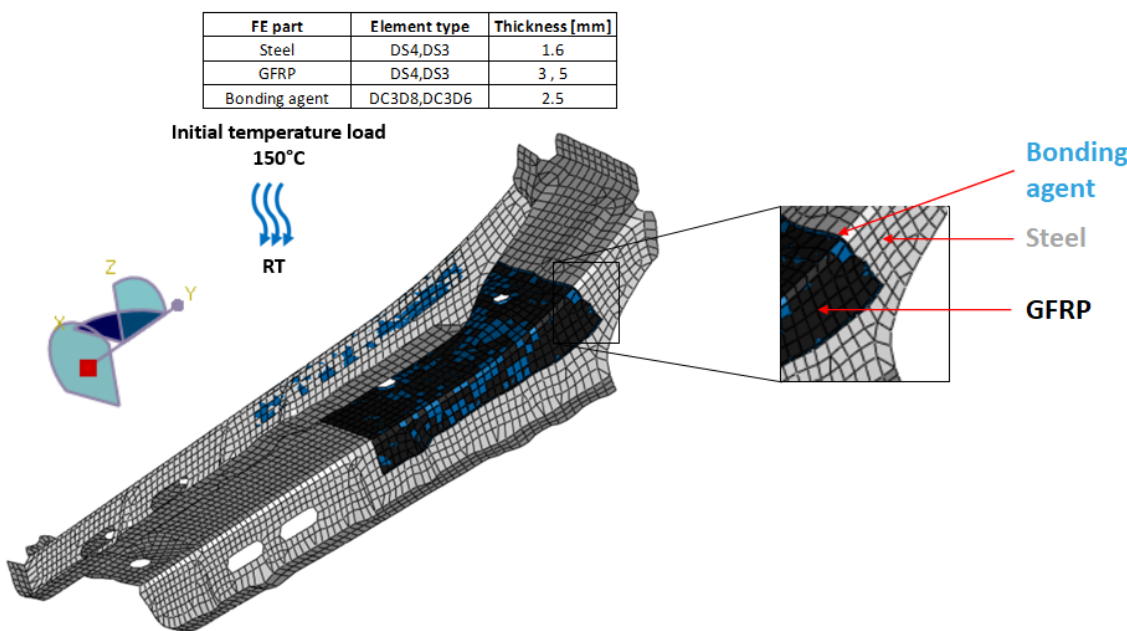


Figure 6.33: Hybrid part process simulation thermal analysis FE model

In this case only the steel and the GFRP film conditions will be used, as in the industry there will be no need of support plate. The film conditions applied for the cooling simulation are referred to the tables 5.2, 5.7. The thermal properties used for the simulation are from tables 5.1, 5.5, 5.6, 5.8. The time period for the simulation will

also be the same around 3950 seconds and the bonding agent will be able to transfer the heat because of the \*TIE connection between the steel and GFRP components. Once the analysis is completed, the nodal temperature results will be transferred to the mechanical analysis model deliberated in the following section.

### Mechanical analysis of hybrid part

The mechanical analysis procedure is similar to the one explained in section 5.1.3. The mechanical analysis FE model is represented in the figure 6.34. The mechanical properties used for steel part is only the elastic properties from table 5.9 since at a temperature of 150°C the plasticity is absurd. The elastic property and thermal expansion coefficient of GFRP are from the figures 5.7, 5.9 respectively. The elastic properties for the bonding agent is from figure 5.8 and the thermal expansion coefficient from table 5.10 and the damage properties from figure 5.13. The output database file from the thermal analysis will be imported into the mechanical model and no boundary conditions were employed for this analysis as like in the manufacturing process in industry.

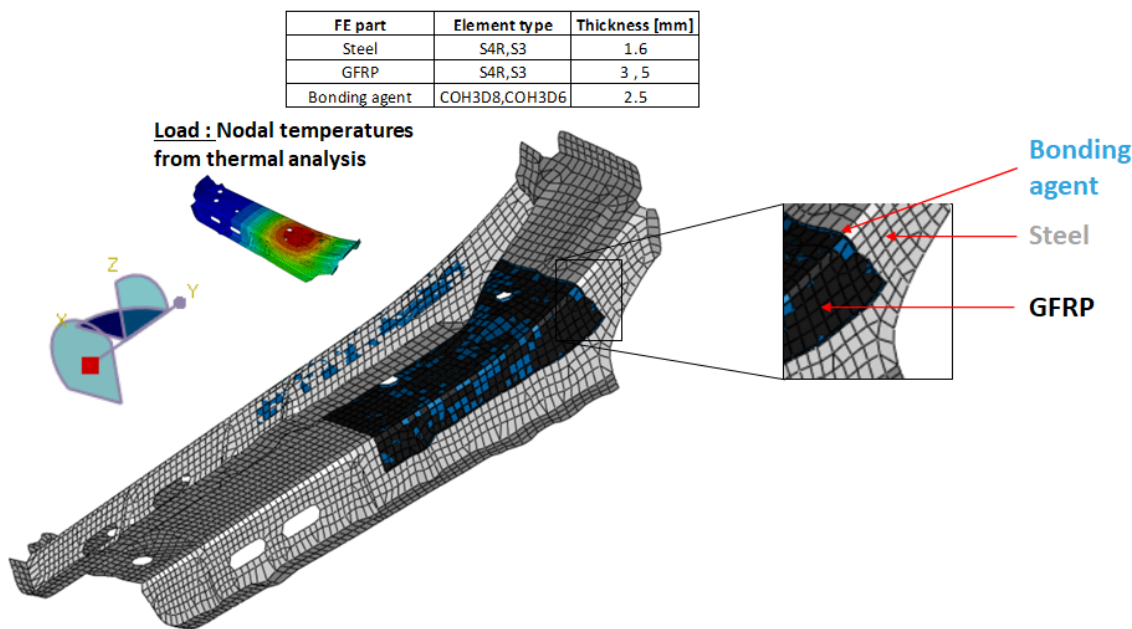


Figure 6.34: Hybrid part process simulation thermal analysis FE model

Thus the process simulation is transferred to the hybrid part and the results of thermal and mechanical analysis will be discussed in chapter 7.

# 7 Results

In this chapter, the results of the most important parts of this research are clarified. Initially, the thermal and mechanical results of the hybrid plate process simulation followed by the process validation are illustrated. Finally the results of the process simulation transferred to the hybrid rear seat cross member will be revealed.

## 7.0.1 Cooling process simulation results

### Thermal analysis

The cooling curves of the hybrid plate process simulation were already illustrated in section 5.1.3. The temperature distribution of the components in the hybrid plate after a certain time period of 190 seconds is displayed in the figure 7.1. As it is supposed to be, the support plate cools faster than the steel plate as seen by the temperatures in the figure. Also the thermal conductivity of the bonding agent is very low so that the heat conduction between steel plate and upper surface of GFRP happens at a slower rate. But the lower surface of the GFRP should be at a higher temperature than the upper surface because of its contact with the support plate.

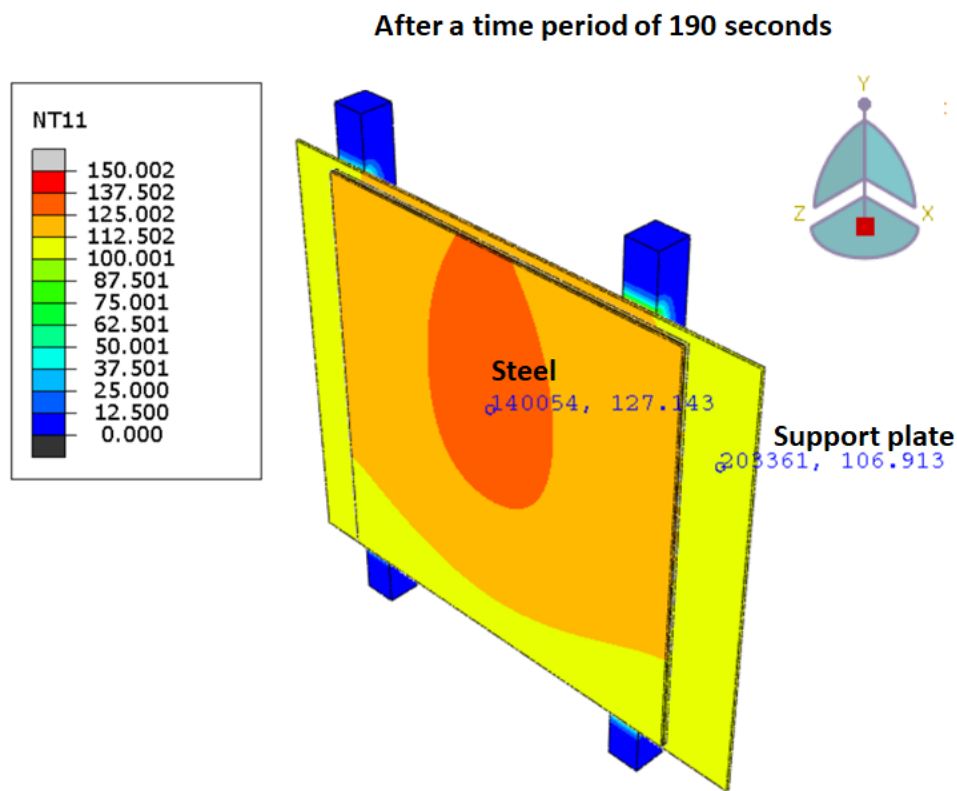


Figure 7.1: Temperature distribution of hybrid plate components

Inspite of the support plate transferring heat to the surrounding, it must also conduct heat at a much faster rate to the lower GFRP surface than the steel plate through the bonding agent. The heat distribution must be stagnated on the lower surface since the GFRP laminate is fixed firmly onto the support plate and hence it must be higher than the upper surface of the laminate. This is the actual physical behavior in the experiment also where the temperature T1 on upper surface is lower than the temperature T2 on the lower surface of laminate and observed a temperature difference of about 5 degrees. This is proved by the temperature distribution in the simulation also represented in the figure 7.2.

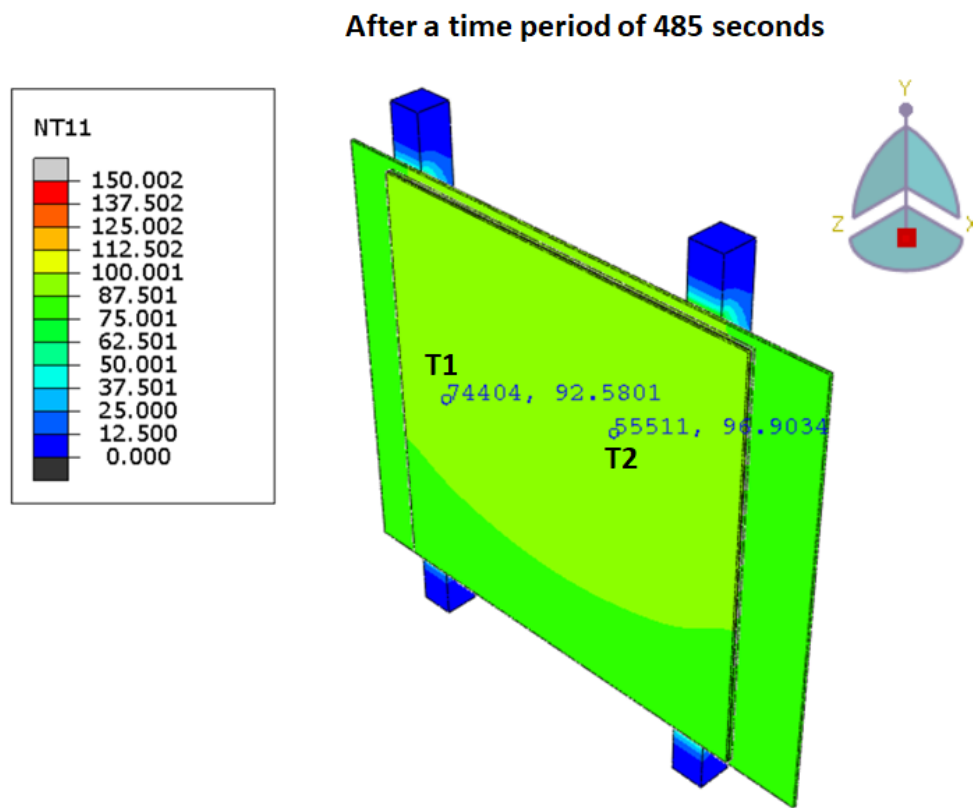


Figure 7.2: Temperature distribution on upper and lower surface of GFRP

The temperature difference in the simulation is also about 4.5 degrees which serves that the simulation results are in good correspondence with the experimental results. But after a time period of 750 to 1500 seconds, the temperature difference slightly increased from 5 degrees to 10 degrees. But this is due to the reason of film coefficients used for GFRP from 5.6. The temperatures T1 and T2 in the GFRP simulation model were interdependent and if it is tried to fit T1 temperature then the other temperature deviates extensively. But this correlation of the simulation with experimental cooling trials of GFRP was not so good compared to the steel and support plate and it is unavoidable too. Hence, it can be agreed that the cooling curves of the process simulation were having meager differences with the experimental results.

## Mechanical analysis

The mechanical analysis simulation setup is described in the section 5.1.3 where the boundary conditions such as the wooden strip and GFRP lower surface are fixed. The various features such as the displacement of the adherends, Scalar stiffness degradation (SDEG) and Damage initiation criteria (QUADSCRT) of the adhesive are examined. This is done because FRP materials have different thermal expansion coefficients along the longitudinal and transverse directions. The longitudinal thermal expansion coefficient depends upon the fiber type whereas the transverse thermal expansion coefficient depends on the resin [34]. All the aforementioned features are based upon two categories in which either the thermal expansion coefficient of the GFRP is isotropic or orthotropic. So, the mechanical analysis results with isotropic temperature dependent thermal expansion coefficients are conferred in the following segment. All the other mechanical properties will remain the same and the thermal expansion properties used for the following results is listed in the table 7.1.

Table 7.1: Isotropic temperature dependent thermal expansion coefficients of GFRP

$\alpha_{11}$	$\alpha_{22}$	$\alpha_{33}$	Temperature [°C]
$1.77\text{e}^{-5}$	$1.77\text{e}^{-5}$	$1.77\text{e}^{-5}$	20
$1.94\text{e}^{-5}$	$1.94\text{e}^{-5}$	$1.94\text{e}^{-5}$	100
$1.94\text{e}^{-5}$	$1.94\text{e}^{-5}$	$1.94\text{e}^{-5}$	180

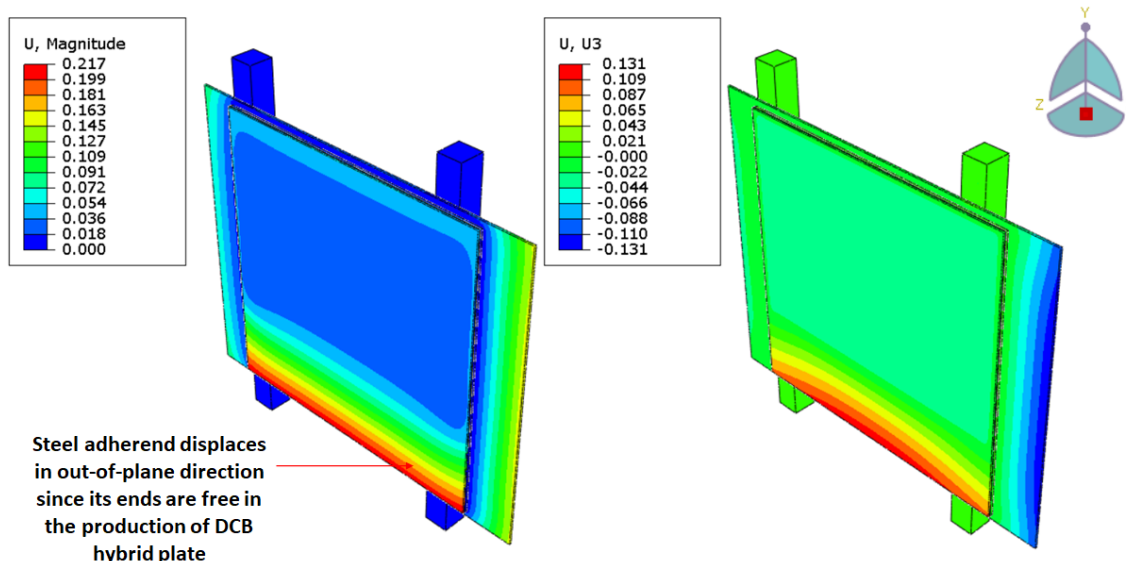


Figure 7.3: Magnitude of displacement of the hybrid plate components based on isotropic CTE of GFRP

The overall displacement and the out-of-plane displacement results of the hybrid plate is presented in the figure 7.3. The SDEG and QUADSCRT results of the bonding agent are displayed in the figure 7.4. It was observed that the steel due to its

expansion effect during cooling moves in the z-direction. But this displacement happens only in the edges and a maximum of 77% stiffness degradation was found in the bonding agent. Although there can be traces of some regions along the edges of the bonding agent where the contact stresses have already crossed the specified initial limit. But the effects were minimal since the thermal expansion coefficient of GFRP was not high enough compared to other adherends such as Aluminium.

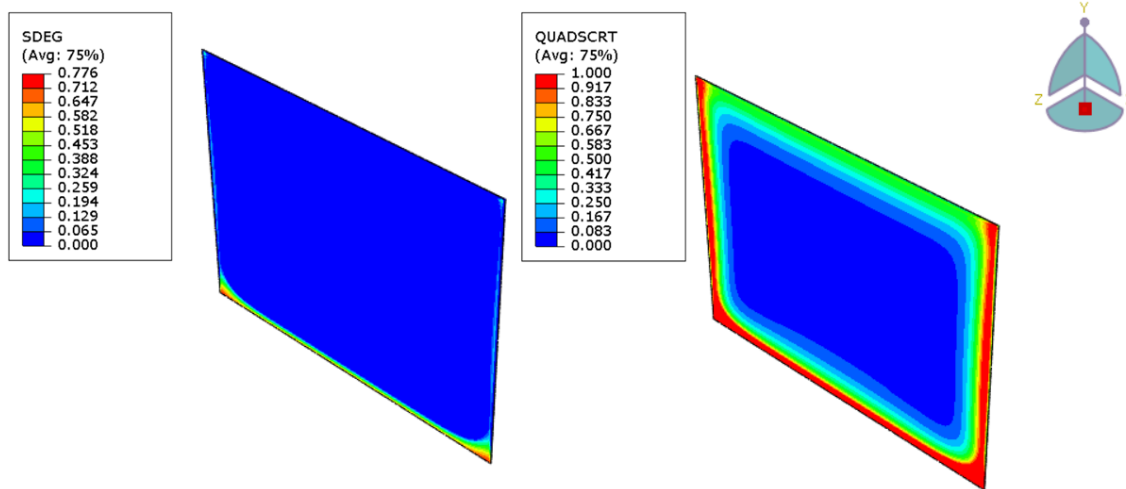


Figure 7.4: Scalar stiffness degradation and damage initiation criterion results of the bonding agent based on isotropic CTE of GFRP

The next case is about applying the orthotropic thermal expansion coefficients for GFRP. The transverse direction thermal expansion coefficients are the same but the longitudinal expansion coefficients are referenced from the research article [34]. The properties are summarized in the table 7.2.

Table 7.2: Orthotropic temperature dependent thermal expansion coefficients of GFRP [34]

$\alpha_{11}$	$\alpha_{22}$	$\alpha_{33}$	Temperature [°C]
$4.4\text{e}^{-6}$	$1.77\text{e}^{-5}$	$1.77\text{e}^{-5}$	20
$4.4\text{e}^{-6}$	$1.94\text{e}^{-5}$	$1.94\text{e}^{-5}$	100
$4.4\text{e}^{-6}$	$1.94\text{e}^{-5}$	$1.94\text{e}^{-5}$	180

The displacements of the hybrid plate components upon the application of the orthotropic thermal expansion coefficients is shown in the figure 7.5. The magnitude of the overall displacement has increased at a minimal scale of about 0.001 mm as it is shown in the figure 7.5. On a comparison to the isotropic thermal expansion coefficient of GFRP it is almost the same and the contour resembles the same. The stiffness degradation and the damage initiation criterion for the bonding agent based on the orthotropic properties is presented in the figure 7.6. It was seen at the top

edge of the bonding agent, where there is an increase in the area of damage initiation due to the reduced thermal expansion coefficient in the material orientation 1-direction of GFRP. It can also be clearly understood from the figure 7.7 where the overall displacement magnitude of GFRP is compared based on the isotropic and orthotropic thermal expansion coefficients. The displacement in the central region of the GFRP laminate tend to decrease because of the lower thermal expansion coefficient along the longitudinal or the 1-direction. Also there is an increase in the displacement below the central region where the edge of the bonding agent is placed. The displacement at this region slightly increases due to the oppression of the steel adherend because of its higher thermal expansion coefficient.

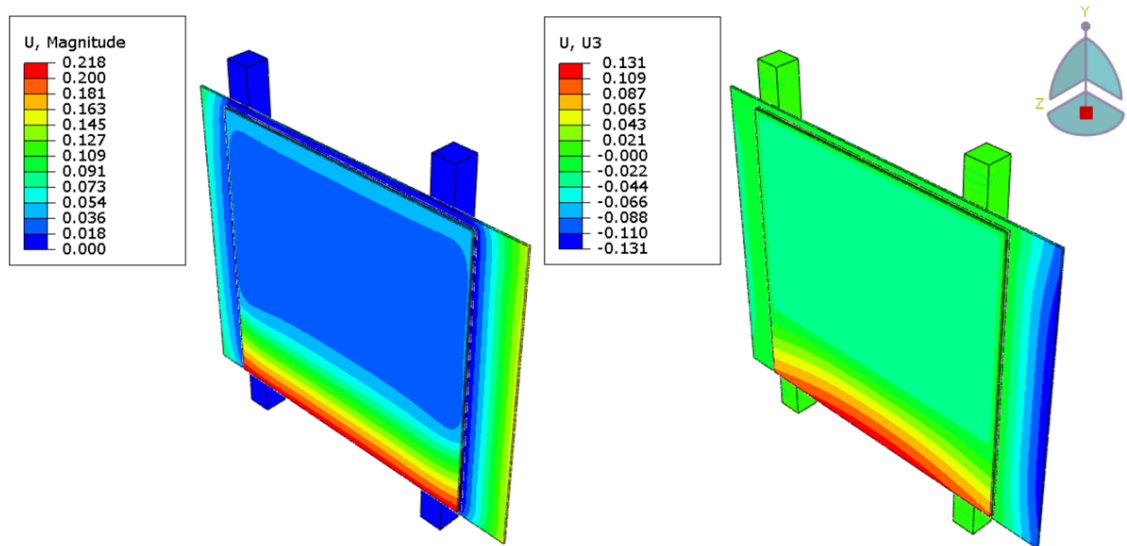


Figure 7.5: Magnitude of displacement of the hybrid plate components based on orthotropic CTE of GFRP

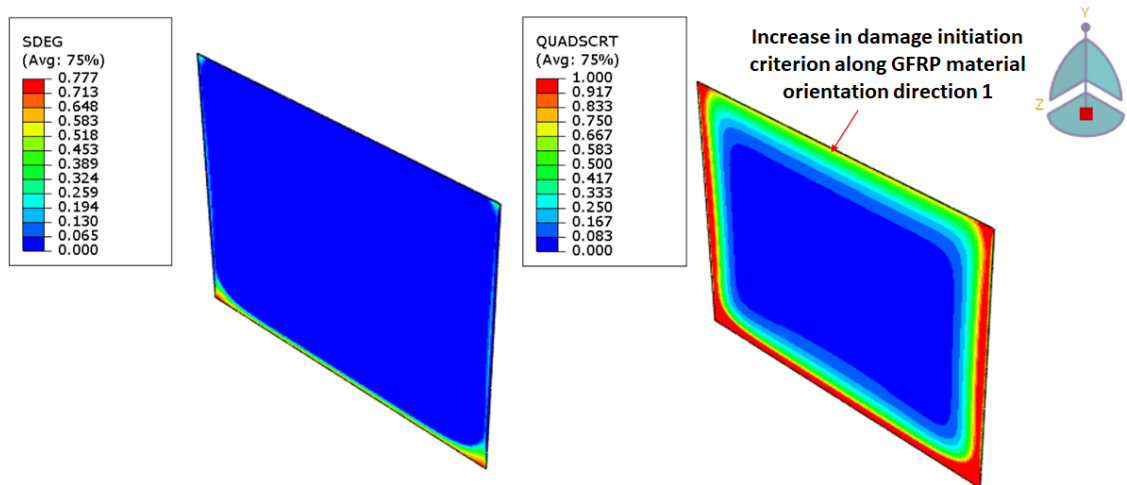


Figure 7.6: Scalar stiffness degradation and damage initiation criterion results of the bonding agent based on orthotropic CTE of GFRP

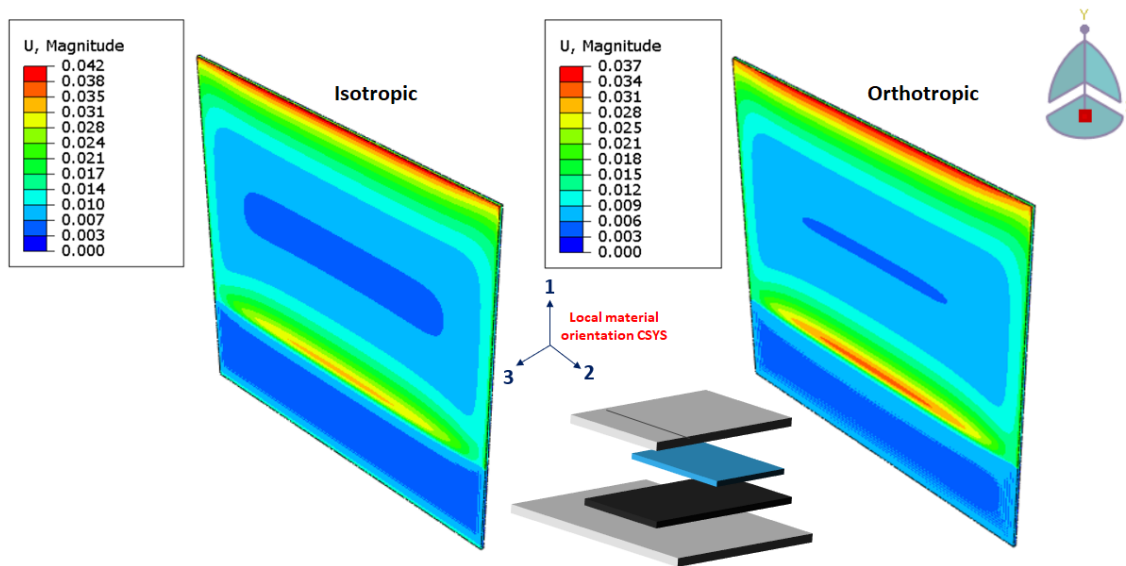


Figure 7.7: Comparison of displacements for the GFRP adherend based on isotropic and orthotropic thermal expansion coefficients

It can be concluded that the different direction thermal expansion coefficient for the FRP material also plays an important role in influencing the damage initiation within bonding agent.

Even though all the above results correspond to the boundary conditions specified in section 5.1.3, it was also made sure to check the results if the GFRP lower surface is not fixed. So, the results for the boundary condition such as the wooden strip fixed and the GFRP lower surface not fixed are shown only for the isotropic thermal expansion coefficient of GFRP in table 7.1. The displacement results are shown in the figure 7.8. It can be seen that the a maximum displacement of about 0.89 mm is found in the support plate. Also the contour is bit different when compared to the figure 7.3 where the lower surface of laminate is fixed. The figure 7.3 proves a bit more of physical behavior compared to the figure 7.8, because the steel plate with its one edge not fixed over the bonding agent displaces outward in the z-direction by about 0.13 mm. Also during the cooling procedure, the support plate is expected to contract and it is observed that it displaces by about 0.13 in the negative x-direction which proves the opinion. From this it can be seen that the results of the boundary condition where the GFRP lower surface fixed proves to be more credible than the one where it is not fixed. The SDEG and QUADSCRT results are also presented in the figure 7.9 for the GFRP lower surface not fixed. There was no stiffness degradation within the bonding agent noticed and the damage initiation criteria was found to be less than that of in the figure 7.4. The coefficient of thermal expansion (CTE) of the GFRP and steel differ by slight values and tend to have a CTE mismatch effect. But the stiffness degradation results in the figure 7.9 shows no such effect and this proves that the boundary condition which is adapted (lower surface of GFRP

not fixed) leads to slightly different results. It can be only decided after the process validation simulation results to choose which boundary condition as the results indicated above are bit tricky even though the results with laminate lower surface fixed proves to be more compromising. The reason behind it is that the displacement or SDEG is based upon only the thermal results and no such validation is done for the mechanical results.

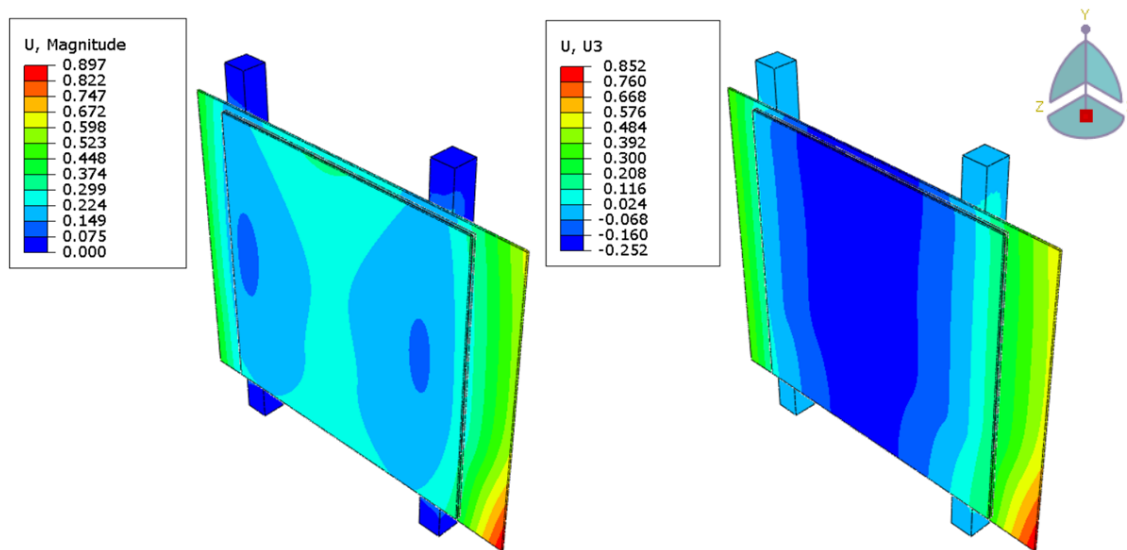


Figure 7.8: Comparison of displacements for the GFRP lower surface not fixed based on isotropic thermal expansion coefficient

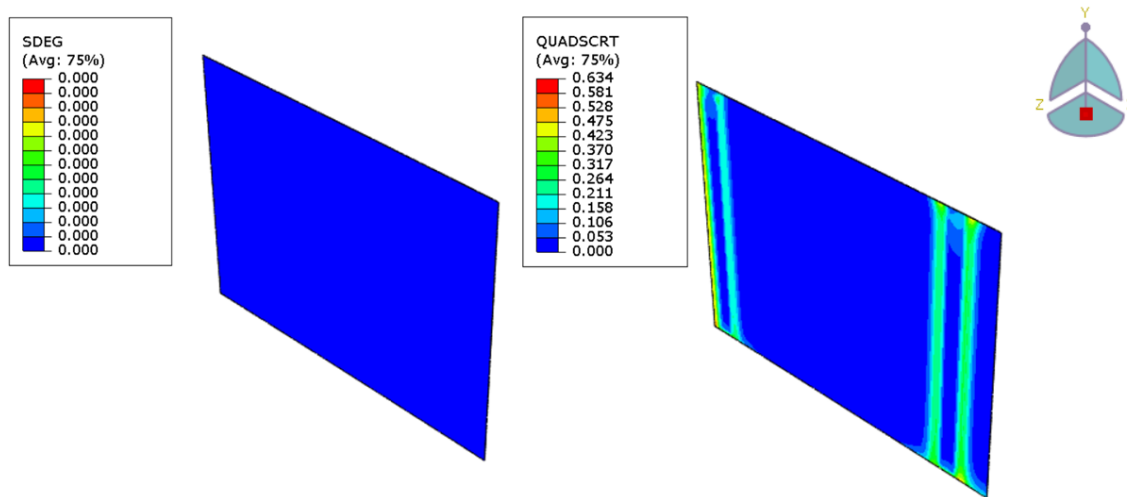


Figure 7.9: Scalar stiffness degradation and damage initiation criterion results of the bonding agent

In the following section the results of the process validation simulation will be presented.

## 7.0.2 Process validation simulation results

### Thermal analysis

The cooling curves of the process validation thermal simulation were already compared with the experimental results in the section 5.1.4. A maximum difference of about 7 degrees was found between the simulation and experimental results which implies to be a good result. As expected the temperature measured at the GFRP surface cools down slower than the support plate. The temperature difference between T1 and T2 in the experiment was about 10 degrees after 500 seconds. In the simulation the temperature difference was about 3 degrees between the two temperatures. This is also due to the reason that the GFRP film coefficients fitting simulation had a temperature difference of 5 degrees with its experiment. But this temperature difference is not so high and can be considered. The results are then transferred to the mechanical analysis FE model and discussed in the following section.

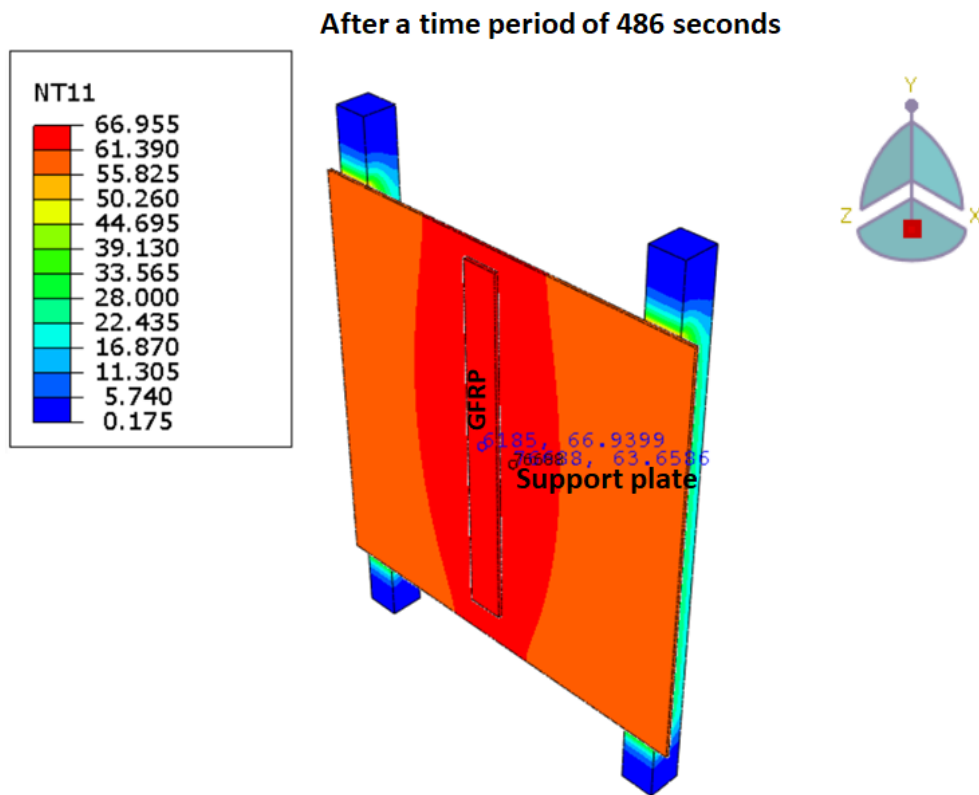


Figure 7.10: Temperature distribution of hybrid plate components of process validation simulation

### Mechanical analysis

The mechanical analysis results are to be classified based upon the boundary condition (GFRP lower surface fixed or not fixed) to verify the results obtained in the

## 7 Results

previous section 7.0.1. But the thermal analysis results will remain the same for both types. The thermal expansion coefficients applied for GFRP are from table 7.1. The boundary conditions were implemented and the displacement along the length of the steel part is shown in figure 7.11. It was seen that for the GFRP unfixed BC, the displacements were high compared to the other. The measured displacements in the simulation were compared against the experimental results and presented in the figure 7.12. The simulation displacement values were converted according to the coordinates of the experiment and found that a maximum displacement of 0.04 mm is found in the simulation which is short of the maximum experimental value at 0.1 mm. The difference between the simulation and experiment was about 0.06 mm.

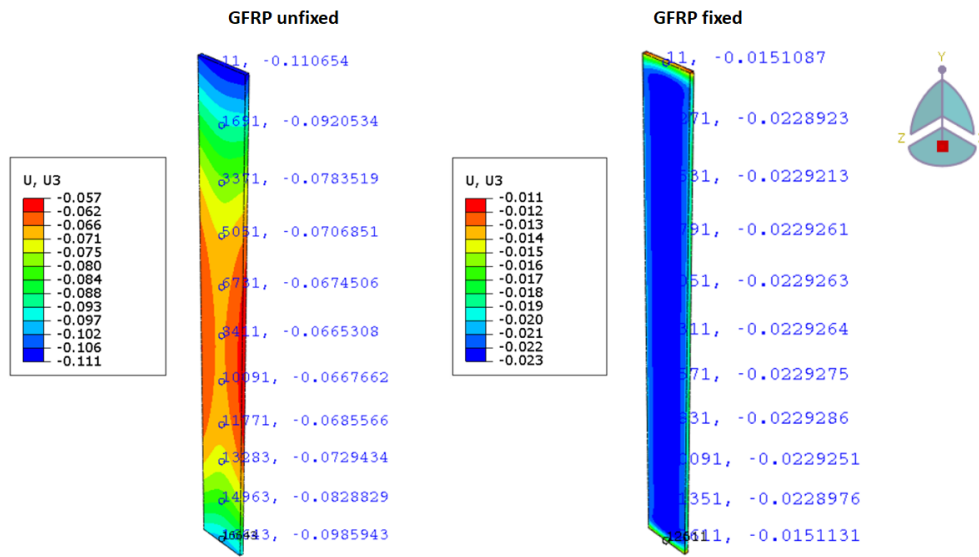


Figure 7.11: Displacement of the steel part based upon the different boundary conditions

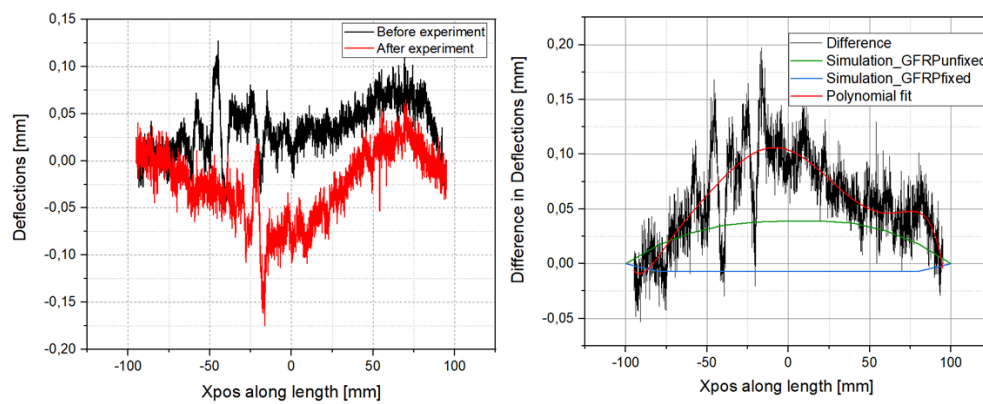


Figure 7.12: Steel part simulation displacements Vs experimentally measured deflections before and after experiments

The deflections were expected to be almost in this range since the thermal expansion coefficient of the steel and GFRP partners are only slightly different from each

other. To make sure about this the thermal expansion coefficients of the GFRP from table 7.1 are taken as the reference and increased by 20% and employed in the simulation to know about the displacements. Also it was decreased by 20% and the changes are observed. The boundary condition employed for this is the GFRP lower surface unfixed since the simulation results finds an acceptable correlation with the experimental results. The displacement results of the steel part from the simulation based upon the difference in thermal expansion coefficients is displayed in the figure 7.13. It was seen that the displacement increased along the length of the steel part with increase in CTE of GFRP. Due to some complications to plot the displacements, they are tabulated and summarized in the table 7.3.

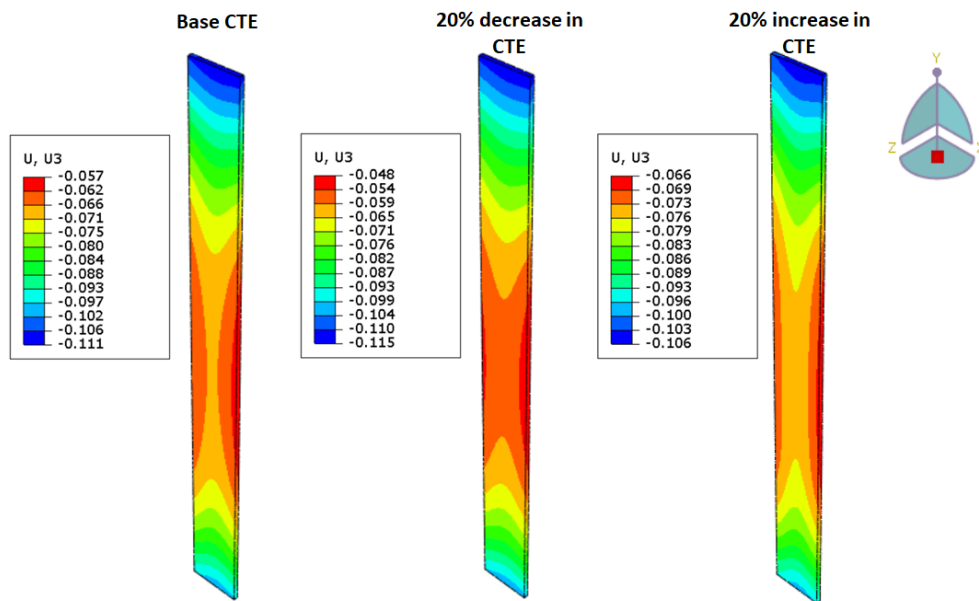


Figure 7.13: Steel part simulation displacements based on increase and decrease of CTE of GFRP

Table 7.3: Displacements of the steel part based on different rates of CTE of GFRP

<b>Xpos along length [mm]</b>	<b>Base</b>	<b>20% decrease</b>	<b>20% increase</b>
100	-0.110	-0.115	-0.106
80	-0.092	-0.091	-0.092
60	-0.078	-0.073	-0.082
40	-0.07	-0.063	-0.077
20	-0.067	-0.059	-0.075
0	-0.066	-0.057	-0.075
-20	-0.066	-0.058	-0.075
-40	-0.068	-0.06	-0.075
-60	-0.072	-0.067	-0.078
-80	-0.082	-0.08	-0.085
-100	-0.098	-0.1	-0.096

The negative sign indicates the inward z-direction and as it is seen from the table that at only the edges, the displacement tend to decrease with increase in CTE whereas from -80 to 80 mm along the length, the displacement increases with the CTE of GFRP. This happens as a reason of some pulling effect of GFRP with the steel part at the top and bottom edges and contracts in the middle region forming a kind of inward displacement. This can be clearly understood from the figure 7.14.

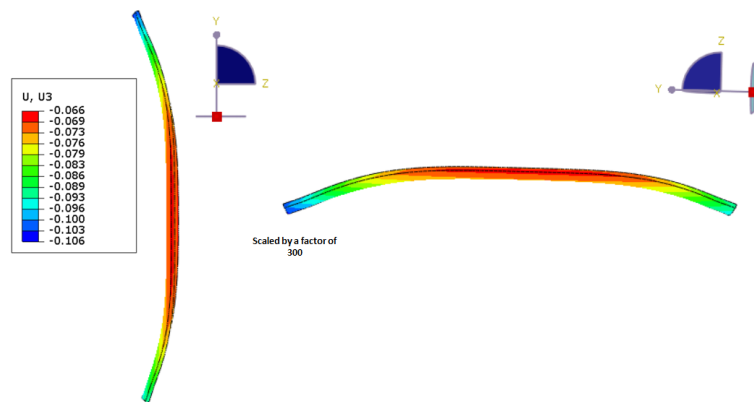


Figure 7.14: Steel part displacement scaled view

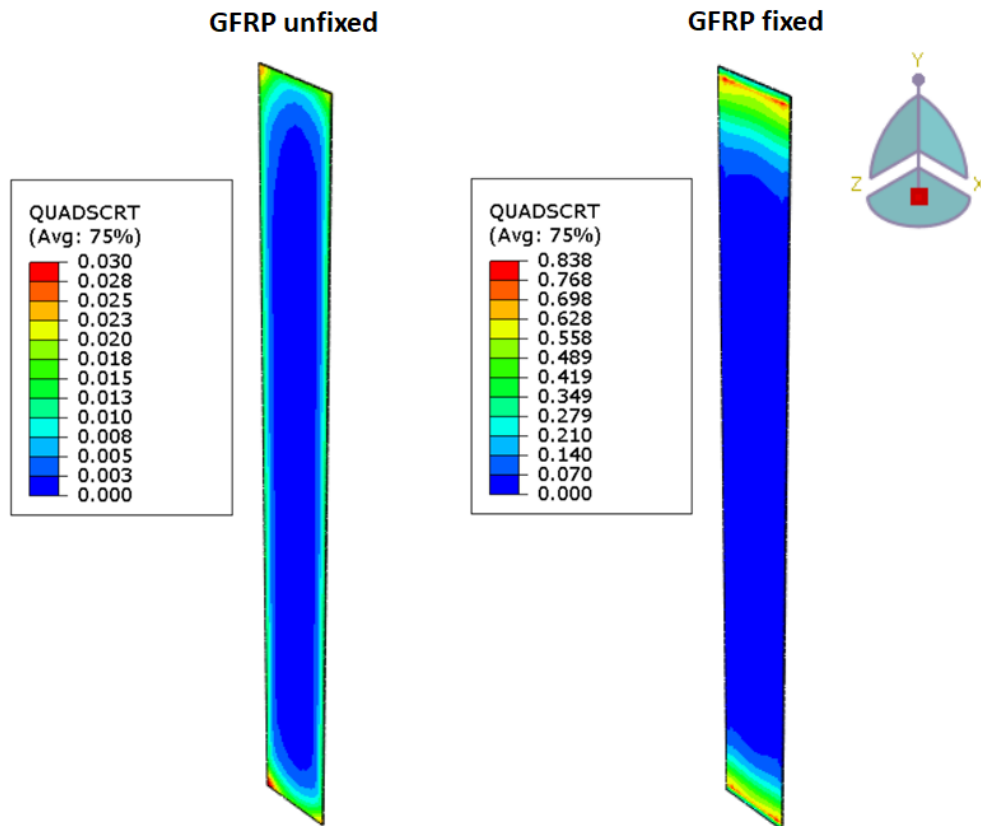


Figure 7.15: Steel part simulation displacements Vs experimentally measured deflections before and after experiments

Since the SEDG values were 0 (it might also be because of the CZM model used from BETAMATE adhesive), only the QUADSCRT values are presented in the figure 7.15 for the bonding agent based upon the boundary conditions. It is observed that for the GFRP fixed BC, the damage initiation criterion values were high when compared to the accomplice. The behavior resembles the same from the hybrid plate process simulation. The QUADSCRT values are comparatively low for the GFRP unfixed BC, but the displacements found to be compromising with the experimental results. This proves that GFRP laminate has some influential thermal expansion effects when placed upon the support plate. Hence, it can be verified that the BC is GFRP unfixed and the results can be affirmed based on the conclusions derived from the last two sections.

In the next section, the results from the hybrid part employed in the Toyota Camry model based upon thicknesses are conferred briefly.

### 7.0.3 Process simulation results of hybrid part from Camry

#### Thermal analysis

The process simulation method is then transferred to both the hybrid part of different thicknesses as described in the section 5.1.3. The temperature distribution of the hybrid components after 570 seconds are displayed in the figure 7.16. It was seen that for the part with higher thickness the cooling is bit slower than the part with lower thickness. The maximum temperature in the 5 mm patch is about 93 °C whereas in the 3 mm patch it is about 84 °C. In the region of the patch, since the conduction happens between the steel and GFRP part through bonding agent which has lower thermal conductivity the temperature distribution is high in that area. The temperature on the top surface of the steel part is about 91 °C approximately at this region while the temperature on the GFRP surface which is underneath the hat section is about 88 °C approximately. But the contour of the temperature distribution in the remaining areas (other than patch region) tends to be the same as that of the 3 mm hybrid component. These results are then to be transferred for the mechanical analysis which is deliberated in the following section.

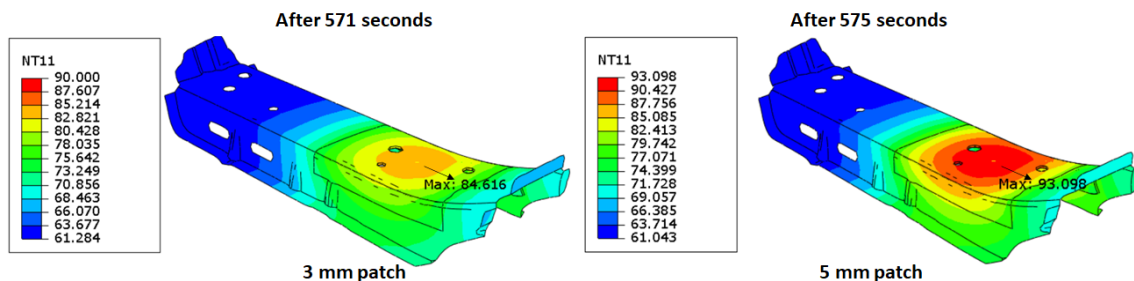


Figure 7.16: Thermal analysis results of the hybrid part

## Mechanical analysis

The mechanical analysis results such as the displacement of the component in figures 7.17,7.18 and SDEG of the bonding agent is shown in the figure 7.19.

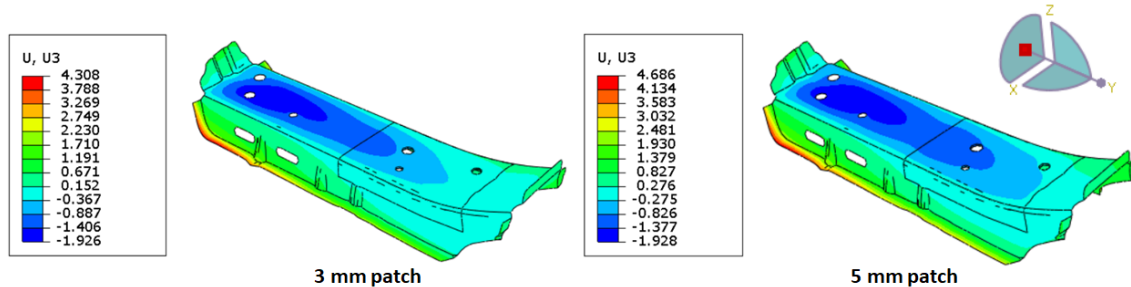


Figure 7.17: Displacement results of the hybrid part

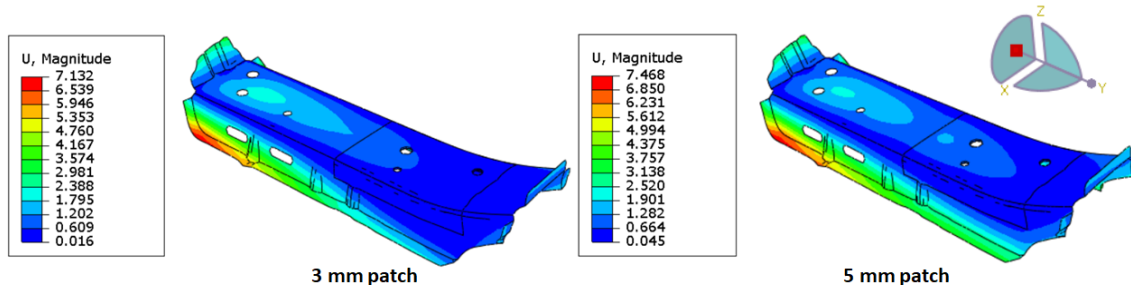


Figure 7.18: Overall displacement results of the hybrid part

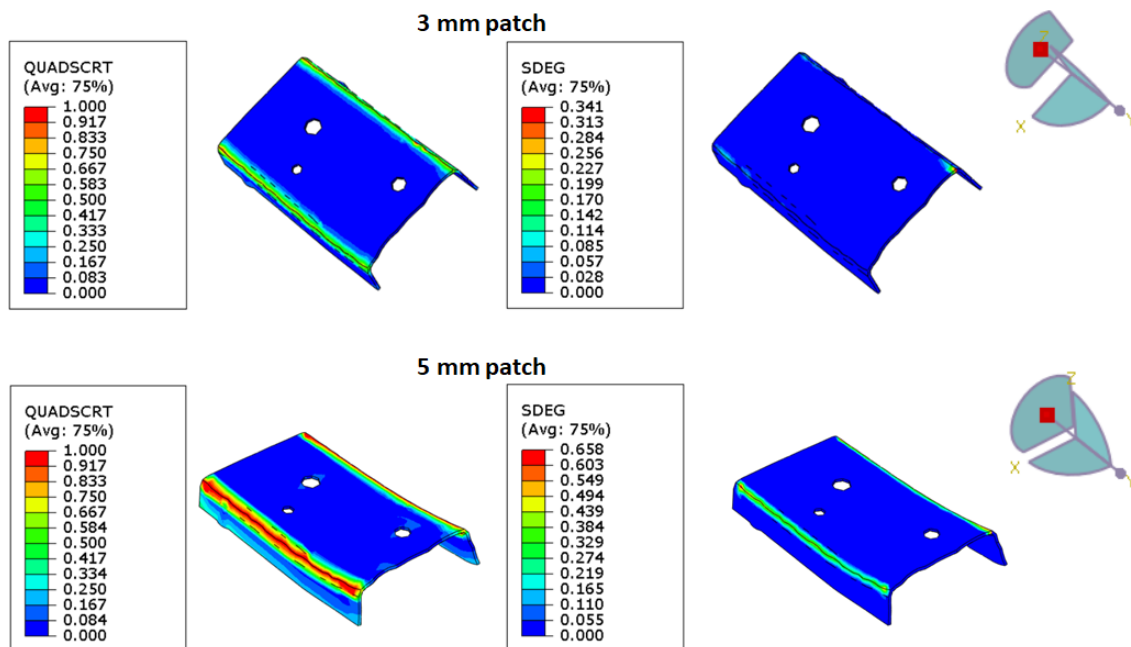


Figure 7.19: QUADSCRT and SDEG values of bonding agent in the hybrid component

No boundary condition was adapted for the mechanical analysis model. The displacements in the z-direction were observed to be high for the part with maximum thickness as the cooling rate is said to be slow rather than the part with minimum thickness. Also the contour on the upper surface of the steel part was found with increase in displacement in the regions near to the 5 mm patch. This is because of the higher contraction behavior of the part with higher thickness. An overall magnitude of 7.468 mm was noticed for the part with 5 mm patch and 7.132 mm for the part with 3 mm patch. It is found that since the displacement increases within the lower region of the cross member in the 5 mm patch, the damage initiation is set to be high rather than 3 mm patch. The SDEG values as expected to be are high for the 5 mm patch rather than the accomplice and also it is observed that both the analyzed parameters are high along the flanks of the patched region. It is because of the increase in thickness of the patch which results in increase in stiffness of the patch. The analysed parameters can also be reduced in the flank regions by an example of hat profile hybrid component provided in [1] where the GFRP can be used on the top side and steel underneath it with the bonding agent.

Thus, the takeaway points from the process simulation, process validation simulation are depending on the thermal expansion coefficient and thickness of the patch components, henceforth there will be a slight change in the bonding agent stress. Also adapting the right boundary condition for the model in the process simulation also leads to different results than the one with not say incorrect boundary condition but the one which is not predictable.

## 8 Summary

Since the adhesive undergoes complex mechanical and thermal stresses during manufacturing and also the drying process in the oven at 180° C after the CDC process due to the CTE mismatch problem of the different joining materials in a multi-material hybrid structure BIW, it is important to predict the adhesive damage before in hand to ensure a good reliable final product. The present work contributed to identify and evaluate the critical regions in the bonding agent after the manufacturing of the hybrid part and the method implemented can be used to calculate the deformations of the joining partners.

In Chapter 1, the importance of lightweight construction principle followed by the motivation and the goal to suit the combined fusion and adhesive bonding technique for different materials such as the steel and FRP is discussed.

The Chapter 2 involves a brief introduction to the use of the FRP and steel materials in the BIW of vehicles. Also the previous investigations for both the process and the mechanical test simulations related to the adapted joining technique are briefly deliberated to devise the process procedure. In addition, the review of the different process parameters which are involved in this technique is elaborated.

In Chapter 3, the questions which are to be solved such as what approach can be used for the simulation and what are the necessary things needed to accomplish the objective are framed and filed.

The Chapter 4 discussed about the various equipments needed for carrying out the experiments which are part of the process procedure and also the experimental procedures in the process workflow such as the individual cooling experiments, production of hybrid plate and also the validation of the procedure. The bending tests of steel, GFRP and finally the hybrid specimen flexural tests are mentioned.

The simulation strategy, the material model which is needed for the process and structural simulation are constructed. The FE model description and the boundary conditions employed for them are contemplated and how well the simulation results equates to the experimental results from the previous chapter are argued in Chapter 5.

In Chapter 6, the Toyota Camry model is used for analysing the crash performance based on various load cases. The critical parts within the model are prioritized based on certain categories and the components which are decided to patch are notified.

Ensuring that, the contrasting features of the crash performance of the final list of components is conferred. The procedure of transferring the process simulation to the component which obtained the best results out of the final list of components is reviewed.

The Chapter 7 deals with the results of both the thermal and mechanical analysis of the process simulation, process validation simulation and also the hybrid component in Toyota Camry model. The displacements as a result of the thermal analysis and also the stresses which occurs in the adhesive layer because of the CTE mismatch are conferred.

For the future scope of this present work, the temperature-dependent CZM must be built up for predicting the temperature based stresses and performance of the bonding agent which could be more interesting. Also the experimental verification of a particular part in a car model is desirable. If all these points are taken care of, then the influence of the most important parameters such as the thermal expansion coefficients of the different materials, the component dimension adaptations and the adhesive performance can be studied deeply which could avoid the future failures after the paint drying process.

## 9 Bibliography

- [1] Robert Georg Dietrich. *Analyse der Wärmeausdehnungs-Inkompatibilität bei Klebverbindungen aus CFK, Stahl und Aluminium bei der Fertigung einer lackierten Karosserie*. PhD thesis, Technische Universität München, Germany, 2017.
- [2] Ralph Lässig. Series production of high-strength composites - perspectives for the german engineering industry - a study, 2012. URL [https://lightweight.vdma.org/documents/266675/2307595/RBSC\\_VDMA\\_Composite\\_Studie\\_FINAL\\_en.pdf/737779e4-24c1-4eee-9d71-b821253cddca](https://lightweight.vdma.org/documents/266675/2307595/RBSC_VDMA_Composite_Studie_FINAL_en.pdf/737779e4-24c1-4eee-9d71-b821253cddca).
- [3] Claus-Peter Köth. *Insight Automobilindustrie 2016 Leichtbau in der Automobilindustrie*. Vogel Verlag. 2016.
- [4] Lee M.S., Hyung-Yoon Seo, and Chung-gil Kang. Comparison of collision test results for center-pillar reinforcements with twb and cr420/cfrp hybrid composite materials using experimental and theoretical methods. *Composite Structures*, Vol.168, 02 2017. doi: 10.1016/j.compstruct.2017.02.068.
- [5] Bruno Lüdke and Markus Pfestorf. Functional design of a lightweight body in white - how to determine body in white materials according to structural requirements. In *International Symposium on Niobium microalloyed Sheet Steel for Automotive Applications*, pages 27–44. The Minerals, Metals and Materials Society, 2006.
- [6] Larry.M. A guide to carbon fiber reinforced polymer repairs. 2016. URL <https://www.vehicleservicepros.com/collision-repair/body-shop-and-repair/article/21191679/a-guide-to-carbon-fiber-reinforced-polymer-repairs>.
- [7] Leif Ickert, Dieter Thomas, Thomas Tröster, and Lutz Eckstein. Beitrag zum Fortschritt im automobilleichtbau durch belastungsgerechte gestaltung und innovative lösungen für lokale verstärkungen von fahrzeugstrukturen in mischbauweise. *FAT-Schriftenreihe 244*, (244), 2012.
- [8] Edmund Haberstroh and Michael Sickert. Thermal direct joining of hybrid plastic metal components. *KMUTNB International Journal of Applied Science and Technology*, Vol.7:29–34, 09 2014. doi: 10.14416/j.ijast.2014.07.002.
- [9] C. Ageorges, L. Ye, and M. Hou. *Fusion bonding of Polymer composites*. Number Issue.6. 2001. doi: 10.1016/S1359-835X(00)00166-4.

- [10] Robert Thomas, Fabian Fischer, and Maik Gude. Adhesives for increasing the bonding strength of in situ manufactured metal-composite joints. *Proceedings of the Institution of Mechanical Engineers, Part D: Journal of Automobile Engineering*, pages 1–14, 2020. doi: 10.1177/0954407020965759. URL <https://doi.org/10.1177/0954407020965759>.
- [11] Levent Jusufi, Roland Körber, Julia Weimer, Kristian Lippky, Stefan Kreling, and Klaus Dilger. A numerical illustration of the fusion bonding process. *Proceedings of the Institution of Mechanical Engineers, Part L: Journal of Materials Design and Applications*, Vol.231, 08 2016. doi: 10.1177/1464420716665649.
- [12] Peter Mitschang, Rudi Velthuis, Stefan Emrich, and Michael Kopnarski. Induction heated joining of aluminum and carbon fiber reinforced nylon 66. *Journal of Thermoplastic Composite Materials - J THERMOPLAST COMPOS MATER*, Vol.22:767–801, 10 2009. doi: 10.1177/0892705709105969.
- [13] L. Kaempf, K. Dilger, and S. Hartwig. Bonding behavior of fusion bonded hybrid joints with press hardened steel and glass mat reinforced thermoplastic. *The Journal of Adhesion*, Vol.96(1-4):113–129, 2020. doi: 10.1080/00218464.2019.1668783. URL <https://doi.org/10.1080/00218464.2019.1668783>.
- [14] K. Lippky, Malte Mund, David Blass, and Klaus Dilger. Investigation of hybrid fusion bonds under varying manufacturing and operating procedures. *Composite Structures*, Vol.202, 01 2018. doi: 10.1016/j.compstruct.2018.01.078.
- [15] Tobias Reincke, Stefan Kreling, and Klaus Dilger. Adhesion of continuously manufactured fusion bonded multi-material structures consisting of steel and carbon fibre reinforced polyamide 6. *International Journal of Adhesion and Adhesives*, Vol.79, 09 2017. doi: 10.1016/j.ijadhadh.2017.09.012.
- [16] Dušan Kecman. Bending collapse of rectangular and square section tubes. *International Journal of Mechanical Sciences*, Vol.25(9):623–636, 1983. ISSN 0020-7403. doi: [https://doi.org/10.1016/0020-7403\(83\)90072-3](https://doi.org/10.1016/0020-7403(83)90072-3). URL <https://www.sciencedirect.com/science/article/pii/0020740383900723>. Special Issue Structural Crashworthiness Conference.
- [17] Robert Thomas, Sören Handtke, Simon Wehler, Fabian Fischer, and Maik Gude. Co-curing of thermoset composites on metal structures with reduced cycle times for high-volume car applications. *Materials Today: Proceedings*, Vol.34, 04 2020. doi: 10.1016/j.matpr.2020.03.550.
- [18] Christian Lauter, Jörg Niewel, Bernd Siewers, and Björn Zanft. Crash worthiness of hybrid pillar structures consisting of sheet metal and local cfrp reinforcements. 07 2012.

- [19] Gurbinder Dhaliwal and Golam Newaz. Experimental and numerical investigation of flexural behavior of carbon fiber reinforced aluminum laminates. *Journal of Reinforced Plastics and Composites*, 35, 02 2016. doi: 10.1177/0731684416632606.
- [20] Gurbinder S. Dhaliwal and Golam M. Newaz. Experimental and numerical investigation of flexural behavior of hat sectioned aluminum/carbon fiber reinforced mixed material composite beam. *Composites Part B: Engineering*, 182: 107642, 2020. ISSN 1359-8368. doi: <https://doi.org/10.1016/j.compositesb.2019.107642>. URL <https://www.sciencedirect.com/science/article/pii/S1359836819340156>.
- [21] Kai Jin, Hao Wang, Jie Tao, and Dandan Du. Mechanical analysis and progressive failure prediction for fibre metal laminates using a 3d constitutive model. *Composites Part A: Applied Science and Manufacturing*, 124:105490, 06 2019. doi: 10.1016/j.compositesa.2019.105490.
- [22] Zhixin Huang, Xiong Zhang, and Chongyi Yang. Experimental and numerical studies on the bending collapse of multi-cell aluminum/cfrp hybrid tubes. *Composites Part B: Engineering*, 181:107527, 2020. ISSN 1359-8368. doi: <https://doi.org/10.1016/j.compositesb.2019.107527>. URL <https://www.sciencedirect.com/science/article/pii/S1359836819325442>.
- [23] Corin Reuter. Crashworthiness and numerical simulation of hybrid aluminium-cfrp tubes under axial impact. *Thin-Walled Structures*, 117:1–9, 08 2017. doi: 10.1016/j.tws.2017.03.034.
- [24] Niklas Günther, Michael Griese, Elisabeth Stammen, and Klaus Dilger. Modeling of adhesive layers with temperature-dependent cohesive zone elements for predicting adhesive failure during the drying process of cathodic dip painting. *Proceedings of the Institution of Mechanical Engineers, Part L: Journal of Materials: Design and Applications*, 233:146442071880600, 10 2018. doi: 10.1177/1464420718806005.
- [25] Kalimuthu Suba Siva Chandran, Niklas Günther, and Erdeniz Ince. Studienarbeit: Simulation of production process-related adhesive damage of adhesively bonded multi-material body in white. 05 2020.
- [26] W. P. Goss. Thermal properties of wood and wood products.
- [27] Manuel Längauer, Franz Brunnthaller, Gernot Zitzenbacher, Christoph Burgstaller, and Christoph Hochenauer. Modeling of the anisotropic thermal conductivity of fabrics embedded in a thermoplastic matrix system. *Polymer Composites*, 42, 01 2021. doi: 10.1002/pc.25958.

- [28] Alexander Lion, Anton Matzenmiller, Gerson Meschut, Dominik Teutenberg, Patrick Kühlmeyer, and Christoph Liebl. Methodenentwicklung zur simulation und bewertung fertigungs- und betriebsbedingter klebschichtschädigungen infolge temperaturwechselbeanspruchung. *Forschungsvorhaben P878, Förderkennzeichen 369 ZN*, 2014.
- [29] David W. Green, Jerrold E. Winandy, and David E. Kretschmann. Mechanical properties of wood. wood handbook : wood as an engineering material. madison, wi : Usda forest service, forest products laboratory. *General technical report FPL ; GTR-113: Pages 4.1-4.45*, 1999.
- [30] Young's modulus: Modulus of elasticity of wood. <https://amesweb.info/Materials/Youngs-Modulus-of-Wood.aspx>, . [2021; accessed 20-July-2021].
- [31] Modulus of elasticity and Poisson's coefficient of wood. <https://www.sonelastis.com/en/fundamentals/tables-of-materials-properties/woods.html>, . [2021; accessed 20-July-2021].
- [32] Muhammad Anas Athar M.Sc. Experimental values of the GFRP laminate. 2021.
- [33] Hexcel. Mechanical properties of Redux® 677. [https://www.hexcel.com/user-area/content\\_media/raw/HexBond\\_677\\_DataSheet.pdf](https://www.hexcel.com/user-area/content_media/raw/HexBond_677_DataSheet.pdf). [2021; accessed 20-July-2021].
- [34] Ferhat Aydin. Experimental investigation of thermal expansion and concrete strength effects on frp bars behavior embedded in concrete. *Construction and Building Materials*, 163:1–8, 02 2018. doi: 10.1016/j.conbuildmat.2017.12.101.
- [35] EU Commission: CO<sub>2</sub> emission performance standards for cars and vans. 2018. URL [https://ec.europa.eu/clima/sites/clima/files/transport/vehicles/docs/ldv\\_post\\_2020\\_co2\\_en.pdf](https://ec.europa.eu/clima/sites/clima/files/transport/vehicles/docs/ldv_post_2020_co2_en.pdf).
- [36] M. Wilhelm. *Fügbarkeit von CFK-Mischverbindungen mittels umformtechnischer Prozesse*. PhD thesis, Technische Universität Dresden, Germany, 2014.
- [37] Stephan Rosenthal, Fabian Maaß, Mike Kamaliev, Marlon Hahn, Soeren Gies, and A. Tekkaya. Lightweight in automotive components by forming technology. *Automotive Innovation*, Vol.3, 07 2020. doi: 10.1007/s42154-020-00103-3.
- [38] Gordon Kelly. Joining of carbon fibre reinforced plastics for automotive applications. 01 2004. URL [https://www.researchgate.net/publication/267775412\\_Joining\\_of\\_Carbon\\_Fibre\\_Reinforced\\_Plastics\\_for\\_Automotive\\_Applications](https://www.researchgate.net/publication/267775412_Joining_of_Carbon_Fibre_Reinforced_Plastics_for_Automotive_Applications).

- [39] N. López de Lacalle, A. Lamikiz, F.J. Campa, A. FDZ. Valdivielso, and I. Etxeberria. Design and test of a multitooth tool for cfrp milling. *Journal of Composite Materials*, 43(26):3275–3290, 2009. doi: 10.1177/0021998309345354. URL <https://doi.org/10.1177/0021998309345354>.
- [40] Kristian Lippky, Stefan Kreling, and Klaus Dilger. Fügetechnik für die integrierte produktion hybrider leichtbaustrukturen. *Lightweight Design*, Vol.9:48–51, 06 2016. doi: 10.1007/s35725-016-0019-7.
- [41] Ye Lin, Junying Min, Hao Teng, Jianping Lin, Jiahao Hu, and Nanjie Xu. Flexural performance of steel–frp composites for automotive applications. *Automotive Innovation*, Vol.3, 08 2020. doi: 10.1007/s42154-020-00109-x.
- [42] Tae Lim, Byung Chul Kim, and D. Lee. Fatigue characteristics of the bolted joints for unidirectional composite laminates. *Composite Structures*, pages 58–68, 01 2006. doi: 10.1016/j.compstruct.2004.10.013.
- [43] D. W. Oplinger. *Mechanical Fastening and Adhesive Bonding*, pages 610–666. Springer US, Boston, MA, 1998. doi: 10.1007/978-1-4615-6389-1\_29. URL [https://doi.org/10.1007/978-1-4615-6389-1\\_29](https://doi.org/10.1007/978-1-4615-6389-1_29).
- [44] Andreas Roesner, Sven Scheik, Alexander Olowinsky, Arnold Gillner, Uwe Reisgen, and Markus Schleser. Laser assisted joining of plastic metal hybrids. *Physics Procedia*, 12:370–377, 12 2011. doi: 10.1016/j.phpro.2011.03.146.
- [45] J.G. Teng, Tao Yu, and Dilum Fernando. Strengthening of steel structures with fiber-reinforced polymer composites. *Journal of Constructional Steel Research*, Vol.78:131–143, 11 2012. doi: 10.1016/j.jcsr.2012.06.011.
- [46] Pedro Cortes and W. Cantwell. The prediction of tensile failure in titanium-based thermoplastic fibre-metal laminates. *Composites Science and Technology*, Vol.66:2306–2316, 10 2006. doi: 10.1016/j.compscitech.2005.11.031.
- [47] Pedro Cortes and W. Cantwell. Fracture properties of a fiber-metal laminates based on magnesium alloy. *Journal of Materials Science*, Vol.39:1081–1083, 02 2004. doi: 10.1023/B:JMSC.0000012949.94672.77.
- [48] P. Gonzalez-Chi, L. May-Hernández, and J. Carrillo. Polypropylene composites unidirectionally reinforced with polyester fibers. *Journal of Composite Materials - J COMPOS MATER*, 38:1521–1532, 09 2004. doi: 10.1177/0021998304043754.
- [49] N.G. Gonzalez-Canche, E.A. Flores-Johnson, and J.G. Carrillo. Mechanical characterization of fiber metal laminate based on aramid fiber reinforced polypropylene. *Composite Structures*, 172:259–266, 2017. ISSN 0263-8223. doi: <https://doi.org/10.1016/j.compstruct.2017.02.100>. URL <https://www.sciencedirect.com/science/article/pii/S0263822316328161>.

- [50] Composite insert as a structural reinforcement for a-pillars. *Continuous-fiber-reinforced thermoplastic composites for lightweight car design*, 10 2019. URL <https://lanxess.com/en/Media/Press-Releases/2019/09/Composite-insert-as-a-structural-reinforcement-for-A-pillars>.
- [51] Alexander Böttcher and Hermann Opdemom. Series-production adhesive process for hybrid components. *Lightweight Design worldwide*, Vol.12:48–53, 2019.
- [52] Kristian Lippky, Julia Weimer, Raphael Schnurr, Jan Beuscher, Stefan Kreling, Klaus Dröder, and Klaus Dilger. Laser pretreatment of contaminated surfaces for fusion bonding processes. 01 2016.
- [53] Robert Thomas, Simon Wehler, and Fabian Fischer. Predicting the process-dependent material properties to evaluate the warpage of a co-cured epoxy-based composite on metal structures. *Composites Part A: Applied Science and Manufacturing*, Vol.133:105857, 02 2020. doi: 10.1016/j.compositesa.2020.105857.
- [54] Xingshuang Peng, Shuai Liu, Yaodong Huang, and Lin Sang. Investigation of joining of continuous glass fibre reinforced polypropylene laminates via fusion bonding and hotmelt adhesive film. *International Journal of Adhesion and Adhesives*, Vol.100:102615, 2020. ISSN 0143-7496. doi: <https://doi.org/10.1016/j.ijadhadh.2020.102615>. URL <https://www.sciencedirect.com/science/article/pii/S0143749620300774>.
- [55] Tobias Reincke, Sven Hartwig, and Klaus Dilger. Improvement of the adhesion of continuously manufactured multi-material joints by application of thermoplastic adhesive film. *International Journal of Adhesion and Adhesives*, Vol.93, 09 2019. doi: 10.1016/j.ijadhadh.2019.01.015.
- [56] Tobias Reincke, Sven Hartwig, and Klaus Dilger. High-tensile joints of continuously fusion bonded hybrid structures. *Composite Structures*, Vol.202, 12 2017. doi: 10.1016/j.compstruct.2017.12.027.
- [57] Tobias Reincke, Sven Hartwig, and Klaus Dilger. Enhanced comprehension of the continuous fusion bonding process of multi-material structures. *Materials Science Forum*, Vol.939:197–204, 11 2018. doi: 10.4028/www.scientific.net/MSF.939.197.
- [58] Tobias Reincke, Stefan Kreling, and Klaus Dilger. *The Production-Related Influence of Iron Oxides on Steel Surfaces on the Adhesion of Fusion-Bonded Hybrid Structures*, pages 363–376. 03 2017. ISBN 978-3-319-50783-5. doi: 10.1007/978-3-319-50784-2\_27.

- [59] Sung-Jin Kim, Jun Park, Jss Babu, Hyeong Seo, and Chung-Gil Kang. Effect of interface bonding process on bending strength in cfrp/metal hybrid composites. *IOP Conference Series: Materials Science and Engineering*, Vol.715:012102, 01 2020. doi: 10.1088/1757-899X/715/1/012102.
- [60] Osamah Barak, Mursal.L. Saad, Marwan Mezher, Sabah Hussein, and Mahmood Hamzah. Joining of double pre-holed aluminum alloy aa6061-t6 to polyamide pa using hot press technique. *IOP Conference Series: Materials Science and Engineering*, Vol.881:012062, 08 2020. doi: 10.1088/1757-899X/881/1/012062.
- [61] Jean Bergmann and Martin Stambke. Potential of laser-manufactured polymer-metal hybrid joints. *Physics Procedia*, Vol.39:84–91, 12 2012. doi: 10.1016/j.phpro.2012.10.017.
- [62] Ives De Baere, Wim Van Paepegem, and Joris Degrieck. Feasibility study of fusion bonding for carbon fabric reinforced polyphenylene sulphide by hot-tool welding. *Journal of Thermoplastic Composite Materials*, Vol.25:135–151, 03 2012. doi: 10.1177/0892705711408160.
- [63] F. Behnisch, P. Rosenberg, K. A. Weidenmann, and F. Henning. Investigation of the matrix influence on the laminate properties of epoxy- and polyurethane-based cfrcps manufactured with hp-rtm-process. *AIP Conference Proceedings*, 1914(1):180003, 2017. doi: 10.1063/1.5016789. URL <https://aip.scitation.org/doi/abs/10.1063/1.5016789>.
- [64] Mirko Schaper, Gerson Meschut, Rolf Mahnken, Mathias Bobbert, Christian Lauter, Carolin Zinn, Zheng Wang, and Christian Dammann. Influences of interface and surface pretreatment on the mechanical properties of metal-cfrp hybrid structures manufactured by resin transfer moulding. *International Journal of Automotive Composites*, Vol.2:272, 01 2016. doi: 10.1504/IJAUTOC.2016.10005305.
- [65] Lee M.S., Hyung-Yoon Seo, and Chung Kang. Comparative study on mechanical properties of cr340/cfrp composites through three point bending test by using theoretical and experimental methods. *International Journal of Precision Engineering and Manufacturing-Green Technology*, Vol.3:359–365, 10 2016. doi: 10.1007/s40684-016-0045-z.
- [66] Hwa-Young Kim, Min sik Lee, and C. Kang. The fabrication of a hybrid material using the technique of hot-press molding. *Materials and Manufacturing Processes*, 28:892 – 898, 2013.
- [67] Abaqus 6.14 manual. <http://abaqus.software.polimi.it/v6.14/index.html>. [2021; accessed 20-July-2021].

- [68] Ruohang Xu, Yixin Huang, Yuan Lin, Binsheng Bai, and Teng Huang. In-plane flexural behaviour and failure prediction of carbon fibre-reinforced aluminium laminates. *Journal of Reinforced Plastics and Composites*, 36: 073168441770887, 05 2017. doi: 10.1177/0731684417708871.
- [69] Peter Mitschang and Rudi Velthuis. Process parameters for induction welding of metal/ composite joints. Proceedings ECCM-13, 2008.
- [70] N. Günther, M. Griese, E. Stammen, and K. Dilger. Loading capacity of adhesive joints regarding their manufacturing process. *Journal of Advanced Joining Processes*, Vol.1:100020, 2020. ISSN 2666-3309. doi: <https://doi.org/10.1016/j.jajp.2020.100020>. URL <https://www.sciencedirect.com/science/article/pii/S2666330920300182>.
- [71] Eichleiter.F. *Fertigungs- und prozessbedingte Eigenschaften von Klebverbindungen im Karosseriebau*. PhD thesis, Shaker Verlag, Germany, 2011.
- [72] G. Jeyakodi. Finite element simulation of the in - situ afp process for thermoplastic composites using abaqus. 2016.
- [73] Heat transfer coefficient. URL [https://en.wikipedia.org/wiki/Heat\\_transfer\\_coefficient](https://en.wikipedia.org/wiki/Heat_transfer_coefficient). [2021; accessed 20-July-2021].
- [74] Sequentially coupled thermal-stress analysis. URL <https://abaqus-docs.mit.edu/2017/English/SIMACAEANLRefMap/simaanl-c-thermstresanal.htm>. [2021; accessed 20-July-2021].
- [75] Heat-press equipment. URL <https://www.servitecberlin.de/de/laborpressen-servitec-berlin/polystat-200t.html>. [2021; accessed 20-July-2021].
- [76] Performance of continuum and shell elements for linear analysis of bending problems. <https://abaqus-docs.mit.edu/2017/English/SIMACAEBMKRefMap/simabmk-c-linbending.htm>. [2021; accessed 20-July-2021].
- [77] ANSA pre-processor introduction. URL <https://www.beta-cae.com/ansa.htm>.